UNIVERSITÀ DEGLI STUDI DI PADOVA

Dipartimento di Fisica e Astronomia "Galileo Galilei"

Corso di Laurea Magistrale in Fisica

Tesi di Laurea

Depth distribution of particles in plastics in sea-water

Relatore	**Laureando**
Prof. Marcello Lunardon	**Nicolò Tuccori**
Correlatrici	
Prof. Maria Teresa Peña	
Prof. Maria Teresa Pinheiro	

Anno Accademico 2017/2018

To my parents

Acknowledgments

This thesis was financed by the Portuguese Fundaçao para a Ciência e Tecnologia (FCT) through the projects PLASTICGLOBAL (PTDC/MAR-PRO/1851/2014), UID/BIO/04565/2013, UID/Multi/04349/2013, Programa Operacional Regional de Lisboa (LISBOA-01-0145-FEDER-007317) and Erasmus+ mobility programme.

Author is extremely grateful to Prof. T. Pinheiro, Prof. M. T. Peña and Prof. L. C. Alves for all the help provided not only during the experimental activity at CTN and also to Prof. V. Corregidor for her assistance with NDF.

Special thanks also to Prof. Lunardon, for his support during the thesis activity and for the useful advices.

Sommario

Al giorno d'oggi detriti plastici di diverse forme e dimensioni sono contaminanti presenti a livello globale negli ecosistemi acquatici. I meccanismi di interazione di questi polimeri con i principali costituenti degli ambienti marini sono però per lo più sconosciuti. L'analisi simultanea con le tecniche PIXE e RBS di campioni di diverse plastiche, permessa dall'uso di una microsonda nucleare, offre possibilità uniche di caratterizzare il materiale accumulato nella superficie dei polimeri e le modalità con cui questi interagiscono con gli elementi chimici dell'ambiente circostante. In particolare, in questa tesi, sono stati analizzati campioni di polietilene ad alta densità (HDPE), polietilene tereftalato (PET) e polipropilene (PP) immersi nell'estuario del fiume Tagus (Lisbona, Portogallo) per 7 e 30 giorni. La caratterizzazione del deposito su scala micrometrica ha rivelato l'esistenza di materiale sedimentario, salino e biologico. Uno dei principali risultati osservati è stata la diffusione degli ioni Cl^- nella matrice dei polimeri studiati, riscontrata esaminando le distribuzioni degli elementi in sezioni trasversali dei campioni. La complementarietà delle tecniche PIXE e RBS e la capacità di analisi di software come OMDAQ2007 e NDF hanno permesso inoltre di valutare la struttura in profondità di depositi sia biotici che abiotici. I risultati hanno indicato una struttura multistrato, segno della complessa distribuzione del materiale cellulare e sedimentario presente sulla superficie delle plastiche. Questo studio ha mostrato che l'uso della microsonda nucleare, combinata con adeguati strumenti analitici (OMDAQ2007 e NDF), presenta caratteristiche esclusive e favorevoli per lo studio del deterioramento delle plastiche e il loro ruolo nel trasporto di elementi chimici. Infine, osservando la diffusione degli ioni Cl^-, sono state fornite nuove evidenze scientifiche sul processo di degradazione dei polimeri esposti in ambienti marini.

Parole chiave: Degradazione plastica, microsonda nucleare, PIXE, RBS, concentrazione elementi

Abstract

Undoubtedly plastics of various shapes and sizes become a persistent contaminant in aquatic ecosystems, from rivers to the ocean. The interaction mechanisms of the polymers with the main constituents of these environments are not completely unravelled yet. Nuclear microprobe clusters PIXE and RBS techniques, which offer unique possibilities to characterize the materials deposited on the surface of plastics rejected to the aquatic environment. In this study, high-density polyethylene (HDPE), polyethylene terephthalate (PET) and polypropylene (PP) are exposed to turbid water of the Tagus estuary (Lisbon, Portugal) for 7 and 30 days. The characterization of the deposition mosaic at the microscale level reveals to contain sediment, biotic and saline components. A major finding is the diffusion of the ion Cl^- in the polymers matrix, observed examining the profiles of elements present in the deposits along the transversal sections of the polymers. Additionally, the combination of PIXE and RBS and the capabilities of general purpose programs, such as OMDAQ2007 and NDF, allowed the investigation of the depth structure of biotic and abiotic deposits. Results point out for a multilayer depth structure which can decode the complex arrangement of cellular and sedimentary materials deposited on the polymers surface. This study demonstrates that nuclear microprobe, in combination with OMDAQ2007 and NDF analytical tools, offers unique possibilities to study plastic degradation and plastic chemical transfer with minimal sample manipulation. Finally, this study contributes to provide scientific evidences of plastic weathering in seawater, which are virtually lacking.

Keywords: Plastic weathering, nuclear microprobe, PIXE, RBS, elemental concentration, depth structure

Contents

List of Tables

List of Figures

Nomenclature

$(\frac{\mu}{\rho})_p$	Concentration-weighted sum of the mass attenuation coefficients of the matrix elements for the emission line p.
χ	Screening function.
δE	RBS energy resolution.
$\Delta E'$	Energy difference in RBS spectrum due to scattering with different elements.
ΔE_x	Energy difference in RBS spectrum due to scattering in the surface and at depth x_t.
ΔM	Mass difference of two elements.
δM	Mass resolution.
Δt	Sample thickness.
ϵ	Stopping cross-section factor.
ϵ_0	Vacuum permittivity.
ϵ_P	PIXE detector efficiency.
ϵ_R	RBS detector efficiency.
η	Sensitivity factor.
ω	Fluorescence yield.
Ω_P	PIXE detector solid angle.
Ω_R	RBS detector solid angle.
Φ	Target recoil angle.
σ_R	Rutherford Cross-section.
σ_S	Screened cross-section.
σ_z	Ionization cross section of element Z.
θ	Scattering angle.
θ_1	Entrance angle between projectile and sample normal.

θ_2	Backscattered particles exit angle respect surface normal.
θ_s	Backscattering angle.
θ_{TO}	X-rays take-off angle.
A	Atomic mass.
a_0	Bohr radius.
A_mB_n	General compound chemical formula.
b	Branching ratio.
d	Distance of closest approach.
DTR_P	PIXE dead time ratio.
DTR_R	RBS dead time ratio.
E	Energy.
e	Elementary charge.
E_2	Initial target nucleus energy.
E_2'	Target nucleus energy after the scattering process.
E_f	Final energy of ionizing particles.
E_1	Initial beam ions velocity.
E_{bs}	Particles energy just before being scattered at depth x_t.
E_{NR}^{high}	Energy above which high-energy effects due to non-Rutherford scattering are important.
E_{NR}^{low}	Energy below which low-energy effects due to non-Rutherford scattering are important.
E_s	Particles energy just after being scattered at depth x_t.
E_{TF}	Thomas-Fermi energy.
F	Screening correction factor.
f	X-ray frequency.
h	Planck constant.
I	Mean excitation potential.
K	Kinematic factor.
K, L, M, O	Atomic shells.
M	Matrix parameters.

m_e	Electron mass.
M_i	Mass of the i element.
n_e	Number of electron per unit volume.
n_f, n_i	Principal quantum numbers involved in X-ray emission.
N_p	Number of incident particles.
N_Z	Concentration of the element Z.
N_{RBS}	Total RBS yield.
R	Rydberg constant.
r	Distance between two nuclei.
R_0	Constant for nucleus radius estimation.
R_n	Nucleus radius.
R_p	Range of the particle p.
S_M	Stopping power in matrix M.
t	Transmission coefficient.
T_Z	X-ray transmission from the successive depths in the matrix.
v	Incident velocity.
v'	Scattered velocity.
v_0	Bohr velocity.
v_{TF}	Thomas-Fermi velocity.
x_t	Depth of the sample nucleus involved in the scattering process.
Y_P	PIXE yield.
Y_R	RBS yield.
Z	Atomic number.
$[\epsilon]$	Stopping power cross-section.
$[E_f]$	Energy loss factor.

Subscripts

$\alpha, \beta, \gamma, \delta$	Siegbahn notation for emission lines.
in, out	In- and out-coming path.
n, e	Nuclear and electronic.

Glossary

BEA	Binary-encounter approximation
CTN	Campus Tecnologico Nuclear
ECPSSR	Energy-Loss Coulomb-Repulsion Perturbed-Stationary-State Relativistic Theory
ERDA	Elastic Recoil Detection Analysis
FTIR	Fourier transform infrared spectroscopy
HDPE	High-density polyethylene
IBA	Ion Beam Analysis
MT	Metric Ton
NDF	Nuclear DataFurnace
NRA	Nuclear Reaction Analysis
PET	Polyethylene terephthalate
PIGE	Particle Induced Gamma-rays Emission
PIXE	Particle Induced X-rays Emission
PP	Polypropylene
PWBA	Plane wave Born approximation
RBS	Rutherford Backscattering Spectroscopy
SCA	Semi-classical Approximation
SEM	Scanning electron microscopy
STIM	Scanning Transmission Ion Microscopy
XPS	X-ray photoelectron spectroscopy
XRD	X-ray Diffraction

Chapter 1

Introduction

Plastic pollution issue

Plastic is a word that originally meant “pliable and easily shaped.” It only recently became a name for a category of polymers, begun to be synthesized over the last century and a half using the carbon atoms provided by petroleum and other fossil fuels. The peculiarity of these synthetic polymers is that they are made up of long chains of atoms, arranged in repeating units. It is the length of these chains, and the patterns in which they are arrayed, that make polymers strong, lightweight, and flexible. In other words, it is what makes them so “plastic”. The versatility of these materials, combined to their low cost, has lead to a great increase in their use over the past five decades, during which plastic production increased from 1.5 million metric tons (MT) in 1960 to 335 million MT in 2016 (PlasticEurope [1]). Plastics immediately became widespread and used in a bewildering variety of applications that nowadays spans mainly from packaging of products such as food, pharmaceuticals and chemicals to a growing range of buildings and constructions applications, as well as from the mobility and transport sector to electrical and electronic devices.

However, plastics cheapness and robustness are mixed blessings. Primarily, the durability of plastic, that makes it such an attractive material to use, also makes it highly resistant to degradation. As a result, disposing of end-of-life plastics with adequate waste-management organization and technologies is problematic: only since 2017, more plastic waste is recycled than landfilled (PlasticEurope [1]). These difficulties are accompanied by an intense consumption of synthetic materials, exacerbated by the copious use of disposable plastics (e.g. packaging material), that is leading to a visible accumulation of plastic debris both in landfills, where it may take centuries for such material to breakdown and decompose (Cole et al. [2]), and through indiscriminate disposal. Among the non-recycled plastics, of particular concern are debris entering the marine environment, estimated to be ~ 3 % of the total waste generated every year (Jambeck et al. [3]). Land-based plastics constitute the major source of debris, entering the ocean through a variety of pathways: coastal recreation, wastewater outflows, wind and rivers, accidental spills, leaching from landfills, discarded or lost fishing gear and storm surges during extreme weather events. At the same time, ocean-based wastes are also significant. It is estimated that around 10-20 % of these plastic debris comes from fishing industry and also virgin resin pellets, a common component of debris, enter the oceans routinely via incidental losses during ocean transport or through run-off from processing facilities (Andrady [4], Cressey

[5]). Therefore, in aquatic environments, plastic pollution is, year after year, an increasing and preoccupying environmental and toxicological issue.

Plastic fragments are generally classified by size in macroplastics and microplastics, with breakpoint commonly set to 5 mm diameter (Conkle et al. [6]). Large plastics objects, known as *macroplastics*, are directly injected in aquatic environments and constitute the majority of the plastic weight in the oceans (Fig. 1.1 a) (GESAMP [7]). The social, economic and ecological impacts of macroplastic have long been subject of research. The presence of large fragments in the marine environment presents an aesthetic issue, with economic repercussions for the tourist industry, a hazard for numerous marine-industries (e.g. shipping, fishing, energy production, aquaculture) as plastic may result in entanglement and damage of equipment, and significant environmental concerns. The environmental impact of macroplastics includes entanglement of wildlife and ingestion by local fauna, sources of injuries and death (Laist [9]). Furthermore, macroplastics can transport non-native marine species to new habitats on floating debris and smother the seabed, preventing gas-exchange and creating artificial hard-grounds (Cole et al. [2]).

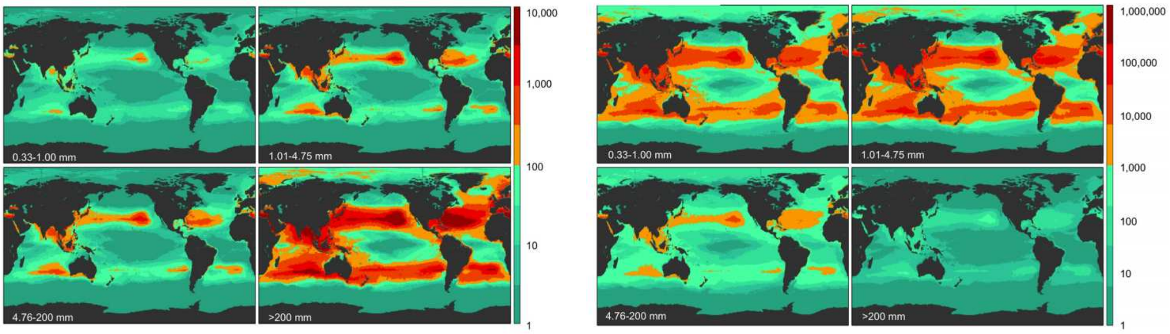

(a) Model results for global weight density in four size classes.

(b) Model results for global count density in four size classes.

Figure 1.1: Model prediction (Eriksen et al. [8]) of global weight [g/km^2] (a) and counts [$pieces/km^2$] (b) density for each of four size classes (0.33 - 1.00 mm, 1.01 - 4.75 mm, 4.76 - 200 mm, and 200 mm). The majority of global weight is from the largest size class while microplastic counts for the greater pieces density.

Nonetheless, the plastic pollution issue is increasingly focusing to *microplastics*. This is not only due to the fact that they are characterized by an higher count density in the oceans, that makes them more present worldwide than the larger debris (Fig. 1.1 b), but also because their quantity would likely increase constantly for many year to come and their impact in the surrounding is not completely unravelled yet. Plastics that are manufactured to be of microscopic size are directly introduced in aquatic ecosystem through the same pathways as larger plastics objects, land and ocean-based. Microplastics, besides including virgin plastic production pellets in their definition, are typically used in facial-cleansers and cosmetics, or as air-blasting media, whilst their use in medicine as vectors for drugs is increasingly reported (Cole et al. [2]). However, direct immission is not the only cause of the estimated growth of microplastics in aquatic environment. Over time, in fact, plastic of every size undergoes weathering processes (Fig. 1.2). The main phenomenon that cause its degradation is the exposure to solar UV radiation, which facilitates oxidative processes in polymers (Andrady [4]), and it is currently consensual that also interactions between polymers and water constituents (biota and inorganic suspended particles) can favor structural

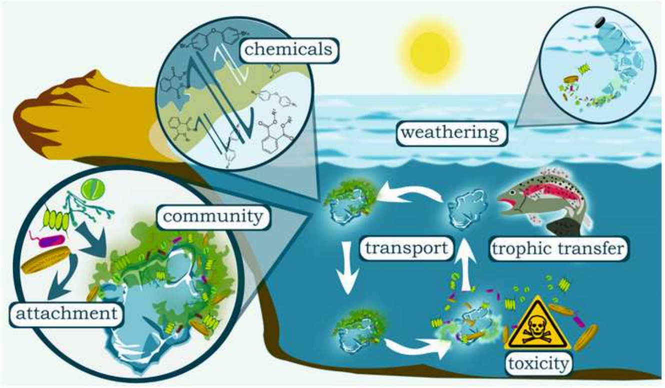

Figure 1.2: Plastics debris introduced in marine ecosystems interact with the consituents, both biotic and abiotic, of these environments. This has consequence in the plastic degradation rate, in the toxicity of polymers when injested by organisms and in habitats dynamics (Rummel et al. [10]).

changes, degradation and fragmentation (Holmes et al. [11], Gewert et al. [12], Restrepo-Florez et al. [13]). Among the others, adsorption of earth crust materials have been observed in polymers exposed to aquatic environments (Vedolin et al. [14], Kedzierski et al. [15]) causing structural changes that can modify the compactness and resistance of the material. Clastic materials is also known to increase oxidized moieties in plastics (Brennecke et al. [16]) that in turn facilitate the adhesion of biota and, through time, lead to a relatively steady film covering the plastic material, which may favor the weathering of the debris surfaces, considering that certain microorganisms can cause the biodegradation of the plastic (Shah et al. [17], Gu [18]). During advanced stages of degradation, plastic debris become weak and brittle, letting any mechanical sources (e.g. wind, waves, animal bite and human activities) to break them into fragments. Therefore, even supposing that the discharge of plastics litter in the sea is stopped, the on-going degradation of larger debris already present would likely increase the quantity of small sized fragments in the future.
To predict and model the plastic distribution in the environment during time and to investigate its environmental impact, a better comprehension of weathering process rate and modalities of plastics in water is required. The processes that probably occur to plastic debris immersed in water listed above are only few of the many and, moreover, are not fully understood: information about general modalities on how water constituents interact with polymers and the consequent effects on the ageing process are virtually lacking.

Investigating the plastic weathering when exposed to aquatic environments would be also helpful to estimate the ecological and toxicological impact of debris in those habitats. Owing to their small size, microplastics have the potential to be ingested by an array of marine biota and thus to be introduced in the food-chain. Trace of polymers has been found in a large variety of marine taxa, representing various trophic levels, that include fish-eating birds, marine mammals, fish and invertebrates. This poses a risk to the health of organisms: experimental studies have demonstrated that at critical concentrations, microplastics can adversely affect feeding, energetic reserves, reproduction, growth, and survival in invertebrate and vertebrate species (Li et al. [19], Setälä et al. [20]). Higher levels of biological organization could also be affected, with population shifts and altered behavior impacting upon the ecological function of keystone species. The physical hazard is the first, evident, consequence associated to debris ingestion. However, recently, also the possible chemical hazard has begun to be considered. Despite the chemicals added or produced during manufacturing, marine plastic debris are susceptible to contamination by a number of waterborne-pollutants, including aqueous metals, endocrine disrupting chemicals and persistent organic pollutants (Fig. 1.2). This raises plastics also to a toxicological issue as contaminated debris, being transported around the ocean, can cause the pollution of pristine ecosystems or can be ingested by marine organisms, transferring toxins from the environment to biota (Thompson et al. [21]).

Finally, aside from physical and chemical effects, microplastics may affect marine ecosystem dynamics as well. Plastic objects floating in the surface or in the water column or in the bottom, might be colonized by marine organisms, becoming foundation for new habitats and modifying the population structure (Fig. 1.2) (Wright et al. [22]).

With additional concerns regarding risks of plastics exposure to ecosystems, food safety and public health, a better comprehension about plastics weathering in aquatic environments, including fragmentation, transportation, accumulation and interaction with marine constituents is required. Polymers degradation mechanisms have been studied typically using either *scanning electron microscopy* (SEM), that provides direct observations of the samples and *Fourier transform infrared spectroscopy* (FTIR), which enables to analyze the surface oxidation and composition. Chemical changes of the surface have also been studied with *X-ray photoelectron spectroscopy* (XPS) while *X-ray diffraction* (XRD) can furnish information about atomic and molecular structure (Shah et al. [17], Cooper and Corcoran [23], Zbyszewski et al. [24], Ikada [25], Copinet et al. [26], U Zhao et al. [27], Kosanetzky et al. [28]).

Ion Beam Analysis

Ion Beam Analysis (IBA) present interesting characteristics that could be adequate to investigate efficiently several implications induced in plastics by the exposure to marine environments. As stated by the name, IBA corresponds to a collection of techniques based on the use of a beam of accelerated ions and the selective detection of specific products of the interaction of the probing ions with an unknown target. Detected particles and/or electromagnetic radiations enable to extrapolate information about the composition and structure of surfaces and near-surface layers on the depth scale from *nm* up to *μm*. Many different techniques, based on this general analysis idea, are implemented, each of them characterized by the detection of a certain reaction product (Fig. 1.3). Elastically backscattered light ions are detected in *Rutherford Backscattering Spectroscopy* (RBS) whereas *Elastic Recoil Detection Analysis* (ERDA) focus in elastically recoiled (secondary) target atoms. X-rays and γ-radiation emitted from the target, due to relaxation of excited electron clouds or of excited atomic nuclei, are detected in the analytical methods of *Particle Induced X-rays Emission* (PIXE) or *Particle Induced Gamma-rays Emission* (PIGE), respectively. *Nuclear Reaction Analysis* (NRA), finally, is a pure nuclear technique as it is governed by nuclear reactions and kinematics. The primary ion is absorbed by the nucleus of target atoms at some resonance energies, and subsequently different secondary particles (proton, deuterium, neutron, or α-particle) or γ-rays are promptly emitted and can be detected.

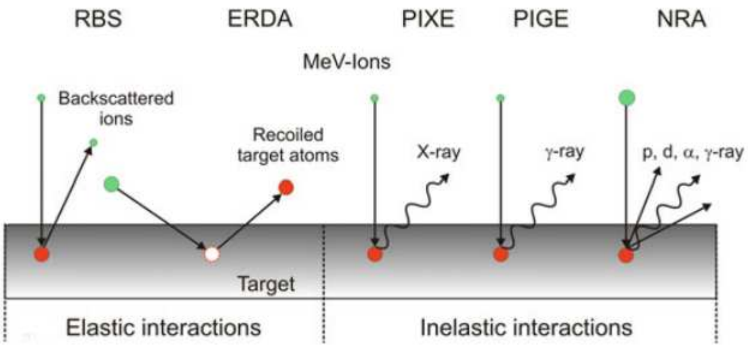

Figure 1.3: Schematic representation of ion–target interaction. MeV ion induced elastic and inelastic interaction processes are related to common ion beam analysis (IBA), whereas primary heavy ions of some keV are used to sputter secondary target ions or atoms (Schmidt and Wetzig [29])

As it can be noticed, each of the IBA methods is tailored around a particular reaction channel that is, in general, specific for the detection of certain atomic species. This represents the great potential of IBA. There is a cluster of techniques, capable of covering the whole periodic table of elements, that provides samples structure information, combining compositional information and concentration values with a *nm*-resolution depth profile. Furthermore, analysis with IBA do not require a long acquisition time and, moreover, do not damage specimens because scattering process between ions and target atoms is dominated by electronic collisions.

The utilization of a *nuclear microprobe* can improve significantly the results achieved with IBA techniques. A beam of μm size is obtained using a probe-forming lens system, allowing to increase the spatial resolution of the techniques, and a scanning magnet moves the beam in the target plan, providing 2D-mapping of the sample with micrometric resolution. Microprobes are also particularly used with IBA techniques since several detectors can be installed in the sample chamber, each collecting specific collision products related to different techniques. The information extracted joining these data are complementary and self-consistent and a more accurate description of the sample can be thus deduced (Jeynes et al. [30]).

Among the several possible fields in which IBA could be exploited, ion beam analysis with a microprobe system fulfill perfectly material analysis requirements. Different materials research fields established IBA techniques as a powerful tool to investigate elemental, structural, electronic and optical properties of the sample (Malmqvist [31]). Each of these applications takes advantages of one or more specific features that those techniques can offer. The study of technological developments of modern materials has traditionally been dominating in IBA, ranging from surface characterisation of semiconductors to nanotechnology and complex materials structure analysis (Hotovy et al. [32], Wittmer [33]). Depth composition profile provided by IBA techniques, is an useful information when studying the microscopic structure of geoscience samples, such as minerals (Ryan [34], Angelici et al. [35]). The non-destructive character of IBA techniques, instead, helped the diffusion of these analysis, especially in external beam setup (Mandò [36]), in the studies of the most sensitive kinds of arts and archaeology objects (Dran et al. [37], Corregidor et al. [38]). Over the years, given the precision and sensitivity with which elements can be locally traced, there has been extensive use of IBA methods also in medicine and biology (Maenhaut [39]), as well as in environmental studies (Malmqvist [40], Orlic [41]). Microprobe analysis in environmental issues are predominantly applied to aerosol samples intended to investigate, for example, climate changes and air pollution. Analyzed samples on the environmental research field can include also soil, sediments, plant materials, animal tissue and food. However, despite IBA unique features that permit to achieve great results also in this topic, plastic pollution in aquatic environment has never been currently dealt with those techniques. Microbeam capabilities could help to overcome partially the lack of information about the weathering of daily-use plastics which are rejected to the marine environment, analyzing the structure of the complex deposits in debris surfaces and changes in the polymers composition.

Thesis outline

In this work, two particular IBA techniques are used simultaneously to deal with the plastic environmental issue: PIXE and RBS. Analysis are provided by the *Campus Tecnologico Nuclear* (CTN) microprobe setup (Alves et al. [42]), supplied with a 2 MeV protons beam by a Van der Graaff accelerator. The analyzed samples are 5 x 10 cm^2 pieces of *polypropylene* (PP), *high-density polyethylene* (HDPE) and *polyethylene terephthalate* (PET), placed in turbid water of the *Tagus* estuary, a polluted freshwater system.

The main objective of the thesis is to demonstrate the possibility of extrapolating significant information about plastics in aquatic ecosystems using the nuclear microprobe and the simultaneous analysis provided by PIXE and RBS. These techniques permit, in principle, to analyze the chemical elements deposited on the water-exposed plastics samples, as well as the interaction modalities with the major ions present in sea-water. This characterization is achieved analyzing the samples both superficially and in their transversal section. Surface data allow to obtain high-resolution images of elemental distributions and, using dedicated softwares, estimations of the elemental concentrations on the plastic surface and of the deposit depth profile. Cross sections analysis, instead, aim to measure directly the transversal distributions of elements, investigating how permeable plastics are to metals and ions in aquatic ecosystems as well.

The organization of the thesis is intended to present initially the theoretical basis of the experimental analysis. Chapter 2, in particular, deals with PIXE and RBS theories. The specific physical processes that generate the signals of the two techniques are described, together with a discussion on their experimental applications. The experimental setup that have been used for the analysis of the plastics samples at CTN laboratory is presented in Chapter 3, focusing on the components of the beam line and of the microprobe system and their functionalities. The operations needed to obtain proper samples for this study are then described, together with the procedure that enables the microprobe analysis of the exposed polymers. Offline analysis operations of the dedicated softwares are finally listed, highlighting their virtues and limitations. The experimental results are presented in Chapter 4. PIXE and RBS data are clustered in order to obtain detailed description of the interaction of the plastic samples with aquatic materials and major ions. A characterization of the deposit distribution and morphology on the polymer surface is achieved, along with the estimation of its elemental concentration. Compositional analysis are simultaneously exploited, evaluating the depth profile of the surface material and investigating the evidence of element absorption inside the plastic matrix.

Chapter 2

Nuclear microprobe analytical methods

The nuclear microprobe setup is adaptable, as already anticipated in the introductory chapter, to several IBA techniques. In order to detect a specific scattering product, adequate detector and electronics have to be installed in the sample chamber. The CTN microprobe, in particular, employs the instrumentation required for PIXE, RBS and STIM (*Scanning Transmission Ion Microscopy*), an alternative IBA technique that utilize the ions energy loss that transverse completely the specimen as imaging mechanism. In this experimental work, the analysis of the plastic samples are provided by the simultaneous collection of PIXE and RBS events. Considered singularly, each of these techniques permits the characterization of materials, with different features and results. A theoretical approach to PIXE is presented in Section 2.1, describing the physical process that regulate the X-ray emission together with a discussion of the yield of this technique that allows the elemental concentration estimations. It is also introduced the reason why PIXE is widely used for multi-elemental analysis in several areas. In Section 2.2, RBS is addressed from a similar perspective, ranging from the model of the backscattering process and the correspondent cross-section to the properties that establish RBS as a powerful technique to assess materials depth structure and composition. In conclusion, in Section 2.3, two analytical methods that cluster PIXE and RBS data are presented.

2.1 Proton Induced X-Ray Emission (PIXE)

PIXE is based on the excitation of inner-shell electrons from target atoms by the energetic incident particles impact, and the spectroscopy of the subsequently emitted X-rays during the electronic relaxation. Usually, in PIXE technique applications, the accelerated particles that compose the beam are protons, due to their low bremsstrahlung radiations, high X-ray production cross-section and good knowledge of fundamental parameters. Electrons, despite requiring lower energy to have the same ionization cross-section of protons, are not suitable with PIXE trace element analysis since they produce a non negligible quantity of bremsstrahlung radiation that contributes to a much higher spectrum background, implying higher detection limits. ^{1}H ions are also preferred to heavier because of the larger ionization cross-section, considering beam of the same energy. If a beam of heavy ions is used for PIXE analysis, the particles should be accelerated at higher energies and thus different accelerating technologies are needed. As a result, PIXE is frequently used to refer specifically to Proton Induced X-ray Emission.

Its considerable success among material analysis techniques arose since the '70 (Johansson et al. [43]), when both experimental and theoretical developments allowed to exploit efficiently this technique. The reason of the increasing interest in PIXE is due to the unique characteristics of its analysis: fast, sensitive and multi-elemental. The analysis of samples made collecting the atomic X-ray emission are remarkably fast because of the large cross-section that describes this process. The peculiar sensitivity is due to the in-depth knowledge of the cross-section values that is needed to estimate the elemental concentrations, whereas the capability to provide multi-elemental description of the samples is a consequence of the unique shells structure of every atom and of the characteristics of the solid state detectors used in this type of analysis. Moreover, its non-destructive character, makes PIXE suitable to different kind of specimens, that need appropriate attentions to be analyzed. Finally, another interesting feature, is that the composition information that PIXE provides do not take into account the chemical bonds and compounds in the samples but are related only to the single elements and can be thus used to an elemental characterization of materials.

Through this Section, a theoretical approach is followed to explain what stated above. The description of the atomic X-ray emission process and the ionization cross-section are combined to formulate a proper definition of the experimental yield.

2.1.1 Atomic X-Ray Emission

X-rays, observed for the first time in 1895 by Wilhelm Conrad Röntgen, denote the part of the electromagnetic spectrum with wavelengths in the range from 10 to 0.01 *nm*. This includes the atomic radiation emitted in the electronic de-excitation process: a vacancy created in the atomic inner-shells is filled by an out-shell electron, and the excess energy taken away by X-ray photon. These radiations are the fingerprints of every atoms, since their energy is determined by the difference in binding energies of the two subshells involved, and the atomic energy levels structure is unique for each element. The various X-ray lines that characterize every atoms are schematized in Fig. 2.1, labelled according to the *Siegbahn* notation. For a vacancy created in the K shell, a K_α X-ray is emitted if an L shell electron fills the vacancy, and a more energetic K_β, K_γ or K_δ X-ray is emitted if respectively an M, N or O shell electron fills the vacancy. Similarly, L_α, L_β and L_γ X-rays are caused by an L shell vacancy being filled by an electronic transition from an higher shell, and so the various M lines. Due to the energy degeneration of each shell in several energy sub-levels that can participate in the correspondent shell emission line, the adopted notation includes also a number to specify which is the energy level considered. The K_α emission line thus includes the K_{α_1} and K_{α_2} and similarly for every emission lines. In Fig. 2.1 only the allowed atomic transitions related to the K, L and M shells are reported. In fact, X-ray emission is mainly due to dipole radiation in which electron transition selection rules, given by the unitary angular momentum of the photon, are obeyed. These selection rules determine also the probability related to an inner-shell to be filled by a specific outer, similarly to the characteristic energy of the transition. A larger energy difference between two atomic energy levels is translated, not considering in principle any selection rule, to a lower probability that an electron de-excites from the higher energy shell. Consequently, the α X-ray lines have,

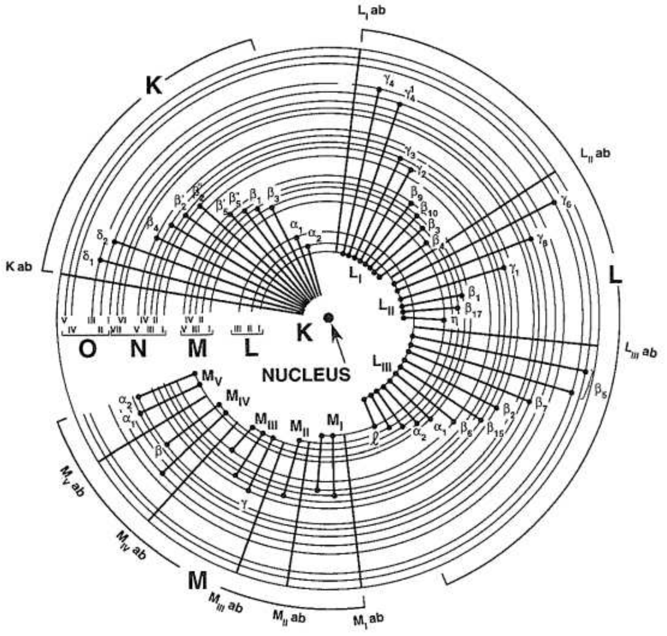

Figure 2.1: Allowed K, L and M transition lines, labelled according to the Siegbahn notation (Woldseth [44]).

usually, the higher probability to be emitted. This probability is called *branching ratio b* and represents, among every line of a specific shell, the fraction of the correspondent X-rays emitted. Characteristic energies of light elements are reported on Table 2.1. If the K_{α_1} and K_{α_2} lines energies are close, that is especially the case of low Z elements, and the energy resolution of the detection system does not allow to separate their energy difference, they are considered as a single line, the K_α. The dependence of the X-ray frequency, related to the energy by the relationship $f = E/h$ (where h is the Planck constant), on the atomic number Z was predicted by the Bohr model of the atom and then confirmed experimentally by Moseley, that creates the *Moseley plot*, reported in Fig. 2.2.

Element (Z)	K_{α_1}	K_{α_2}	K_{β_1}	L_{α_1}	L_{α_2}	L_{β_1}
C (6)	0.277					
O (8)	0.523					
Na (11)	1.042	1.042	1.070			
Si (14)	1.740	1.739	1.836			
S (16)	2.308	2.307	2.465			
Cl (17)	2.622	2.621	2.816			
K (19)	3.314	3.311	3.592			
Ca (20)	3.691	3.688	4.015	0.341	0.341	0.345
Ti (22)	4.511	4.505	4.936	0.452	0.452	0.460
Mn (25)	5.899	5.888	6.490	0.637	0.637	0.649
Fe (26)	6.404	6.391	7.058	0.705	0.705	0.719
Cu (29)	8.048	8.028	8.905	0.930	0.930	0.950

Table 2.1: Energy $[keV]$ of the emission lines of few elements with low atomic number (Zschornack [45]).

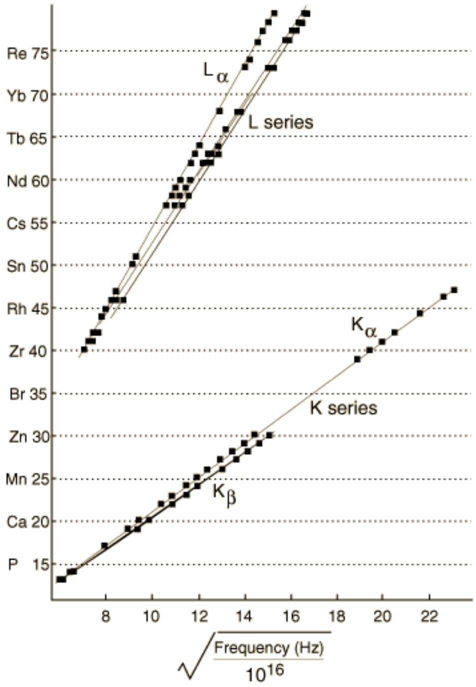

Figure 2.2: Moseley plot, the atomic number is plotted against the square root of the frequency of the emitted X-ray.

The correspondent equation is the *Moseley law* (Moseley [46]), that states:

$$E = R \cdot \left(\frac{1}{{n_f}^2} - \frac{1}{{n_i}^2}\right)(Z - \sigma)^2 \tag{2.1}$$

where R is the Rydberg constant (eV), n_f and n_i are the principal quantum numbers of the final and initial shell respectively, and σ is the shielding constant, that takes into account the atomic charge shielding effect due to the other atomic electrons. The energy difference between atomic inner-shell states increases with the atomic number. Thus, target nuclei with higher atomic number emit more energetic X-ray, as it can also be noticed from the values reported on Table 2.1.

The atomic X-ray emission is not the only process that can occur when an atomic inner-shell has to be filled. The excess energy can be transferred to another electron, which is subsequently ejected as *Auger electron*. The *fluorescence yield* ω represents the probability of a core hole in the inner shells being filled by an outer electrons while emitting a characteristic X-ray, in competition with the Auger non-radiative processes. It is defined, for a given transition from an excited state of a specified atom, as the ratio of the number of excited atoms which emit a photon to the total number of excited atoms. The contribution of the radiative process increases with the atomic number whereas the emission of Auger electrons diminishes in high Z element.

Cross-section

Inner-shell ionization processes can occur as a result of different excitation mechanisms. For X-ray physics, electron impact ionization, photoionization and ionization during proton or heavy ion impact are used for different applications. In general, for an efficient ionization the projectile must have an energy greater than the binding energy of the shells electrons and its velocity have to match the velocity of the electron in its orbit. The orbital velocity of inner-shells electrons is typically 1-10% of the speed of light and, in order to reach these velocities, electrons should be accelerated to few keV, protons to around 3 MeV and alpha particles to $\sim$ 15 MeV. Both keV electrons and MeV protons from small accelerators can be used to ionize efficiently the atomic electrons. Excitation with alpha particles (and any heavier ions) requires much higher energies. As already anticipated, given also the significant intensity of bremsstrahlung X-ray produced by electron beams, charged particles are the most common projectile for induced atomic X-ray trace elements analysis.

Efficient spectroscopy analysis using atomic X-ray emission relies on an accurate knowledge of the electron-shell ionization cross-sections. The ionization process of the inner-shells by incident charged particles has been described by different theoretical models, namely the *plane wave Born approximation* (PWBA) (Merzbacher and Lewis [47]), the *semi classical approximation* (SCA) (Garcia [48]) and the classical approach, also known as the *binary-encounter approximation* (BEA) (Choi [49]). Based on some physical corrections, the PWBA theory has been further developed to give rise to the *Energy-Loss Coulomb-Repulsion Perturbed-Stationary-State Relativistic Theory* (ECPSSR) (Brandt and Lapicki [50]). Calculated K and L shell ionization cross sections as a function of the target atomic number for protons of 1.5 and 3 MeV are shown in 2.3.

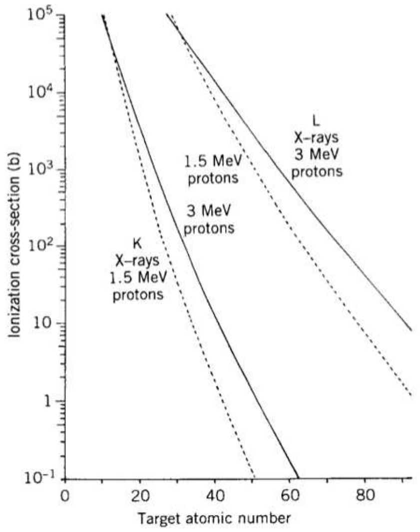

Figure 2.3: Calculated cross-sections for K and L shell ionisation as a function of sample atomic number for 1.5 MeV protons (dashed lines) and 3 MeV protons (solid lines) (Watt and Grime [51]).

Considering scattering from an equal element, cross section increases with the energy of the beam while, for a fixed energy, it has a smaller value if the mass of the target element gets heavier, because it is required an higher energy for the ionization of the inner-shells.

2.1.2 Elements Yield

High-precision quantitative analysis on the elemental concentrations of the analyzed specimens are exploited by PIXE if the values of the experimental parameters are accurately known. In fact, emitted X-rays caused by the proton induced ionization of atomic electrons, are collected in the correspondent PIXE spectrum which displays the total number of X-ray detected for each energy (Fig. 2.4).

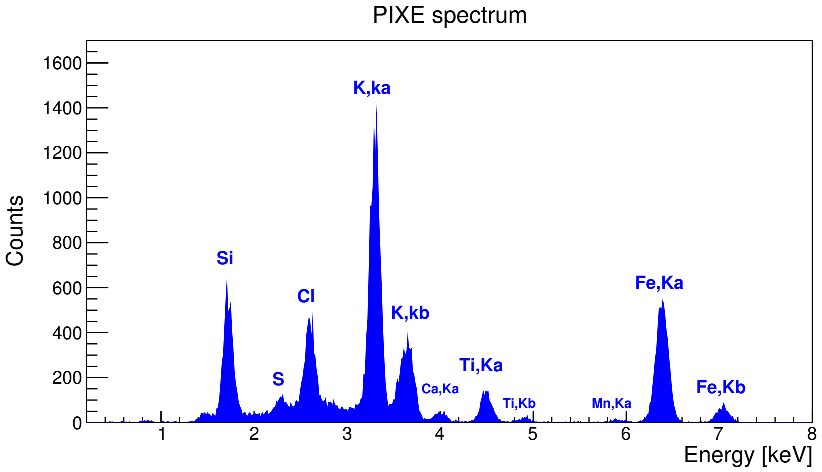

Figure 2.4: PIXE spectrum of the analysis of a polypropylene sample with deposit on the surface. Peaks of the main emission lines of several elements are present: Si, S, Cl, K, Ca, Ti, Mn and Fe (See Table 2.1).

In correspondence of the characteristic energy of the principal lines (K_{α_1} or K_{β_1}) of the elements that compose the sample, peaks of various height can be found. The counts on the PIXE spectrum related to the peak of the element Z (atomic mass A) is called *yield* $Y_P(Z)$. To estimate the elemental concentration N_z ($atoms/cm^3$) of the element, precise knowledge of the ionization cross section $\sigma_z(E)$, of the fluorescence yields ω and of branching ratios b is required. Furthermore, for thick targets, the overall stopping power of the sample matrix $S_M(E)$ and, if there are absorbers, the transmission coefficient t, have to be known. For the geometry shown in Fig. 2.5, with a homogeneous sample of intermediate thickness, the concentration of a specific element can be estimated from the elements PIXE yield, with the equation (Wang and Nastasi [52]):

$$Y_P(Z) = \omega \ b \ t \cdot \epsilon_P(E_z) \cdot N_z \cdot \frac{\Omega_P}{4\pi} \cdot N_p \cdot (1 - DTR_P) \cdot \int_{E_1}^{E_f} \frac{\sigma_z(E) T_z(E)}{S_M(E)} dE \tag{2.2}$$

Here, considering a general experimental setup, E_1 is the initial ion energy, and E_f, is the final energy on exit from the sample. E_Z is the emitted X-ray energy. Ω_P is the detector solid angle, $\epsilon_P(E_Z)$ is its relative efficiency, DTR_P the detector dead time ratio and N_p is the number of incident protons. The quantity $T_z(E)$ describes the X-ray transmission from the successive depths in the matrix and it is given by (Wang and Nastasi [52]):

$$T_z(E) \ = \ exp\left[-\left(\frac{\mu}{\rho} \right)_p \frac{\cos\theta_1}{\sin\theta_{TO}} \int_{E_1}^{E} \frac{dE'}{S_M(E')} \right] \tag{2.3}$$

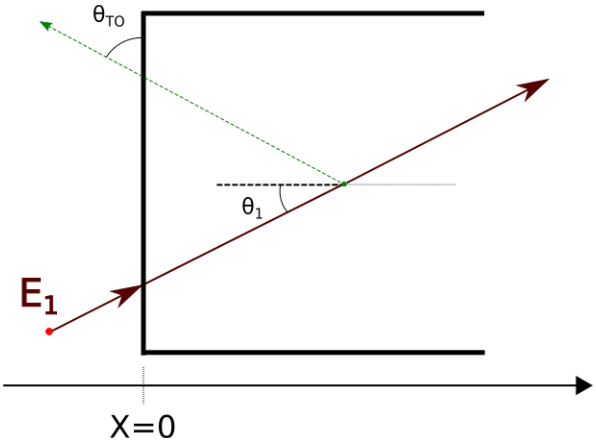

Figure 2.5: Scheme of PIXE experimental geometry. The incident particle enters the sample with an angle α respect the surface normal. After having ionize an atom, the particle is not deflected. The X-rays produced towards θ_{TO} (angle between the specimen surface and the specimen detector axis) are detected and contribute to the PIXE spectrum.

with $(\mu/\rho)_p$ is the concentration-weighted sum of the mass attenuation coefficients of the matrix elements in the sample matrix for the emission line p , θ_{TO} the angle between the specimen surface and the specimen detector axis (i.e., the x-ray takeoff angle) and θ_1 is the entrance angle between the incident beam and the sample normal. In Eq. 2.2, the dominant linear dependence of $Y_P(Z)$ on N_Z is modified by the integral term, known as the matrix correction, which can only be evaluated if the concentrations of all elements present are known. If the sample is thick enough to stop the proton beam completely ($E_f = 0$) the major elements (comprising 99.9%) and their concentrations in the matrix have to be known or be easily determined by other techniques, such as RBS or even simultaneous PIXE analysis using a second detector tuned for major elements.

On the other hand, when a specimen is so thin that proton energy loss and X-ray attenuation are negligible, the matrix effects drop out, and the integral in Equation 2.2 becomes $\Delta t/\cos\theta_1$, where Δt is the specimen thickness (Nastasi et al. [53]). Thus, there is a direct linear relationship between concentration of the element Z and its yield, as described in the following:

$$Y_P(Z) \; = \; \eta \; N_p \; N_Z \; \Delta t \tag{2.4}$$

Here, $\eta = \omega \; b \; t \cdot \epsilon_P(E_z) \cdot \frac{\Omega_P}{4\pi} \cdot (1 - DTR_P) \cdot 1/\cos\theta_1$ is a sensitivity factor (i.e., X-ray yield per proton per unit areal density for element Z).

Nevertheless, the matrix effects are physically simple and well understood and the underlying database accurately known and this gives PIXE a significant advantage, both for thick and thin samples, in contrast to other analysis techniques in which matrix effects are difficult to calculate and may not even be reproducible.

It should be mentioned that Equation 2.2 has neglected the incident beam *energy straggling* and *secondary fluorescence* contributions. When a beam of charged particles penetrates matter, the slowing is accompanied by a spreading of the energy distribution of the particles. This phenomenon is called energy straggling. It is due to statistical fluctuations in the number of collision processes. The omission of energy straggling of MeV protons is believed to change the predictions of the preceding equation by less than 0.1% and can be therefore ignored (Nastasi et al. [53]). However, the secondary fluorescence effect must be included in any code that generates X-ray yields from element concentrations, because it can raise uncertainties till the 20% on the results (caron Scaronmit et al. [54]). Secondary fluorescence occurs when the characteristic radiation produced in turn induces the X-ray emission of another element in the sample. This contribution may be accurately calculated for the various atomic shells using the quantities introduced before, together with the ionization cross-section relative to X-rays.

2.2 Rutherford Backscattering Spectrometry (RBS)

Rutherford backscattering spectrometry (RBS) has evolved from classical nuclear physics experiment conducted by E. Rutherford in 1911, that used the backscattering of alpha particles from a gold film to determine the fine structure of the atom, resulting in the discovery of the atomic nucleus. RBS as a method for materials analysis was then firstly described in 1957 (Rubin et al. [55]). The fundamental basis of RBS is the detection and analysis of the projectile ions which are backscattered after the interaction with the target nuclei that compose the sample matrix. Measurements of the number and energy distribution of these ions, provide the quantitative determination of the composition of a material and depth profiling of individual elements. Using RBS, accurate depth information (typically of a few percent, with 10–30 nm in depth resolution) about the stoichiometry, elemental area density, and impurity distributions in the near surface region of bulk materials and in thin films, are quickly and easily achieved. Depth profile information, that ranges typically about 2 μm for incident ^4He-ions and about 20 μm for incident protons, is obtained in a non-destructive manner. Furthermore, RBS does not require typically the use of standards and its analysis are insensitive to the sample chemical bonding. These properties have established RBS as a powerful and widely used technique for material analysis. To motivate RBS unique properties, a theoretical description of RBS technique, that relies on the classical model of the two-body elastic collision, can be found in this Section. The cross-section of the backscattering process is discussed followed by an explanation on the mechanisms that cause the ions loss of energy. With these concepts, a detailed description of the RBS capabilities to provide depth profiling and the elemental composition analysis are formulated.

2.2.1 The Kinematic Factor K

The theoretical scattering model that describes this technique raises from the assumption that the process is a two-body elastic collision between two isolated particles of masses M_1 and M_2. Thus, the binding energy of particle 2 in the target is neglected and the analysis is independent of the nature of the force between the particles (as long as energy is conserved). The scheme of the elastic process is presented in Fig. 2.6. The incident particle with mass M_1, atomic number Z_1 and kinetic energy $E_1 = \frac{1}{2}M_1{v_1}^2$, interacts with a nucleus of the sample, at rest in the laboratory frame ($E_2 = 0$), with mass M_2 and atomic number Z_2. After the scattering process, the projectile is deflected at an angle θ with kinetic energy ${E_1}'$ while the target nuclei is scattered through the recoil angle Φ with kinetic energy ${E_2}' \neq 0$. The energy ${E_1}'$ of the scattered projectile ion is determined by applying conservation of kinetic energy and of longitudinal and

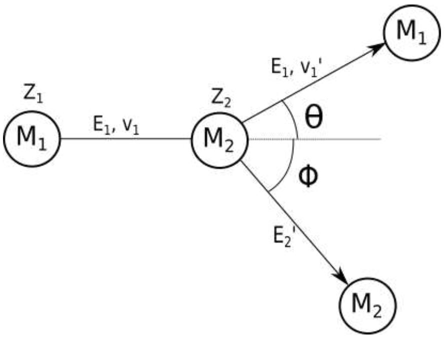

Figure 2.6: Scheme of the two-body elastic collision between a particle of mass M_1, atomic number Z_1 and energy E_1 and a second with mass M_2, atomic number Z_2 and energy E_2. The particle 2 is initially at rest in the laboratory frame. The impact cause the deflection of the projectile at an angle θ and with energy E_1', while the target nuclei is deflected at an angle Φ with energy E_2'

transverse momentum of the two-body system after the scattering process. Using the related equation, it is possible to obtain the ratio of the velocity of the scattered ion ${v_1}'$ and the original one v_1:

$$\frac{{v_1}'}{v_1} = \frac{M_1}{M_1+M_2}\cos\theta \pm \sqrt{\left(\frac{M_1}{M_1+M_2}\right)^2\cos^2\theta + \frac{M_2-M_1}{M_1+M_2}} \tag{2.5}$$

For projectile mass greater than the target mass ($M_1 > M_2$), there is a maximum scattering angle, θ_{max}, that obeys:

$$\cos^2\theta_{max} = 1 - \left(\frac{M_2}{M_1}\right)^2 \tag{2.6}$$

and $\theta_{max} \in [0, \pi/2]$ for $M_1 > M_2$. Only projectile ions that are lighter than the target nuclei can be backscattered. For this reason, in backscattering spectrometry technique, light elements such as ^4He and ^1H are often used for the ion beam.

For $M_1 < M_2$, taking the positive root of Eq. 2.5, it is possible to define the *Kinematic factor* K_{target} as the ratio between the energy before and after the interaction (Wang and Nastasi [52]):

$$K_{target} = \frac{{E_1}'}{E_1} = \left[\frac{\sqrt{1-(M_1/M_2)^2\sin^2\theta} + (M_1/M_2)\cos\theta}{1+(M_1/M_2)}\right]^2 \tag{2.7}$$

As highlighted by the subscript, this factor has an intrinsic dependence on the target element. Hence, for a known ion mass M_1, the energy loss after elastically colliding with the target atom, becomes a function only of the scattering angle θ and the target mass M_2. In the experimental setup for RBS analysis, the scattering angle is fixed by the experimental geometry, specifically by the RBS detector position. Therefore, the kinematic factor permits to recognize the element of the sample involved in the scattering process (given that the collision happens in the sample surface). In Fig. 2.7 it is reported the dependence of the kinematic factor on the mass of the target element, either for a proton and an α particle beam, for a fixed scattering angle of 140 °. In the plot, the K factors correspondent to the main elements are marked. As it can be noticed, backscattered protons lose less energy than ^4He ions when colliding with the same element nucleus. Furthermore, increasing the atomic mass of the target nucleus, the differences between kinematic factors of mass-adjacent elements become smaller. Regarding RBS

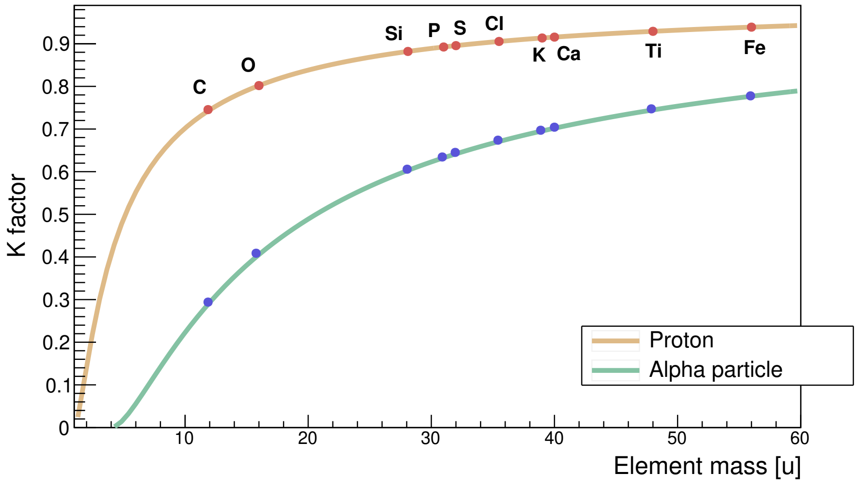

Figure 2.7: Plot of the kinematic factor in function of the atomic mass of the target element for a proton and an α particle beam and fixed scattering angle of 140°.

analysis, if this difference can not be resolved by the system resolution, there is an uncertainty in determining which element correspond to a certain event. Taken the first equivalence of Eq. 2.7, for fixed experimental geometry (θ constant) and constant beam energy E_1, the energy separation between two elements $\Delta E_1'$ is given by:

$$\Delta E_1' = E_1 \, \frac{dK}{dM_2} \, \Delta M_2 \tag{2.8}$$

with ΔM_2 the mass difference between the two elements. The mass resolution of the system δM_2 can be obtained by setting $\Delta E_1'$ to the minimum energy separation that can be resolved experimentally δE:

$$\delta M_2 = \frac{\delta E}{E_1 (dK/dM_2)} \tag{2.9}$$

The mass resolution varies considerably with the depth at which the interaction occurs: at the sample surface, δM_2 is mainly determined by the detector energy resolution, while at deeper layers the dominant component of δM_2 is energy straggling.

2.2.2 Scattering Cross-section

The probability of the projectile to be scattered at a certain angle depends on its energy. Almost all scattering processes of energy much below the coulombian barrier are mediated by couloumbian force and thus described by the Rutherford cross-section. In low energy regime screening process of the nuclear charge arise whereas, high-energy projectile can have nuclear reactions with the nuclei.

Rutherford Cross-section

Rutherford scattering refers to the elastic scattering of charged particles by the Coulomb interaction, with the projectile described by mass and atomic number M_1 and Z_1 and the target nucleus by the equivalent M_2 and Z_2. If the collision is mediated by the Coulomb force, the *differential scattering cross section* σ_R in the laboratory frame is given by (Wang and Nastasi [52]):

$$\sigma_R(E,\theta) = \frac{d\sigma(\theta)}{d\Omega} = \frac{e^4}{(8\pi\epsilon_0)^2} \cdot \left(\frac{Z_1 Z_2}{E_{bs}}\right)^2 \cdot \frac{1}{\sin^4(\theta/2)} \cdot \frac{(1+(M_1/M_2)^2 + 2(M_1/M_2)\cos\theta)^{3/2}}{1+(M_1/M_2)\cos\theta} \tag{2.10}$$

with θ the scattering angle in the center of mass frame, ϵ_0 the vacuum permittivity, e the elementary charge and E_{bs} the projectile kinetic energy, in the center of mass frame, just before the collision (eV). Higher energies particles are characterized by a lower scattering cross-section while, considering the atomic number of the projectile Z_1 and of the target nucleus Z_2, the quadratic dependencies show that the probability of scattering is higher for heavier beam and target.

Non-Rutherford Cross-section

Experimental measurements indicate that actually cross section departs from the Rutherford values at both high and low energies for all projectile-target pairs. The *low-energy* departures are caused by partial screening of the nuclear charges by the electrons shells surrounding both nuclei. This is taken into account introducing a screening function χ in the Coulomb potential

$$V(r) = \frac{Z_1 Z_2 e^2}{4\pi\epsilon_0 r} \cdot \chi \tag{2.11}$$

where r is the distance between the two nuclei and e the elementary charge. With $\chi = 1$ the unscreened Coulomb potential is described. Many different screening functions exist and each defines a different correction factor F for the screened interaction cross-section σ_S:

$$\sigma_S(E,\theta) = F(E,\theta) \cdot \sigma_R(E,\theta) \tag{2.12}$$

Experimental results agree especially with two particular correction factors, *L'Ecuyer factor* (L'ecuyer et al. [56]) that represents a first order correction that does not take into account the scattering angle θ, and the *Anderson* factor (Andersen et al. [57]) that acknowledges the angular dependence of the screening in the Rutherford cross-section. Nevertheless this correction is estimated to affect only ~ 3 % of the results (estimation for 1 MeV ^4He ions on Au atoms). The energy at which electron screening effects become important can be estimated requiring that a parameter called the distance of closest approach, d, is greater than the K-shell electron radius. The distance of closest approach is given by

$$d = \frac{Z_1 Z_2 e^2}{4\pi\epsilon_0 E_1} \tag{2.13}$$

In this analysis, the K-shell electron radius can be estimated as a_0/Z_2 where a_0 is the Bohr radius. Using Equation 2.13 and the requirement that $d > a_0/Z_2$, the lower limit of the beam energy to not include screening effects is set. It results:

$$E_{NR}^{low} = \frac{Z_1 {Z_2}^2 e^2}{4\pi\epsilon_0 a_0} \tag{2.14}$$

This energy value corresponds to ~10 keV for ^1H scattered from Si ($Z_2 = 14$) and ~250 keV for ^1H scattered from Au ($Z_2 = 79$). Typical beams used for RBS analysis have MeV energies and are out of the range of the screening process.

Conversely, the *high-energy* deviation from the classical Rutherford scattering is due to the existence of short-range nuclear forces. It becomes important when the distance of closest approach of the projectile-nucleus system is comparable to the nuclear radius. Although the size of the nucleus is not a uniquely defined quantity, early experiments with alpha-particle scattering indicated that the nuclear radius R_n could be expressed as:

$$R_n = R_0 A^{1/3} \tag{2.15}$$

where A is the mass number and $R_0 = 1.25 \cdot 10^{-15}$ m. From Eq. 2.13 and 2.15, imposing that d corresponds to R_n, a lower limit for the non-Rutherford cross section to become important in the scattering process is set:

$$E_{NR}^{high} = \frac{Z_1 Z_2 e^2}{4\pi\epsilon_0 R_0 A^{1/3}} \tag{2.16}$$

For ^1H ions incident on carbon, this energy is ~2.5 MeV. For a few MeV beam of protons is thus possible to observe effects due to the non-Rutherford cross-section involving nuclear processes.

Recent measurements and calculations regarding the onset of these high-energy departures result in the following formula that gives the energy E_{NR}^{high} above which deviations from Rutherford gets $> 4\%$ (Bozoian et al. [58]):

$$\begin{aligned} E_{NR}^{high} &= \frac{M_1 + M_2}{M_2} \cdot \frac{Z_2}{10} \qquad && \text{for } Z_1 = 1 \\ E_{NR}^{high} &= \frac{M_1 + M_2}{M_2} \cdot \frac{Z_1 Z_2}{8} \qquad && \text{for } Z_1 > 1 \end{aligned} \tag{2.17}$$

It should be noted, however, that Eqs. 2.17 are not intended for high accuracy, and deviations up to 500 keV may occur. Threshold energies E_{NR}^{high} are shown in Fig. 2.8 for ^1H, ^4He and ^7Li projectiles and different target atomic numbers Z_2.

The straight line in Fig. 2.8 represents a rough boundary separating the region of Rutherford behaviour (below the line) from the region where the cross section deviates from Rutherford by 4% (above the line), for each impinging ions. For ^1H particles impinging in carbon atoms non-Rutherford scattering effects should be visible below 1 MeV. Therefore, these effects can be observed during the following analysis and they have to be included in the RBS spectrum simulation.

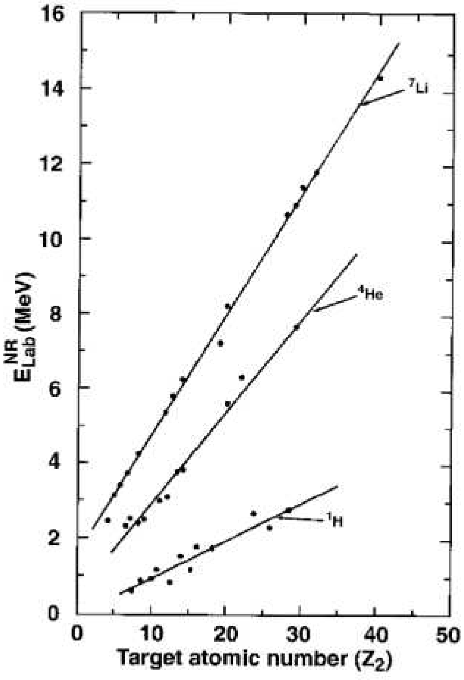

Figure 2.8: Laboratory projectile energies, E_{NR}^{high}, at which backscattering cross-sections deviate from Rutherford by 4% (for $\theta > 160°$) for ^1H, ^4He and ^7Li projectiles. Straight lines result from a least squares fit to experimental or optical model calculation data, see Eqs. 2.17 (Tesmer and Nastasi [59]).

2.2.3 Ion Energy Loss

The capability of characterize the analyzed sample in depth relies mainly on the energy loss of the analysis beam ions as they traverse the specimen. The *stopping power* of a material is usually defined as the energy loss per distance travelled by a particular ion in the material and is denoted as dE/dx. The energy loss process occurs mainly through successive *electronic collisions*, in which the projectile kinetic energy is lost through the excitation of atomic electrons. These collisions impart small energy losses and small angle deflections to the ion projectile. Less frequent are the *nuclear collisions* that refer to the elastic collisions between the projectile ion and nuclei in the sample (that is the reason of the established designation "nuclear", no nuclear forces are involved in these processes). In these collisions, responsible for the backscattered events detected in RBS analysis, the incident particle energy loss is large and discrete and the projectile is deflected at large angle. Considering these two terms, the stopping power $S(E)$ can be written as:

$$S(E) = \frac{dE}{dx} = \left.\frac{dE}{dx}\right|_e + \left.\frac{dE}{dx}\right|_N \tag{2.18}$$

where the subscript e stands for "electronic" and N for "nuclear". A comparison between the electronic and nuclear energy loss can be seen in Fig. 2.9. The values of $S(E)$ refer to an oxygen projectile impinging in an aluminium target. This simulation has been provided by the software *SRIM* (Ziegler [60]).

At ion velocities v that are significantly lower than the Bohr velocity of the atomic electrons $v_0 = e^2/\hbar = 2.2 \cdot 10^6\ m/s$, the ion carries its electrons and tends to neutralize by electron capture.

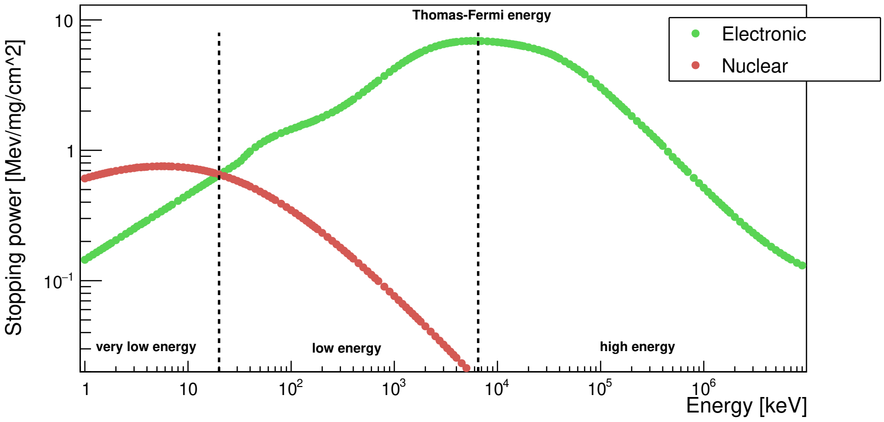

Figure 2.9: Stopping power in function of the projectile energy. Values are estimated by the simulation software SRIM. In this specific case, it has been selected an O projectile and on Al target.

The correspondent energy to the Bohr velocity, for ${}^{16}O$ ions, is $\sim 400\ keV$, estimated using the relationship $E = \frac{1}{2}mv^2$.
At very low velocities, elastic collisions with the target nuclei, that is nuclear energy loss, dominate. As the ion velocity increases, the nuclear energy loss diminishes as $1/E$. Simultaneously, electronic energy loss soon becomes the main interaction and dominates in the low-ion-velocity range, that is from $v \sim 0.1v_0$ to $v \sim {Z_1}^{2/3}v_0$. The incident ion is not fully stripped of its electrons, with an effective charge smaller than Z_1e, and still tends to neutralise its charge by electron capture. Nuclear collisions are negligible compared to the electronic ones. In these conditions the electronic energy loss is approximately proportional to ${E_1}^{1/2}$, increasing with the energy until reaching its maximum rate, occurring at the ion *Thomas-Fermi velocity* $v_{TF} = {Z_1}^{2/3}v_0$. For the oxygen projectiles considered in Fig. 2.9, $v_{TF} \sim 8.8 \cdot 10^6\ m/s$ and $E_{TF} \sim 6.5\ MeV$. In the high-energy regime, finally, the projectile ion is completely stripped of its electrons and behaves as a positive charge Z_1e. The rate of its electronic energy loss in this regime can be characterize in terms of close, high momentum transfer collisions with electrons, when the ion is within the electronic orbitals and distant, low momentum transfer collisions when the ion is outside the electron shells. This behaviour is described by the *Bethe-Block* formula in the non relativistic approximation (Breese et al. [61]):

$$-\left.\frac{dE}{dx}\right|_e = \frac{4\pi e^4}{m_e} \cdot \frac{n_e {Z_1}^2}{{v_1}^2} \cdot \ln\left(\frac{2m_e {v_1}^2}{I}\right) \tag{2.19}$$

In this formula, the notation is the same used previously. n_e is the number of electrons per unit volume, m_e is the electron mass and I is the mean excitation potential. In this regime, the rate of ion electronic energy loss decreases with increasing energy. To be noticed that, given the proportionality on Z_1^2, heavier ions are subjected to an higher loss of energy than lighter ones when traversing the same depth in the sample.

Light ions are characterized by a keV Thomas-Fermi energy, 25 keV for protons and 250 keV for ${}^4He$. Therefore, for MeV light ions beam, the stopping power is included in the high-energy regime and it is dominated by electronic collisions. Nuclear collisions have a contribution up to

5 orders of magnitude lower. The two contributions to the energy loss are discretized in Fig. 2.10 in function of the depth of the projectile in the sample, considering ^1H and ^4He ions beam in Si.

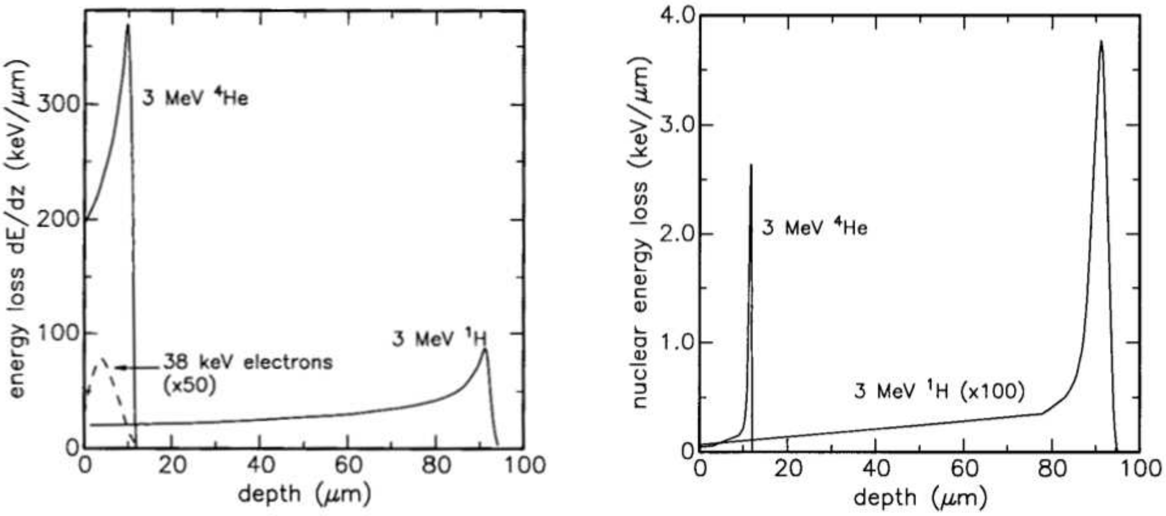

(a) Electronic energy loss

(b) Nuclear energy loss

Figure 2.10: Average electronic (a) and nuclear (b) energy loss for 3 MeV ^1H ions and 3 MeV ^4He ions in amorphous silicon as a function of ion penetration. In the nuclear components, the lines that refers to protons is been multiplied per 100 (Breese et al. [61])

As it can be seen, in this specific case, nuclear contribution is 2 and 4 order of magnitude lower, respectively for alpha particles and protons. From the graphs illustrated in 2.10, while crossing the sample, the energy loss rate increases with the depth until reaching a maximum, known as *Bragg peak*, before coming to rest (if the sample material is thick enough). These considerations are generally valid for every ions beam as it can also deduced from the oxygen cross-section behaviour simulated in Fig. 2.9. The dependence of the energy loss on the depth reached in the sample by the projectile allows then to estimate the ions *range* R_p, that is the total distance along the beam direction travelled by the particle p before coming to rest. R_p is given by:

$$R_p = \int_0^{E_1} \frac{1}{(dE/dx)} dE \tag{2.20}$$

Eq. 2.20 can only give an estimation of the range of the ion beam, since statistical variations affect either the exact number and the geometrical after-effect of the collisions that the incident ions sustain. As such, the initial mono-energetic beam ions are dispersed after traversing a given length in the sample material. This phenomenon is titled *energy straggling*. The energy straggle effect causes also the variation of the range of different ions traversing the target, denoted as *longitudinal straggling*. Furthermore, each single particle can have different trajectory through the sample material, associated, in particular in the transverse plane, to the transverse momentum that is provided to ions. This phenomenon is termed *lateral straggling*. Fig. 2.11 present Monte Carlo simulations of the trajectories of ^1H and ^4He ions through a carbon target, obtained using SRIM. From the simulation results a total longitudinal straggling of 1.25 μm and 0.11 μm for protons and α particles respectively. The total lateral straggling, instead, is

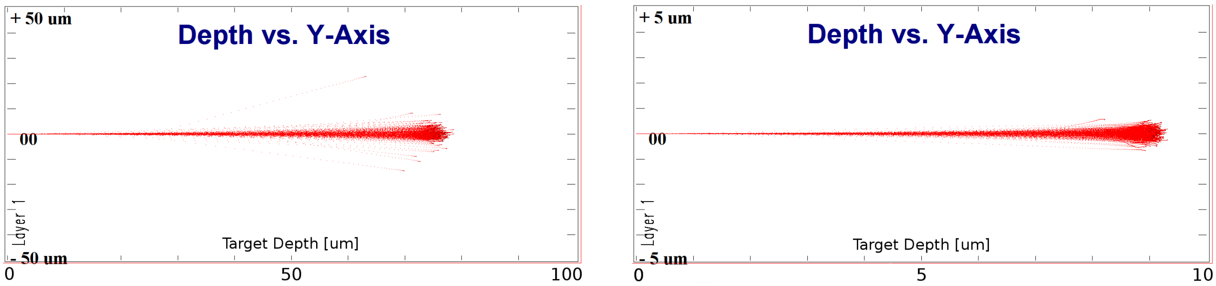

(a) Protons

(b) α particles

Figure 2.11: Simulation of the trajectories of a 3 MeV proton (a) and helium (b) beam in a carbon target. For protons, the target is 100 μm while for ^4He is 10 μm. To be noticed that the lateral scale is different in the two graphs.

of few μm for the ^1H beam and of $\sim$ 500 nm for ^4He. However, considering an equal depth in the target (5 μm for instance), protons present less straggling compared to helium ions. The consideration of these effects are quite important in the planning of ion beam analysis, since they set a fundamental limit to the depth and lateral resolution attainable. Helium ions beam is characterized by larger cross-section for the collisions process and can provide a better resolution in the results of RBS analysis. On the other hand, the shorter range of the heavier ions permit to analyze the sample only for a limited depth. If the analysis aim to investigate the depth profile of a thick sample, protons are preferable even because their straggling effect is lower. Still, the lateral and the depth resolutions obtained by light MeV ion beam analysis are a significant improvement over electrons analysis, and prove RBS to be a powerful tool in attaining high-resolution depth information of an unknown sample.

2.2.4 Depth profiling

Undoubtedly, the most interesting capability of RBS analysis resides in its ability to probe the inner structure of a given sample, not only on a surface level but also as a function of its depth. The physical process intrinsically related to this capability is, in particular, the loss of energy by the projectile while crossing the medium. The beam ions are characterized by their dE/dx, that, considering the in- and out-coming trajectories of the particles, enable the extraction of depth information from the sample. Figure 2.12 schematizes the backscattering process.

The particle enters in the sample with an energy E_1 and an angle θ_1 respect to the surface normal. After having traversed a depth x_t in the material, it is backscattered at an angle θ_s, losing a fraction of its energy given by the kinematic factor. In order to be detected and contribute to the RBS spectrum, it then goes through the sample until it emerges off at an angle θ_2 respect to the normal of the sample surface. The ion loses an energy ΔE_{in} along its path into the sample and ΔE_{out} along its path out of the sample, where

$$\Delta E_{in} = \int_0^{x_t/\cos\theta_1} \left.\frac{dE}{dx}\right|_{E_1} dx \qquad \Delta E_{out} = \int_{x_t/\cos\theta_2}^{0} \left.\frac{dE}{dx}\right|_{E_s} dx \tag{2.21}$$

in which the subscripts E_1 and E_s stand for the energy values from which the energy loss has to be evaluated. The first is the ion energy before entering the sample while E_s is its energy just after being scattered, $E_s = K_{target}(\theta_s) \cdot (E_1 - \Delta E_{in})$, where $K_{target}(\theta_s)$ is the kinematic factor

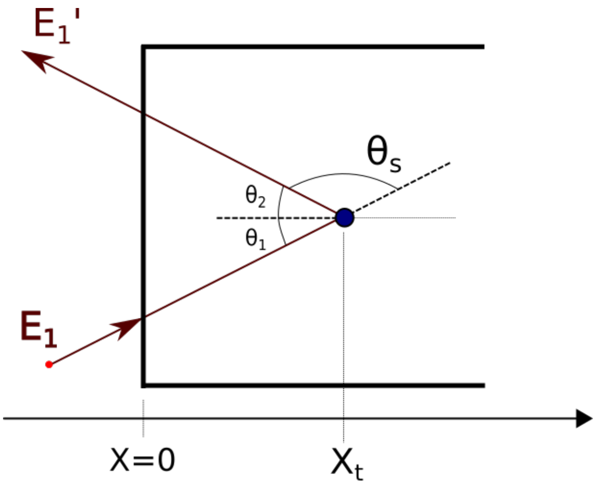

Figure 2.12: Scheme of a backscattering event at a depth x_t in the sample. The incident particle enters the sample with an angle θ_1 respect the surface normal and is backscattered at an angle θ_s. The exit angle respect to the surface normal is θ_2. The energy of the out-going particle is ${E_1}'$

given in Eq. 2.7, that depends directly on the backscattered angle θ_s and the target nucleus. The measured backscattered ion energy ${E_1}'$ from a given element at a depth x_t is thus

$$
{E_1}' = K_{target}(\theta_s) \cdot (E_1 - \Delta E_{in}) - \Delta E_{out} \tag{2.22}
$$

Using the proper rates of ion energy loss and kinematic factors, the energy spectrum of the collected backscattered ions can be converted to the depth profile of each element of the sample.

For thin films, in which the maximum collision depth is $\sim 100\ nm$, it is possible to perform analytical estimations using the *surface energy approximation*, that consists in assuming the stopping power in both paths through the sample constant. In particular, ΔE_{in} refers to the energy loss of a particle with energy E_1 and ΔE_{out} to a particle with energy E_s:

$$
\Delta E_{in} = \frac{dE}{dx}(E_1) \cdot \frac{x_t}{\cos\theta_1} \qquad \Delta E_{out} = \frac{dE}{dx}(E_s) \cdot \frac{x_t}{\cos\theta_2} \tag{2.23}
$$

For thicker films, instead, a better approximation, named *mean energy approximation*, consists in evaluating the energy loss at a mean energy between the initial and the final energies of the two paths, precisely $E_{in} = (2E_1 - \Delta E_{in})/2$ and $E_{out} = (2E_s - \Delta E_{out})/2$. Evaluating the energy loss according to one of these approximation, for a single-element samples, the energy difference at the detector ΔE_x, between ions backscattered at the sample surface and at a depth x_t, is estimated by:

$$
\Delta E_x = [E_f] x_t \tag{2.24}
$$

where $[E_f]$ is named the *energy loss factor*, given by:

$$
[E_f] = \left[K_{target} \cdot \frac{dE}{dx}_{in} \cdot \frac{1}{\cos\theta_1} + \frac{dE}{dx}_{out} \cdot \frac{1}{\cos\theta_2} \right] \tag{2.25}
$$

Here it is not reported the precise energies at which the energy losses are evaluated since depend on the approximation used. The target nuclei depth x_t at which a single event occurs can be estimated using Eq. 2.24 and Eq. 2.25, once it has been calculated the energy loss factor and ΔE_x measured.

Usually, RBS analysis results are expressed in terms of *areal density* ($atoms/cm^2$) and, as such, the difference ΔE_x can be also defined by:

$$\Delta E_x = N_Z[\epsilon]x_t \tag{2.26}$$

where N_Z is the atomic density ($atoms/cm^3$) of the Z element and $[\epsilon]$ is named the *stopping cross section factor*, given by:

$$[\epsilon] = \left(K_{target} \cdot \epsilon_{in} \cdot \frac{1}{\cos\theta_1} + \epsilon_{out} \cdot \frac{1}{\cos\theta_2} \right) \tag{2.27}$$

ϵ_{in} and ϵ_{out} are the equivalent, respectively, of the quantities $\frac{dE}{dx}_{in}$ and $\frac{dE}{dx}_{out}$. They are called the *stopping cross-sections* and are defined as:

$$\epsilon = \frac{1}{N}\frac{dE}{dx} \tag{2.28}$$

The definition of the stopping cross-section factor allows to make depth considerations about multi-elemental samples, in which the question of the way to take into account the contribution of the different elements to the global energy loss mechanism arises. In fact, a linear additivity rule of stopping cross-sections in compounds can be used, on the assumption that the interaction processes between ions and component target elements are independent of the surrounding target atoms. This is called *Bragg rule* and, for the stopping cross-section ϵ^{AB} of the compound A_mB_n, can be written as (Wang and Nastasi [52]):

$$\epsilon^{AB} = m\epsilon^A + n\epsilon^B \tag{2.29}$$

where $m + n$ is normalized to unity and ϵ^A, ϵ^B are respectively the stopping cross-section that correspond uniquely to the element A and B. The depth-energy relation for samples with multiple elements of concentration N_{AB} can be found in the following way. The energy loss in the entrance path, before the scattering process, is equal either the projectile would collide with the element A or B and it is given by ϵ^{AB}. The kinematic factor depends on the particular nuclei i that is involved in the scattering and thus has to be replaced with the correct values, K^i_{target}. Lastly, the energy loss through the exit path depends on the energy of the particle just after being scattered. $\epsilon^{AB}_{out,i}$ is the stopping cross-section of the ion after being scattered with the i element, thus estimated using the kinematic factor that characterizes that collision. Considering scattering events with the element A, the depth-energy relations are given by:

$$\Delta E_A = [\epsilon]^{AB}_A N_{AB} x_t \tag{2.30}$$

$$[\epsilon]^{AB}_A = \left(K^A_{target} \cdot \epsilon^{AB}_{in} \cdot \frac{1}{\cos\theta_1} + \epsilon^{AB}_{out,A} \cdot \frac{1}{\cos\theta_2} \right) \tag{2.31}$$

with similar relations for the other element B.

Using these relationships between the energy of the backscattered ions and the depth of the nucleus involved in the scattering process, depth structure information are deduced from the RBS spectrum, that displays to number of events collected in function of their energies. Typical example of RBS spectrum, simulated with RUMP (Doolittle [62]), is illustrated in Fig. 2.13.

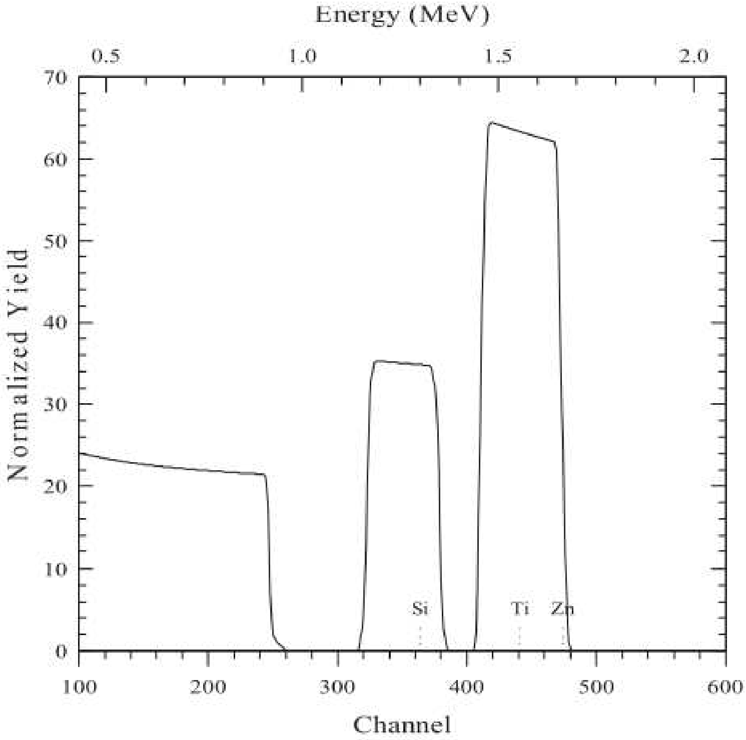

Figure 2.13: RBS spectrum simulated with RUMP and taken from (Corni and Michelini [63]). The sample is composed by a Zn layer on top of a titaniums, each of 150 nm. The substrate is composed by Si. The beam is composed by 2 MeV ^4He ions and the scattering angle set to 120°. The spectrum is normalized to the scattering cross section (*Normalized yield*). The expected energy positions of the single elements at the surface are marked.

The sample has a Si substrate on which there are two 150 nm layers of Ti and Zn. In the RBS spectrum, the edge at higher energy of the right peak corresponds to ^4He ions that have lost energy uniquely for the collision with surface zinc atoms and is determined by the related kinematic factor. Consequently Zn atoms constitute the upper layer. Its thickness can be derived looking at the width of the considered peak in the spectrum, that represents ΔE_{Zn} of Eq. 2.30. The right edge of the peak at lower energy, instead, is given by the contribution of the Ti atoms closer to the surface. ^4He ions lose energy passing through the Zn layer before and after being backscattered from one of those atoms. Thickness information is again related to the peak width (ΔE_{Ti}). Finally, the ions backscattered from Si atoms have the lower energies since $K_{Si} < K_{Ti}$, K_{Zn} and they go through the upper layers in the in-coming and out-coming paths. The shape in the spectrum of the silicon-backscattered ions peak, without a left barrier, is sign that the substrate is thick and only a lower limit for its depth length can be estimated.

2.2.5 Sample Composition Determination

The RBS technique enables also the determination, with considerable precision, of the stoichiometry of the sample elemental matrix. Considering a uniform beam of normal incidence on an uniform sample surface, the numbers of backscattered ions detected after interacting with a layer of atoms with mass A of thickness Δt, uniformly distributed with concentration N_A, is given by:

$$Y_R(A, \Delta t, \theta_s) = \epsilon_R \cdot \frac{\Omega_R}{4\pi} \cdot N_p \cdot N_A \; (1 - DTR_R) \cdot \int_0^{\Delta t} \sigma_R(E(x_t), \theta_2) dx_t \qquad (2.32)$$

where $\sigma_R(E(x_t), \theta_2)$ is the scattering cross section at angle θ_2 evaluated at ion energy $E(x_t)$, with x_t the depth of the involved target atom. Using beam energies typically in the order of few MeV, the scattering cross section can be assumed to be the Rutherford (Eq. 2.10). N_p is the measured number of incident particles, DTR_R the detector dead time ratio, Ω_R its solid angle and ϵ_R the efficiency. Eq. 2.32 can be efficiently used if in the spectrum, the full peak of the considered element can be resolved, so that the element concentration N_A can be estimated. Y_R, in a RBS spectrum like the one of Fig. 2.13, is simply given by the area under the peak of a certain element. The integral in the correspondent energy range then furnishes, using Eq. 2.32, the elemental concentration. However, many multi-elemental samples generate an RBS spectrum in which is possible that the total area of the i element, N^i_{RBS}, is not of easy determination since signals related to scattering events with different elements can have similar energies. This is the case of the presence of elements characterized by kinematic factors with close values in homogeneous samples. Alternatively, in layer-structured samples, even if the difference of the elements kinematic factors is large, the depth in which the atoms are placed can provide backscattered protons with similar energies, due to the energy loss along the trajectory in the sample. Nevertheless, in some specific cases of multi-elemental samples, the sample composition can be analytically estimated by comparing the edge heights related to the various elements of the backscattering yield spectrum, instead of the peak area. For example, this method gives a correct estimation when the sample is composed homogeneously by a two elements compound A_mB_n of concentration N_{AB}. Considering only the backscattering events at the sample surface, from the elements A and B, the heights of the correspondent edges in the RBS spectrum are (Nastasi et al. [53]):

$$\begin{aligned} H^A_R &= \epsilon_R \cdot \frac{\Omega_R}{4\pi} \cdot N_p \cdot (1 - DTR_R) \cdot \sigma^A_R(E_1) \; \tau_A \cdot m \; N_{AB} \\ H^B_R &= \epsilon_R \cdot \frac{\Omega_R}{4\pi} \cdot N_p \cdot (1 - DTR_R) \cdot \sigma^B_R(E_1) \; \tau_B \cdot n \; N_{AB} \end{aligned} \qquad (2.33)$$

where the cross section is evaluated at the incident particle energy E_1. τ_A, τ_B are the corresponding thicknesses of a slab of the target at the surface for elements A and B and defined by the energy resolution of the detecting system δE. Projectiles scattered from within τ_A and τ_B have a depth scale at the surface given by:

$$\delta E \;=\; \tau_A \; N_{AB} \; [\epsilon]^{A_mB_n}_A \;=\; \tau_B \; N_{AB} \; [\epsilon]^{A_mB_n}_B \qquad (2.34)$$

Combining equations 2.33 and 2.34, one obtains:

$$\begin{aligned} H_R^A &= \epsilon_R \cdot \frac{\Omega_R}{4\pi} \cdot N_p \cdot (1 - DTR_R) \cdot \sigma_R^A(E_1) \cdot m \cdot \frac{\delta E}{[\epsilon]_A^{A_m B_n}} \\ H_R^B &= \epsilon_R \cdot \frac{\Omega_R}{4\pi} \cdot N_p \cdot (1 - DTR_R) \cdot \sigma_R^B(E_1) \cdot n \cdot \frac{\delta E}{[\epsilon]_B^{A_m B_n}} \end{aligned} \tag{2.35}$$

The ratio of the atomic densities related to elements A and B can be written as:

$$\frac{m}{n} = \frac{C_A}{C_B} = \frac{H^A \ \sigma_R^B(E_1) \ [\epsilon]_A^{A_m B_n}}{H^B \ \sigma_R^A(E_1) \ [\epsilon]_B^{A_m B_n}} \tag{2.36}$$

Given the ratio of the stoichiometry coefficients of the two-elements sample, the chemical compound of the material can be identified. The backscattering spectrum of a compound sample that reflects these considerations is sketched in Fig. 2.14.

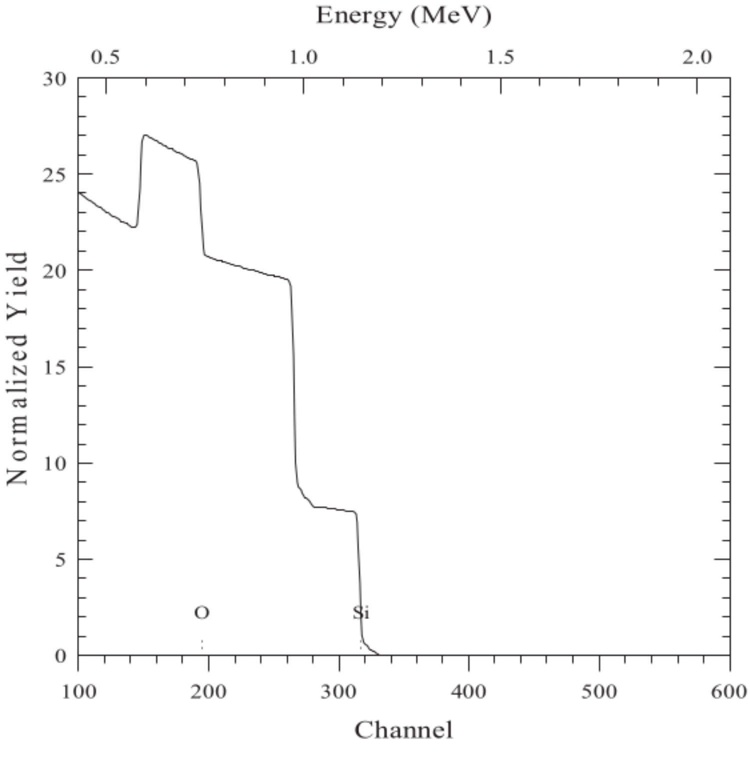

Figure 2.14: RBS spectrum simulated with RUMP and taken from (Corni and Michelini [63]). The sample is composed by a SiO_2 layer of 0.5 μm on top of a Si substrate. The beam is composed by 2 MeV ^4He ions and the scattering angle set to 120°. The spectrum is normalized to the scattering cross section (*Normalized yield*). The expected energy positions of the single elements at the surface are marked.

The sample is composed by a SiO_2 layer of 0.5 μm on top of a Si substrate. The energy spectrum consists of a superposition of the two signals generated by Si and O in the first layer of the sample and by Si in the substrate. The edge of each peak is defined by the correspondent kinematic factor K_i. For the example shown, since $K_{Si} > K_O$, the Si edge corresponding at surface events is at higher energy. Its height, H_R^{Si} can be easily estimated. In between the surface-Si and the O barriers it is present the edge corresponding to backscattered ^4He ions from the Si substrate.

H_R^O is evaluated considering the height of the edge at the correspondent energy and subtracting the Si-backscattered events at that energy, both from silicon atoms in the first layer and in the substrate. Knowing a-priori the scattering cross-sections and the stopping cross-sections for the involved elements, the composition of the upper layer can be then deduced using Eq. 2.36.

In multi-elemental samples that are characterized by a more complicated composition, especially when the chemical compounds inside the sample are more than one, in a multi-layer structure or in low concentrations, the estimation of the sample composition using this method can not be done. The edges correspondent to the various elements are not clearly distinguishable and, having different elements at different depth, there is also an ambiguity in determining to which element corresponds a specific event.

2.3 PIXE and RBS complementarity

IBA techniques, together with their characteristic features, present also limitations. Considering RBS and PIXE, the issues that raise using these techniques have already been discussed. For PIXE, when analyzing a thick sample, the elemental composition of the matrix is required in order to estimate the concentration of the elements. On the other hand, RBS analysis are not fruitful when they have to deal samples with complex structure, being either multi-elemental or multi-layered or even both. In these situations, the multiple variables that have to be considered, originate ambiguities in the RBS spectrum interpretation and, as a result, there is not a unique matrix that simulates properly the spectrum.

These limitations can be partially solved by clustering the two techniques. The analysis provided singularly, in fact, focus in different features of the sample. As such, combining the data, complementary and self-consistent results can be obtained. In particular, for PIXE and RBS, two different approaches are possible. The first consists in improving the PIXE estimation of the elements concentrations in a thick sample using the RBS capability of estimate the sample matrix and provide a correction to the measured charge, that may differs from the effective one. Vice versa, the RBS depth profiling evaluation can be improved limiting the possible matrices that fit the spectrum to the ones that produce also a PIXE simulation that is in agreement with the related data.

PIXE concentration estimation improvement

One of the approach that analyze the PIXE spectrum relying on the simultaneous RBS events is called *Q factor* method, from the name of the factor that provides the charge correction (Grime [64]). In detail, recalling Eq. 2.2 and the notation used in that formula, the total number of counts $Y_P(Z)$ in the reference line of a particular element Z, recorded in a PIXE experiment, can be also written as:

$$Y_P(Z) = \Omega_P \; \epsilon_P(E_z) \; N_z \; (1 - DTR_P) \; t \cdot Y_N(Z, M) \cdot \frac{Q}{f_Q} \tag{2.37}$$

Here, Q is the measured charge (μC) and f_Q is the Q factor, that is the ratio between the measured charge and the beam total charge that hit the target (Q_{TRUE}):

$$f_Q = \frac{Q}{Q_{TRUE}} \tag{2.38}$$

M is the set of parameters describing the sample matrix. It represents the modelization of the sample, including the number of layers, their thicknesses and compositions in terms of atomic percentages. $Y_N(Z, M)$ is the normalized target yield for the measured X-ray line of Z. From the yield definition given in Eq. 2.2, the normalized one is described as:

$$Y_N(Z) = \frac{\omega\ b}{4\pi e} \cdot \int_{E_1}^{E_f} \frac{\sigma_z(E) T_z(E)}{S_M(E)} dE \tag{2.39}$$

and, assuming that the fluorescence yield and the branching ratio of the considered emission lines are well known, it only depends on the sample composition through the stopping power $S_M(E)$ and the transmission coefficient $T_z(E)$. Therefore, the only unknown quantities to estimate the yield of the particular sample, and consequently the elemental concentrations, are the matrix composition, M, which allows Y_N to be calculated, and the Q factor, f_Q.

These quantities, as already anticipated, can be estimated from the simultaneous RBS spectrum collected during the PIXE analysis. In fact, in general, the total RBS yield, N_{RBS} can be calculated as the area of the related spectrum between two selected energy limits, E_1 and E_2:

$$N_{RBS} \; = \; \int_{E_1}^{E_2} Counts(E)\ dE \; = \; \epsilon_R\ \Omega_R\ (1 - DTR_R) \cdot \frac{Q}{f_Q} \cdot \int_{E_1}^{E_2} R(E, M, \theta) dE \tag{2.40}$$

where $Counts\ (E)$ is the number of events collected for a certain energy ($counts/MeV$) which, integrated over the energy, gives the RBS spectrum total area. In the second relation of Eq. 2.40, $R(E, M, \theta)$ ($counts/(MeV \cdot \mu C \cdot sr)$) represents the normalized simulation of the RBS spectrum, obtained modelling the sample through a matrix with specific M parameters. As before, Ω_R and ϵ_R are constants of the system, Q has, in principle, the same value as for the PIXE spectrum and DTR_R can be measured during the run. $R(E, M, \theta)$ can be then calculated using a dedicated software, that provides the sample composition parameters M that correspond to the best fit of the RBS spectrum. The M parameters of the best fit matrix can then be used as an input for the PIXE analysis program to estimate accurately the values of $Y_N(Z, M)$. Although this information is sufficient to provide the estimation of the element concentrations in that specific matrix, the absolute values of the element concentrations can be further correct using f_Q. This parameter is obtained as the ratio of the areas of the fitted over the experimental spectrum in a selected energy range.

This method has been demonstrated to be valid if the RBS spectrum is well-fitted and gives a proper evaluation of the sample matrix, without ambiguities (Grime [64]). Uncertainties can derive from the analysis of complex samples that require an elaborated structure model to fit the RBS spectrum or that may contains several heavy elements in unknown ratios, whom individual contribution to the spectrum may not be resolved.

RBS depth profiling improvement

RBS spectrometry can, in principle, determines the complete elemental depth profile of a sample from the energy spectrum of the scattered particles. However, the scattered particle energy is a function both of the mass of the target nucleus, and of the depth of the target nucleus in the sample. This ambiguity in the interpretation of the detected particle energy is the origin of the *inverse problem*. In particular, for a target whose composition varies continuously with depth, if straggling and multiple scattering effect are neglected, the contribution of each element at depth x_t to the RBS spectrum can be described by the following equation (Brice [65]):

$$\Phi_i(E_1, E_1', x_t) \;=\; \frac{N_i(x_t)\;\sigma(E_{bs}, \theta_s)\;\Delta\Omega}{K_i\;S(E_{bs}, x_t)\;+\;C\;S(E_s, x_t)}\left(\frac{\partial E_s}{\partial E_1'}\right)_{x_t} \tag{2.41}$$

where Φ_i is the number of projectiles with energy E_1 that are backscattered from the element i, with atomic number Z, at depth x_t and detected with energy E_1'. $N_i(x_t)$ is the concentration of the element i at depth x_t in the sample. $E_{bs} = E_1 - \Delta E_{in}$ is the beam energy before the backscattering process considered while $E_s = K_i \cdot E_{bs}$ is the energy just after the collision, estimated using the proper kinematic factor $K_i(\theta_s)$. $\sigma(E_{bs}, \theta_s)$ is the correspondent differential cross-section and $S(E, x)$ the stopping power, calculated with initial energy E and for a thickness x. $C = \cos\theta_1/\cos\theta_2$ is a geometrical parameter (see Fig. 2.12 for the angles notation). The measured spectrum yield, $N_{RBS}(x_t)$, for a precise ions beam energy E_1, due to the layer at depth x_t is the sum of the energy-integrated Φ_i for all the constituent elements i of the target:

$$N_{RBS}(x_t) = \sum_i \int dE\;\Phi_i(E_1, E) \tag{2.42}$$

Since, usually, there is no way to measure these individual partial spectra, is not easy to calculate analytically the inverse $N_i(N_{RBS}, x_t)$, that represents the concentration of the i element at depth x_t in the particular matrix. However, this information is necessary to estimate the depth profile of the sample.

There are softwares that reproduce the total RBS spectrum N_{RBS} from a certain matrix composition, evaluating the single Φ_i for each element. But, again, there may be different possible matrices that simulate properly the spectrum, considering that it is possible to combine variously the several variables that define the sample structure: which elements are present, the number of layers, the concentration of each element at every depth. To limit these solutions to the most meaningful, simultaneous PIXE data can be considered. For each matrices that provide a well-fitted RBS spectrum, Eq. 2.2 enables to estimate the PIXE yield for each specific element i included in the sample structure. If the estimated yield and the correspondent experimental peak area in the PIXE spectrum are not in good agreement for all the elements of the matrix, that solution is rejected. As such, the matrix solutions that best describe the sample are restricted to the ones that are self-consistent with the data regarding the two techniques. This approach revealed meaningful results for the sample structure in many different cases (Jeynes et al. [30]).

Chapter 3

Experimental setup, measurements and data analysis tools

In this Chapter, experimental instrumentation and procedures are presented. In particular, in Section 3.1, CTN microprobe system is described in detail, together with the accelerator and the beam line components. The experimental work needed to achieve the goals of this thesis is then illustrated in Section 3.2. The samples are plastics pieces exposed to water that have to be prepared for the microprobe analysis, selecting regions of interest for the analysis and making them suitable for the experimental setup. During the days in which the microprobe analysis are scheduled, preliminary operations in the beam line and in the microprobe have to be done in order to find the best condition of beam focus and intensity. Afterwards, samples analysis can be effectuated with different geometries, depending if it is intended to analyze their surface or their cross section. Acquired surface data are then analyzed using two dedicated software that cluster information from PIXE and RBS to estimate the elemental samples composition and their depth structure. Introduction to OMDAQ2007 and NDF, the two analysis softwares, is done in Section 3.3.

3.1 CTN Nuclear Microprobe

Material analysis using Ion Beam techniques are usually performed with a standard experimental apparatus. Specific instruments, different for every IB technique, are needed only at the sample chamber level. The various component of the CTN microprobe system, from the ions accelerator to the microprobe itself, are reported in the scheme of Fig. 3.1. The first essential component of any microprobe facility is the accelerator, responsible for boosting the ions to the desired energy. In order to obtain minimal probe resolution the accelerator should provide a stable beam current and a low beam energy spread, less than 100 eV per MeV (Breese et al. [61]). CTN is provided by a Van de Graaff generator that supplies an electrostatic high voltage of 2.5 MV. The accelerated particles can be deflected by the *switching magnet* in three distinct beam lines that bring to experimental stations with different purposes. The nuclear microprobe is set at the end of the central line, which provides a beam with the lower energy dispersion. The first *stabilizing slit* acts as a feedback for the accelerator and controls that the beam is stable and its direction parallel to the beam line. Afterwards, the 90° *bending magnet*

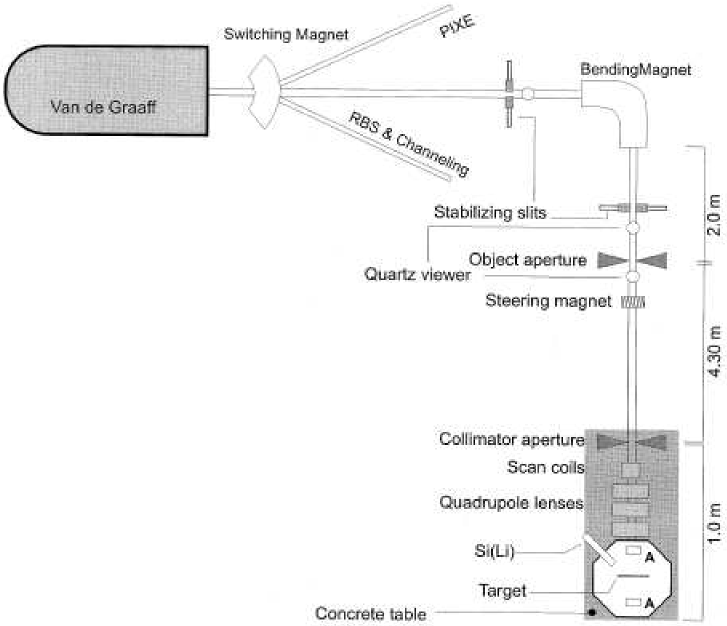

Figure 3.1: Scheme of the CTN experimental setup for microprobe analysis, from the accelerator, through the beam line and its components, to the microprobe system.

selects ions with a defined energy, by applying a proper magnetic field. A second stabilizing slit is placed soon after the bending magnet. Two sets of micrometer driven slits are used to select the size of the *object* and the *collimator* aperture that define, respectively, the beam area to be demagnified and to limit the divergence of the beam that enters the probe-forming lens system, while reducing the beam current. Each of these slit blade is a tungsten carbide cylinder polished to better than 1 μm. In between the two slits is placed the *steering magnet* with the essential function to optimise the beam intensity that is transmitted through the collimator aperture. With this magnet, little alterations in the beam trajectory, that could be due to an alteration of the beam energy, changes of the used ions or mechanical movements of beam lines components and supports, are easily compensated without a new mechanical alignment. Quartz mirrors placed along the beam line permit the user to visualize the particles beam with the aim of establish the optimal conditions of focusing and transmission. The final part of the microprobe can be seen in the photo of Fig. 3.2 that includes, in particular, the collimator aperture,

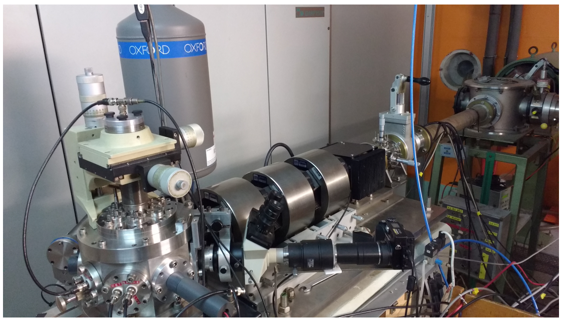

Figure 3.2: Photo of the microprobe setup installed at CTN. It is visible the last part of the beam line that ends in the microprobe. Scanning coils and quadrupoles triplet are placed before the sample chamber.

the scanning coils, the quadrupole focusing system and the vacuum chamber used. All the microprobe components have been developed and produced by *Oxford Microbeams*. The focusing system is provided by an high excitation magnetic quadrupole triplet, *OM150*, mounted on a precision micrometer controlled table for easy alignment (5 μm vertical and horizontal, and 50 μrad rotational alignment). The dimensions of the yokes are 100 mm long x 200 mm outside diameter while the bore radius is 7.5 mm for each quadrupole. Two independent units, OM52e, supply currents to the quadrupoles. As a result, the first two quadrupoles, grouped as C, focus the beam in the vertical plan (x,y) while the last one, CO, in the horizontal plan (x,z). The overall effect of the triplet, is to focus the beam in both directions (x,y with reference to Fig. 3.3) of the plan that corresponds to the sample one (*Sample plan*). The scanning system of the microprobe, composed by two coils, enables the scan of a selected area of the sample. The microprobe units dedicated to control this operation are the OM1010e and the OM40e. The former receives the signals generated to localize the point in which the beam is focused in the sample plane (x,y coordinate). These signals can have 256 discretized values each in the range 0-10 V. The standard scanning method is organized to associate 256 y values for every x value. The (x,y) signal is then forwarded to the OM40e unit, that generates a current signal up to 3.5 A to be transmitted to the coils in order to move the beam to the following point of the scan. With this procedure, the sample area of interest, are subdivided in 256 x 256 pixels and the beam is moved repeatedly on those points, being fixed in the x directions while translating in the y one for each x pixel. The upper current limit, provided to the coils by the OM40e unit, set also the scanned area maximum size, that is 2.6 x 2.6 mm^2 using 2 MeV protons.

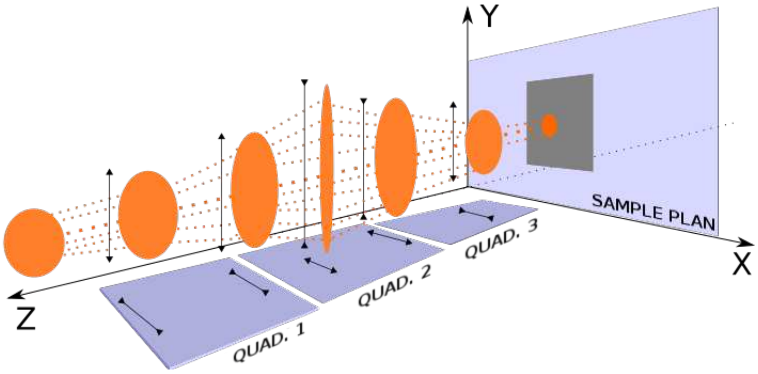

Figure 3.3: Schematic view of the beam focusing process. Traversing the first two quadrupoles the beam is focused in the vertical plan (x,y) whereas the last magnet reduces the beam dimensions in the horizontal plan (x,z). The overall result is to achieve the smaller size possible in the sample plan.

The body of the vacuum chamber design is an octagonal cylinder and a variety of interchangeable items can be inserted through ports on the flat faces. The samples are mounted on a stage which is fitted to the top flange of the chamber and different interchangeable stages are available depending on the application. With the fixed samples support, the beam hits the sample perpendicularly to its surface. An eucentric goniometer with translation and rotation in two axes is available for applications requiring the angle of the sample to be adjusted. Three micrometer enables to move the samples support inside when fixed in the chamber flange. In one of the lateral flanges is inserted a front viewing stereo zoom microscope at a backward angle of 45°, to operate a first step in the beam focusing operation and to help during the samples placement. The chamber is vacuum pumped using a diffusion pump coupled to a rotary vane pump, and a pressure of 10^{-6} $mbar$ is attainable. The microprobe lenses, scanning coils, collimator slits and vacuum chamber are mounted on a single concrete block, which rests on a layer of polystyrene to minimise the transmission of vibrations from the ground, that would decrease the spatial resolution of the beam.

The detecting system of CTN microprobe in the standard setup includes two detectors, one for X-rays, the other for back-scattered protons, in order to analyze simultaneously the sample using RBS and PIXE. The inside part of the chamber is visible in the photo of Fig. 3.4.

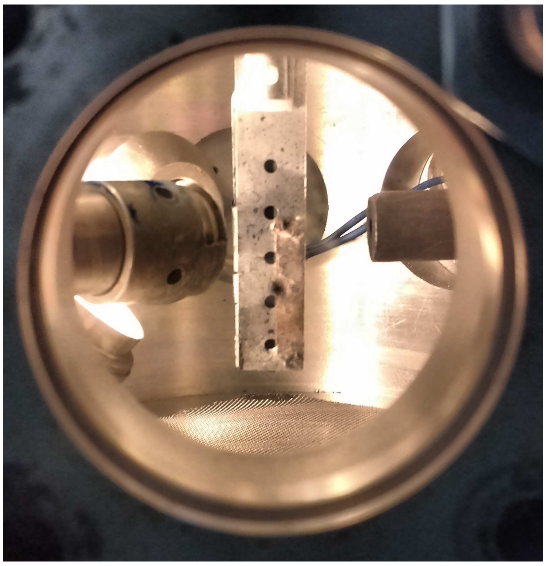

Figure 3.4: The sample is in the transversal section analysis setup. The beam hit them coming from the left side of the photo. From the beam point of view, in the photo are visible, on its right, the Si(Li) detector, on its left the microscope coupling. The Si surface barrier detector is placed below the beam entry position.

A *Link Analytical Si(Li) detector* with an active area of 80 mm^2, located at a backward angle of 45°, is mounted for PIXE analysis. The detector resolution is 145 eV. The distance from detector to sample can be altered and a minimum value of 25 mm can be reached. Several filters for X-rays can also be used, depending on which characteristic energies have the X-rays coming from the sample. These foils are used also to protect the active region of the detector, while stopping the scattered particles going towards it. Backscattering analysis are provided by a *Si surface barrier detector* with an active area of 200 mm^2 and 15 keV of resolution. It is located at a backward angle of 40° in the Cornell geometry and at a distance of 50 mm from the sample. Signals elaborated by the electronics dedicated to each detectors are read respectively by one of the eight analogic entrances of the OM1000e unit. This component, besides the analogic signals coming from detection events, receives also from the unit OM1010e the tension pulse correspondent to the (x,y) beam position and is furnished of two logic entrances that provide dead time corrections. A 12-bit $1\mu s$-conversion time ADC is used to analyze the energy signals while, the position ones are stored thanks to two 8-bit ADCs. Every event is thus stored digitally in the computer memory, using 3 bit to define the detector involved, 16 bit correspondent to the (x,y) beam position while the signal is recorded, and 12 bit for the energy information.

Data acquisition is carried out by a Oxford Microbeam proprietary software: OMDAQ2007 (Oxf [66]). RBS and PIXE spectra are generated online by this program while related events are collected. Furthermore, it displays 256 x 256 pixels elemental maps of the scanned area, showing the distributions of selected elements in that region. The maps generation is described taking as reference a specific element events detected in the PIXE spectrum, for example the 6.4 keV Fe characteristic X-rays. In the PIXE spectrum a energy range around 6.4 keV is set, referred to iron. If the energy of a detected X-ray is included in the defined interval, one count is added in pixel the Fe map corresponding to the (x,y) position of the beam. This allows to create a 256 x 256 pixels map correspondent to Fe, that shows the concentration of collected events coming from iron atoms in scanned area. Therefore, this map, represents the Fe distribution in the sample. The visualization of the element intensity in the map is provided by the colour code in Fig. 3.5. Maps can be created for every element, once the associated energy range is defined.

Figure 3.5: Maps colour code.

Also RBS events can be used, selecting in the correspondent spectrum the energy interval that includes the backscattered particles of a specific element. OMDAQ2007 enables to record all the maps created during the online analysis, as well as all the spectra obtained of the different techniques during the sample scan and a set of experimental information, such as the involved detectors, the scanned area dimension, the accumulated charge, the recording time and the beam particles type and energy. Different scan method can also be selected using the OMDAQ2007 interface. The scan of a selected area just described is the standard scan option and allows the maps creation. Different maps size can be chosen, up to 2.6 x 2.6 mm^2, and their shape can also be changed to whichever regular or irregular polygon. With the *point analysis*, instead, the beam is fixed only in a specific point of the sample, selected thanks to the maps given by an area scan that has to be previously done. *Linescans* option can also be chosen. The beam is moved along a predefined line creating, in this way, a 1D map of the distributions of each desired element. Complementarily to these standard acquisition modes, it exists the possibility to register the data in a event-by-event *listmode*. Every event is sequentially included in this file. This allows to obtain, during the offline analysis, information about region of interests of recorded spectra that were not considered during the data acquisition.

3.2 Materials and Methods

In order to study plastics weathering in aquatic environments, pieces of three different polymers are firstly exposed to the water of the Tagus river. After being retrieved, the samples are then prepared for the microprobe analysis. Interesting regions for the analysis are selected using magnifing lens and a microscope, cut using a surgical blade and adapted to the experimental setup. In the days dedicated for the data acquisition, preliminary operations have to be done to stabilize and focus the beam. Both surface analysis of the deposits on polymer samples and transversal analysis across the full depth of the samples are carried out using several beam scan options. Simultaneous RBS and PIXE events are analyzed with two dedicated softwares, OMDAQ2007 and NDF.

3.2.1 Preparation of polymer samples

Polymers that are commercialized in different everyday life products all over the world, such as high-density polyethylene, polyethylene terephthalate and polypropylene, are selected as samples. These polymers are significant to study because, being three of the most widely produced plastics, they represent a considerable fraction of the plastic that ends up in water environments. HDPE (CH_2), in particular, is an opaque plastic used in many products and packaging such as carry bags, detergent bottles, garbage containers and water pipes. PET ($C_{10}H_8O_4$) is transparent and mainly used in synthetic fibers for clothing and in packages for liquids and foods. PP ($(C_3H_6)_n$), finally, is a white thermoplastic polymer used in a wide variety of applications to include packaging for consumer products, plastic parts for various industries, special devices like living hinges, and textiles. Pieces of these polymers of approximately 5 x 10 cm^2 are exposed to turbid water of the estuary ecosystem of the Tagus river, near the confluence of the *Trancão* river in Lisbon. Samples are suspended in the water-column at the same depth and assessed through 30 days. After exposure, they are retrieved from the site and air dried. A photo of the sample at this stage of the operations can be seen in Fig. 3.6.

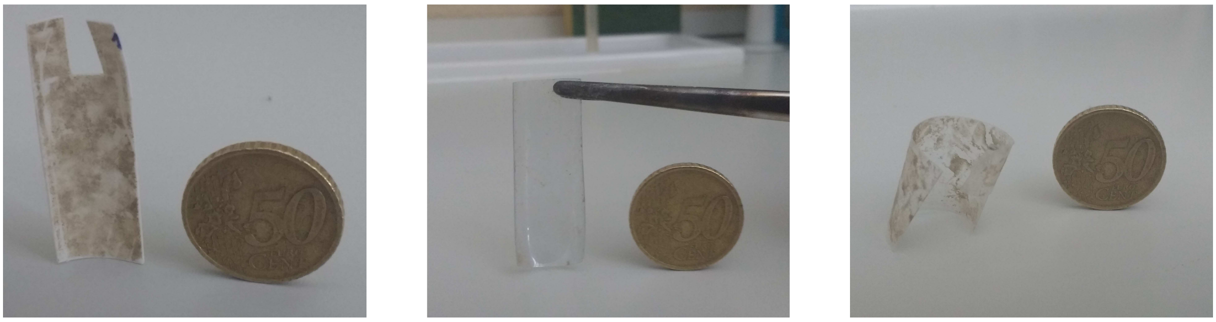

(a) HDPE (b) PET (c) PP

Figure 3.6: Photo of the plastics that have been immersed in the river. HDPE (a) is white while PET (b) and PP (c) transparent. The deposit on top of the surface is clearly visible in the HDPE and PP samples. The PET one shows, on the contrary, lower quantity of material deposited on top of the sample. The dimension of the plastics can be deduced with a comparison with the $\sim 24\ mm$ diameter standard placed in the photos.

Therefore, for the analysis of each of the three considered polymers, the available samples are: pristine plastics, to be used as controls, and samples with exposure time respectively of 7 and 30 days in the Tagus water.

Once decided which samples to analyze, it is necessary to select regions of particular interest and make them suitable for the microprobe analysis. Raw information about the type of deposits in the plastics surface are provided by looking at them with magnifing lens and a microscope. With these tools it is possible to discriminate regions on the plastics with low and high deposit and furthermore if it contains biotic (cells, biota) or mainly abiotic material (earth crust materials and saline compounds). In Fig. 3.7 are shown typical microscope images: blank plastic surface and details of biological and sedimental deposits on samples surface.

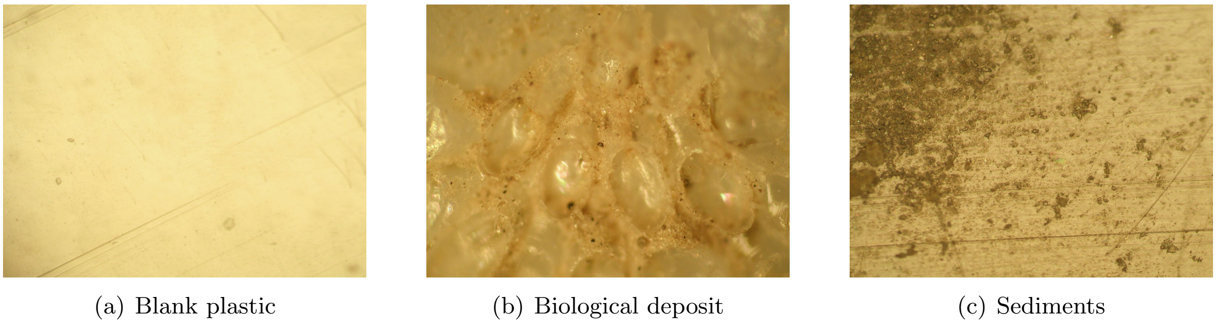
(a) Blank plastic (b) Biological deposit (c) Sediments

Figure 3.7: Photo of the surface of samples with different features. Pristine plastic (a) is clean from water deposit. Biota (b) can be identified from the shape and structure of the material, grouped with regular pattern. Sediment (c), instead, are characterized by an irregular distribution of different size and coloured particles.

Likely, the regions of interest to cross-section characterization, with high and low deposit, are identified and a clean cut is done using a surgical blade. Analysis area are chosen looking for areas without spread dirtiness due to the samples manipulation, with low or high deposits on the surface and where the plastic edge is as straight as possible, without apparent defects or roughness. Photo of an HDPE and a PET samples cross section can be seen respectively in Fig. 3.8 a and b, where is visible also some deposit on the surface.

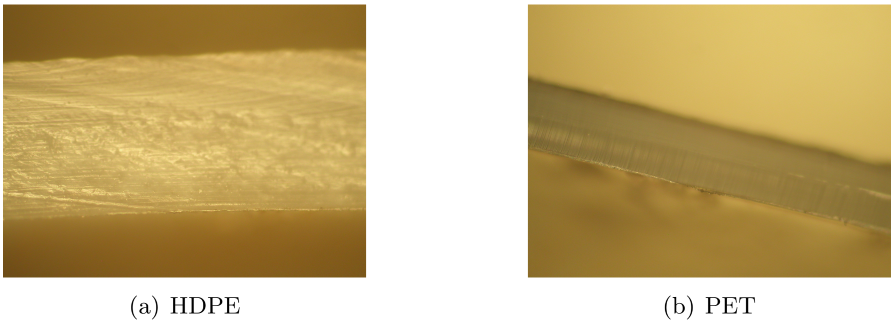
(a) HDPE (b) PET

Figure 3.8: Transversal sections images obtained with the microscope. HDPE sample (a) shows a non homogeneous structure while PET (b) seems to have a more uniform composition.

Regions of the samples selected for the analysis are cut in 0.5 cm^2 pieces and are carbon coated, using an adhesive graphite spray (Ach [67]), to avoid charge build up, that can introduce noise in the RBS and PIXE spectra.

3.2.2 Beam and microprobe settings

Initial adjustments of the microprobe conditions comprehend beam alignment, stabilization and intensity optimization using the several driven slits and quartz viewers placed along the beam line. The beam dimensions are then set using precision collimation slits and the magnetic quadrupoles. A quartz mirror and a 2000 mesh copper grid, positioned in the sample holder inside the chamber, permit to carry out the beam focusing procedure. Firstly, using the quartz mirror and the front viewing stereo zoom microscope, the quadrupoles currents are coarsely set to values that correspond to the smallest beam size in the sample plane. The triplet currents fine tuning is reached using the PIXE map generated from the Cu signal of the grid and searching for the values that give the best spatial resolution both in the vertical (y) and horizontal (x) directions. This can be done using a profile scan, which enables the statistical examination of the Cu unidimensional distribution in order to obtain the narrowest widths and the sharpest edges possible of the vertical and horizontal grid mesh while adjusting the lenses currents. The vacuum system is set to provide pressure under 10^{-6} $mbar$.

3.2.3 Analysis of Samples

Once the preliminary operations are done, selected samples are placed in the x-y-z sample stage for surface or transversal analysis. In the first case samples are glued to the standard sample holder from the surface not destined to analysis, as shown in Fig. 3.9.

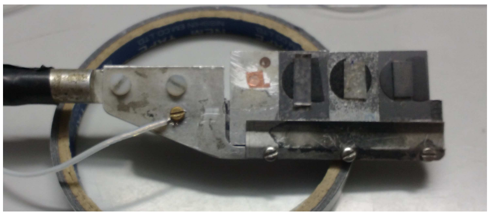

Figure 3.9: Samples glued to the support for the surface analysis. The first sample on the left of the photo is composed by the copper grid and the quartz mirror. The others are plastic samples.

Once inside the chamber, the surface analysis are done placing the sample surface perpendicularly to the beam, as is schematized in Fig. 3.10 a. Whereas, for transversal sections, samples are positioned in the support ensuring that the selected sample edge stuck out few mm from the support, hindering the contribution of the support to the PIXE spectra. A goniometer coupled to the sample stage allows the rotation of the sample to put its transversal section in the sample plan (Fig. 3.10 b). To ensure a sharp definition of the deposit on the sample surface, the stage is rotated a few degrees more than 90°. The procedure adopted to search regions of interest for analysis consists initially of performing large scans, covering approximately 1000 μm^2 of the surface or the cross section length. After, selected regions are inspected by performing smaller scans (from 500 to 50 μm^2) which enable a better spatial precision of the elemental distributions

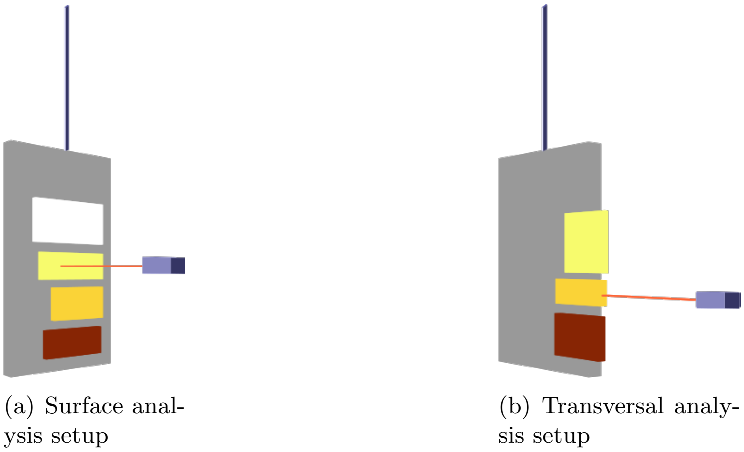

(a) Surface analysis setup

(b) Transversal analysis setup

Figure 3.10: Schematic of the support placements inside the chamber depending if are scheduled surface (a) or transversal (b) analysis.

of the deposit and of the polymer edge and cross section. Point analysis (roughly corresponding to the area of the beam) can then be selected in surface analysis or linescans in case of transversal sections. In Fig. 3.11, the steps of a surface analysis are shown: large maps (212 x 212 μm^2)

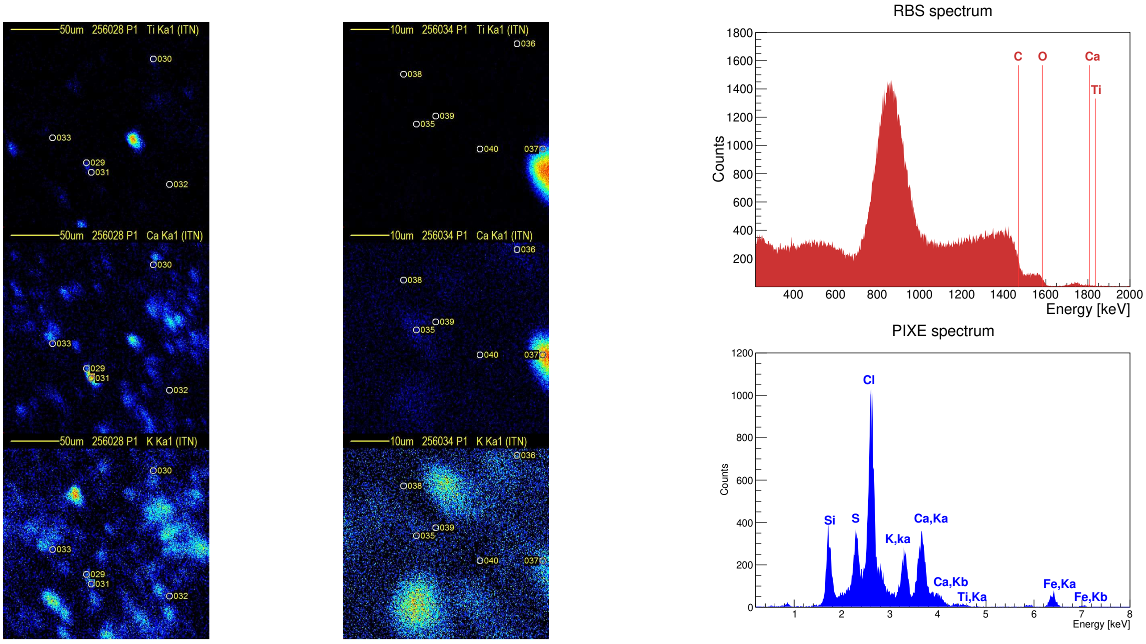

(a) 212 x 212 μm^2 Ti, Ca and K maps of a plastic sample.

(b) 53 x 53 μm^2 Ti, Ca and K maps of a detail.

(c) RBS, on top, and, below, PIXE spectra of the point analysis labelled as 36 in the maps.

Figure 3.11: Surface analysis standard procedure. Firstly a large scan (a) permit to choose the area to analyze. A smaller scan (b) provides maps with an higher resolution of a detail of the large maps. RBS and PIXE spectra (c) of selected points in the maps are then collected.

of spread deposits of Ca, K and Ti, smaller maps (53 x 53 μm^2) of the same elements showing a zoom in the center of the previous maps and RBS and PIXE spectra of the point labelled as 36 of those maps.

In Fig. 3.12 one can find larger maps of Ca, K and Cl of the transversal section of a plastic sample (1060 x 1060 μm^2), maps that zoom a region of those first scans (160 x 160 μm^2) and the PIXE and RBS counts along the line highlighted in the smaller maps, corresponding to the distribution of selected elements. To be noticed that linescans are represented with the counts of the detected PIXE or RBS events relative to each elements and not with their concentration. The relation between counts and concentrations is not straightforward and is given by Eqs. 2.2 and 2.41 (integrated for the whole target thickness), respectively for PIXE and RBS.

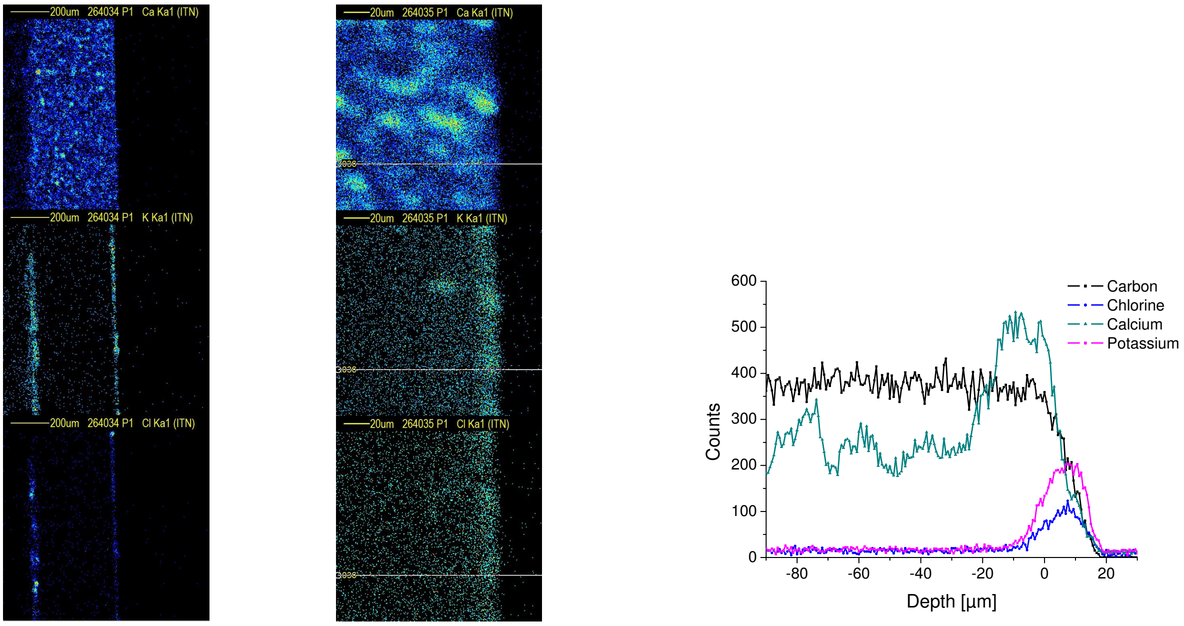

(a) 1060 x 1060 μm^2 maps of Ca, Cl and K of transversal analysis of a sample.

(b) 160 x 160 μm^2 maps of Ca, Cl and K of a detail.

(c) PIXE linescans of C, Ca, Cl and K with deposit in the right edge.

Figure 3.12: Procedure for transversal analysis is similar to the one for surfaces. The large scan (a) is followed by a smaller one (b). An horizontal line can be selected in the maps and RBS and PIXE counts along this line (c) are collected.

3.3 Data analysis softwares

There are several softwares to analyze RBS and PIXE data. For RBS events, in particular, the main dedicated softwares are GISA (Rauhala [68]), RUMP (Doolittle [62]), RBX (Kòtai [69]), DEPTH (Szilàgyi et al. [70]), DataFurnace (NDF) (Barradas et al. [71]) and SIMNRA (Mayer [72]). The main purpose of all these codes is to enable elemental depth profiles to be inferred from particle scattering spectra. The first three codes are "first generation codes", initially designed to do efficient and accurate simulations of single RBS spectra where multiple scattering is not significant. DEPTH is designed as a code for making the best possible calculation of energy straggling effects. NDF and SIMNRA are new generation codes which are designed to handle all cases of interest at the best possible accuracy.
Analysis of PIXE data are also provided by various softwares: Geopixe (Ryan et al. [73]), Gupix [Maxwell et al. [74]], Pixan (Clayton [75]), Pixeklm [Szabò and Borbèly-Kiss [76]], Sapix (Sera and Futatsugawa [77]). The main feature is to provide the best PIXE spectrum fit and estimate the related elements concentration. Differences between these softwares are the employment of different cross-sections database, the different approaches to deal with peak shape and background continuum and the different phenomena taken into account.

The calculation of elemental concentrations is possible using simultaneously PIXE and RBS techniques. At CTN, the available codes that enable to join information between the related spectral data are OMDAQ2007 and NDF. OMDAQ2007 uses the GUPIX algorithm for PIXE analysis while RBS events are analyzed using RUMP routine. NDF, instead, bases its analysis on the simulated annealing algorithm to deal with the *inverse problem* of RBS spectra. A review of the potential of these softwares is reported in the following, along to their limitations in the analysis.

3.3.1 OMDAQ2007

The software code OMDAQ2007 was developed to provide an effective, user-friendly RBS simulation and fitting routine and a convenient interface to GUPIX and RUMP. Charge (Q-factor) and sample matrix are estimated through the RBS spectrum in order to normalize PIXE data and produce quantitative elemental measures, using the approach described in Section 2.3. OMDAQ2007 fitting routine of the RBS spectrum find the best experimental parameters values (spectrum calibration, beam energy, detector resolution) and depth structure of the sample analyzed. Initial conditions have to be set for all the variables. Experimental parameters have standard values. On the contrary, for the sample depth structure, a first guess is required, defining layers number, thicknesses (μm) and elemental compositions (in atomic or weight percentage). During the fitting routine, the software is able to modify layers composition and thickness. The addition of new layers or particular elements in existent layers, if needed, has to be done manually. Once the RBS spectrum best fit is found, OMDAQ2007 automatically calculates the Q-factor and transfers all the parameters (matrix and charge correction) of the fit to the PIXE spectrum analysis routine. Concentrations in ppm (or in % that is $ppm \cdot 10^4$) are then traced for selected elements of each layer. However, total multilayer quantitative analysis are not possible if two or more layers share the same element(s). In this case, in order to have an estimation of the concentrations, multilayers structure should be approximated to one single layer. But, the single layer model, not being the real description of the sample structure, does not fit properly the RBS spectrum and thus does not estimate correctly the Q-factor value. Therefore, when the analyzed sample structure is composed by multi layers that share common elements, uncertainties and errors due to OMDAQ2007 analysis limitations have to be taken into account in the concentrations calculation.

3.3.2 IBA DataFurnace (NDF)

The IBA DataFurnace (NDF) is a general purpose program for analysis of IBA data, currently including RBS, EBS, ERDA, NRA and PIXE (Barradas and Jeynes [78]). The aim of NDF is to analyze simultaneously and fit self-consistently and automatically any number of spectra collected from the same sample, taken with any of these techniques in any experimental condition, in order to estimate the sample depth profile (given as elements or molecules, or any combination of those). Experimental parameters can also be fitted (beam energy, calibration parameters, charge). These operations are provided by the *simulated annealing* algorithm, which is a global minimization algorithm, that use combinatorial optimization, on which NDF is based.

Analysis of samples depth profile using, in particular, PIXE and RBS data are exploited by NDF algorithm with the method presented in Section 2.3. RBS spectrum and the area of the peaks of the major elements present in both RBS and PIXE spectrum have to be given as input to NDF. The program calculates the PIXE elemental yields for the layer structure that is currently fitting the RBS spectrum. Matrix composition that best describes the data not only simulates properly the RBS spectrum but also furnishes elemental PIXE yields compatible with the PIXE spectrum obtained experimentally. Fitting methods can be chosen among several options: the "search" option modify the depth profile without changing the number of layers but only their thickness and composition and optimize the experimental parameters (similar to OMDAQ2007 RBS fitting method). With the "ultra-fast", "fast", "normal", "slow" and "ultra-slow" options the NDF algorithm is free to change also the number of layers. The velocity reference stands for the time involved for the fit and thus its accuracy. However, the slower the fit the more accurate have to be the initial conditions in order to have realistic results. NDF usually gives reasonable results and improves the sample structure resulting from OMDAQ2007 analysis. However, analysis of complex samples with NDF are time consuming: accurate limitations have to be set for the sample structure, in terms of maximum depth achievable by every elements and thickness range for the layers; appropriate elements have to be chosen from the PIXE spectrum and included in the fitting routine, avoiding to select more than the necessary (that would increase the variables and thus probably brings to a non-convergent fit) but still enough to be able to fit all the regions of the RBS spectrum. If these limitations cannot be set properly, the fit may converge to a solution without physical sense. For these reasons, NDF is used only to analyze some significant spectra while OMDAQ2007 is used to analyze all the data acquired with the microprobe.

Chapter 4

Experimental results

The analysis of plastic samples are reported in this chapter. First, the results of the quadrupole focusing to optimize image sharpness are discussed in Section 4.1. In the following Section 4.2, a complete characterization of the pristine polymers used is presented. Samples of HDPE, PET and PP not exposed to salty water under natural conditions are analyzed both in surface and transversal modes. Thus, different information are deduced, such as elements distributions in the plastic surface and in depth, their concentrations and the plastics elemental composition. Given these information, the analysis can proceed with the study of samples immersed in water. This encompasses the study of the surface and transversal elemental distributions in selected areas of the polymers, as presented in Section 4.3. Estimation of the elemental concentrations and depth structure of the deposits point analysis are then included in Section 4.4. To achieve these goals OMDAQ2007 and NDF capabilities are explored to combine and compare the results obtained using the different approaches. To be noticed that when referring to the elemental *concentration* it is intended the quantity expressed in % (that correspond to $ppm \cdot 10^4$), given by OMDAQ2007 PIXE analysis. Elemental *composition* is, instead, referred to the quantity measured in atomic percentage *at* %, resulting from the OMDAQ2007 and NDF RBS analysis. Finally, the elemental profiles obtained in transversal analysis of the polymers are also discussed. These represent direct measurements of the depth structure of the deposits and can be compared with the depth results obtained with the software analysis. Furthermore, cross section elemental distributions allow to investigate the diffusion of specific elements in the polymer matrices, as discussed in Section 4.5.

4.1 Spatial resolution

Generally, in imaging systems, the spatial resolution is given by the system response to a well defined edge and it is defined as the distance required by the edge response to rise from 10% to 90%. PIXE and RBS can be referred as imaging techniques, given the possibility to create maps and linescans with related events. The resolution of the CTN microprobe is normally provided analyzing the copper map given by the scan of a 2000 mesh Cu grid with a period of 12.7 μm pitch, corresponding to approximately 7.7 μm hole and 5 μm bar. In Fig. 4.1 is reported a typical copper map of dimension 53 x 53 μm^2 of the used grid, created with Cu PIXE events. Selecting, once at a time, a vertical and a horizontal line in the map, is possible to have the

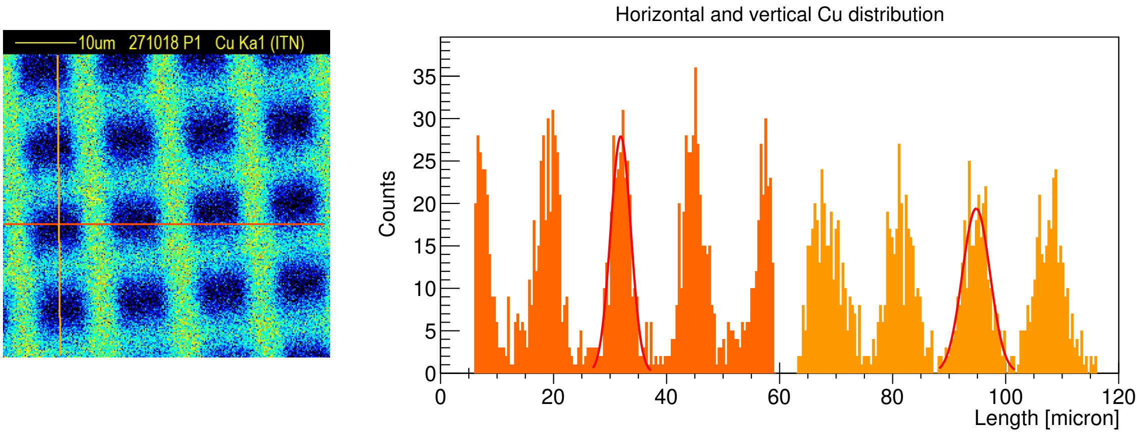

(a) 53x53 μm Cu map.

(b) Horizontal (on the left) and vertical (on the right) linescans.

Figure 4.1: Cu map of the 2000 mesh grid (a) is used, in first approach, to set the optimal quadrupoles currents. Precise value of the spatial resolution are obtained analyzing the linescans (b) along the horizontal (on the left) and the vertical (on the right) directions of the Cu maps.

copper concentration distributions along these two directions. The distribution are considered to be Gaussian. The vertical and the horizontal resolutions of the PIXE system are thus given by the 10% to 90% height distances of the several distributions in both the directions. In Fig. 4.1 b two typical linescans along the horizontal (on the left) and the vertical (on the right) directions of the Cu maps are reported. Gaussian fits of the copper strips distribution in both directions are also visible. Along the horizontal direction, the system presents an higher resolution, as it can also be noticed in the Cu map of Fig. 4.1 a. The resolutions obtained during the several analysis performed in each day in which the microbeam was used are reported in Table 4.1. The best system resolution obtained is 3.3 ± 0.2 μm horizontally and 4.1 ± 0.4 μm vertically.

Day	Horizontal resolution $[\mu m]$	Vertical resolution $[\mu m]$	C Current $[A]$	CO Current $[A]$
1	3.2 ± 0.5	5.6 ± 0.7	42.24	39.59
2	5.2 ± 0.6	6.8 ± 0.9	42.27	39.71
3	4.3 ± 0.3	6.3 ± 0.8	42.19	39.61
4	3.6 ± 0.2	5.5 ± 0.7	42.63	39.77
5	3.3 ± 0.2	4.1 ± 0.4	42.63	39.72

Table 4.1: Horizontal and vertical resolution of the microprobe system during the different days of analysis. The currents of the quadrupoles used to focalize the beam are also reported: *C* refers to the first two quadrupoles while *CO* to the last.

Along with the resolution values, the currents of the quadrupoles used to focalize the beam are also reported. As it can be seen, spatial resolution variations are up to 2 μm while the changes of the optimal working currents of the quadrupoles between different days is of the order of 1%. However, optimal quadrupoles currents depend on many external factor that influence the focalizing system, such as the room temperature and external radiations. Furthermore, resolution depends also on beam current and stability that can influences spectra statistics and resolution. The spatial resolution estimated set a lower limit for the resolution that images created collecting PIXE and RBS events can reach. In addition, it offers an indication of the beam dimension.

4.2 Pristine plastics characterization

Knowledge of the blank plastics features is gained joining information from surface and transversal analysis of the control samples. Plastics matrices composition (in $at\%$), which are fundamental for OMDAQ2007 and NDF analysis of samples with deposit, are estimated, along with the elements distribution inside the plastic, with the two dedicated softwares. This is important to recognize elements that belong to the deposit and to the plastics and to observe ions diffusion or absorption inside the plastics. Furthermore, an estimation of polymers major elements concentration (in %) is done, in order to avoid errors in the concentration estimations of elements present both in the plastic and in the deposit. Finally, all these kind of information about the plastics samples, can also be interesting from a general point of view, being these plastics commonly used and commercialized. This section is organized in three parts, one for each polymer tested and analyzed.

4.2.1 HDPE

Maps of the different elements (Fig. 4.2 a) enlighten that the main component of the plastic matrix is carbon, as expected from the chemical formula of this polymer (CH_2). The C atoms only generate detectable RBS events (Fig. 4.2 b). However, Ca and Ti are also found to be constituents of the plastic matrix, as can be easily seen in the PIXE spectrum collected simultaneously with RBS (Fig. 4.2 c). Looking at the correspondent PIXE Ca and Ti maps, it can be noticed that their distributions is different: Ti is homogeneous inside the plastic while Ca non-homogeneous. The Ca distribution shows a granular-like structure, with agglomerates that reaches a maximum size of 10 μm, evenly distributed within the polymer matrix. The average composition of the plastic has been estimated separately by OMDAQ2007 first and NDF after, setting a standard thickness of 100 μm. OMDAQ2007 estimates:

$$99.15\ at.\%\ \mathrm{C} \quad 0.62\ at.\%\ \mathrm{Ca} \quad 0.24\ at.\%\ \mathrm{Ti}$$

The composition that results from NDF analysis is, instead:

$$97.76\ at.\%\ \mathrm{C} \quad 2.12\ at.\%\ \mathrm{O} \quad 0.10\ at.\%\ \mathrm{Ca} \quad 0.02\ at.\%\ \mathrm{Ti}$$

Since data refer to different large scans of the blank sample, they represent an average of the plastic composition, not considering the differences of polymer regions with or without Ca aggregates. Both softwares give a good fit of the RBS spectrum, with compatible results: major component of this polymer is C with an atomic percentage around 98-99 %. Other elements are present in a very low quantity. In order to use NDF algorithm fitting routine, oxygen is included in the possible matrix elements because RBS spectrum shape suggests its presence: it may be in the matrix in small quantities, as Ca and Ti. Setting a “fast” fit, NDF estimates a low quantity of O in the polymer matrix.

The percentage concentrations of the elements in plastic provided by OMDAQ2007 PIXE analysis, reported on Table 4.2, are also an average of different large scans data. As anticipated by

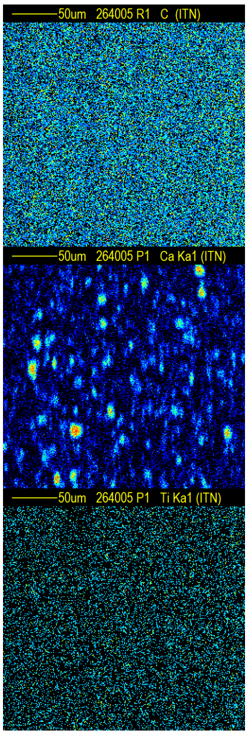

(a) 264 x 264 μm^2 maps of C, Ca and Ti

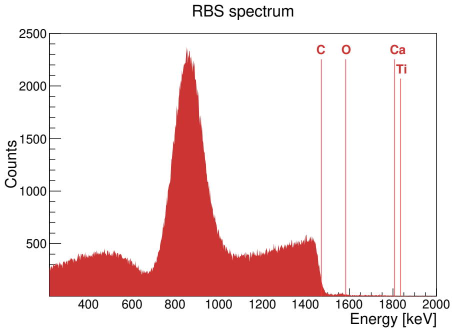

(b) RBS spectrum of HDPE plastic large scan.

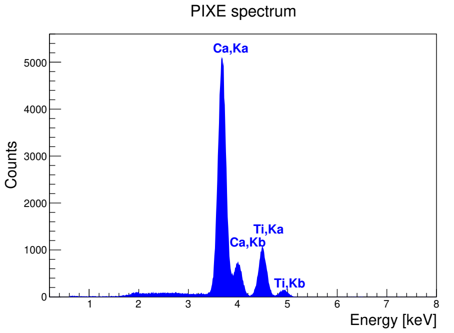

(c) PIXE spectrum of HDPE plastic large scan.

Figure 4.2: 264 x 264 μm^2 maps (a) resulting from a scan of the surface of an HDPE pristine sample. RBS (b) and PIXE (c) spectra define the polymer elemental composition: C is present in the RBS spectrum while Ca and Ti related event are visible in the PIXE spectrum. The charge collected during these analysis is Q = 75 nC.

Element	Concentration [%]
Si	0.047 ± 0.006
Ca	0.4747 ± 0.0009
Ti	0.1486 ± 0.0006
Fe	0.0013 ± 0.0001

Table 4.2: Average elements concentration, provided by the OMDAQ2007 analysis, of the HDPE pristine sample. Values estimated refer to a 100 μm structure with the HDPE composition resulting from the RBS fitting routine of OMDAQ2007.

the PIXE maps, there is a non negligible presence of Ca and Ti inside the plastic. Low traces of other elements, such as Si and Fe, which may be present as contaminants of the polymer, are detected by PIXE analysis. Results from further point analysis in different plastic regions are reported on Table 4.3. Being point analysis, they provide a local description of the sample. They confirm the relatively homogeneous distribution of Ti (its value is almost constant in different points) and set a range in which the Ca concentration can vary, depending if the correspondent point analysis includes or not a Ca dot. Si and Fe are detected also in point analysis with similar concentrations of the scans data analysis. This prove that HDPE is also composed by low quantities of Si and Fe, excluding that related signals in large scans analysis were due to dirtiness on top of the sample.

Point	Si [%]	Ca [%]	Ti [%]	Fe [%]
1_{HDPE}	0.085 ± 0.027	4.226 ± 0.005	0.099 ± 0.001	0.002 ± 0.003
2_{HDPE}	0.042 ± 0.008	0.092 ± 0.001	0.142 ± 0.001	
3_{HDPE}		0.450 ± 0.002	0.191 ± 0.001	0.003 ± 0.001
4_{HDPE}	0.044 ± 0.009	0.146 ± 0.001	0.138 ± 0.001	0.001 ± 0.002
5_{HDPE}	0.041 ± 0.010	0.271 ± 0.001	0.150 ± 0.001	0.002 ± 0.002
6_{HDPE}	0.050 ± 0.009	0.137 ± 0.001	0.168 ± 0.001	0.001 ± 0.002

Table 4.3: Elemental concentration related to points analysis of the HDPE pristine sample. Values estimated refer to a 100 μm structure with the HDPE composition resulting from the RBS fitting routine of OMDAQ2007.

Transversal analysis of HDPE can be seen in Fig. 4.3. Maps and linescans confirm the plastic composition observed in the surface analysis: C is the main component and has a constant distribution, such as Ti. Ca dots are present also inside this polymer and not only on its surface. The thickness of HDPE samples can be estimated looking at the C, Ca and Ti maps and it is about 450 μm. Further details on the linescans analysis, such as the definition of the zero-depth point, that is the plastic edge, are described in Appendix A.

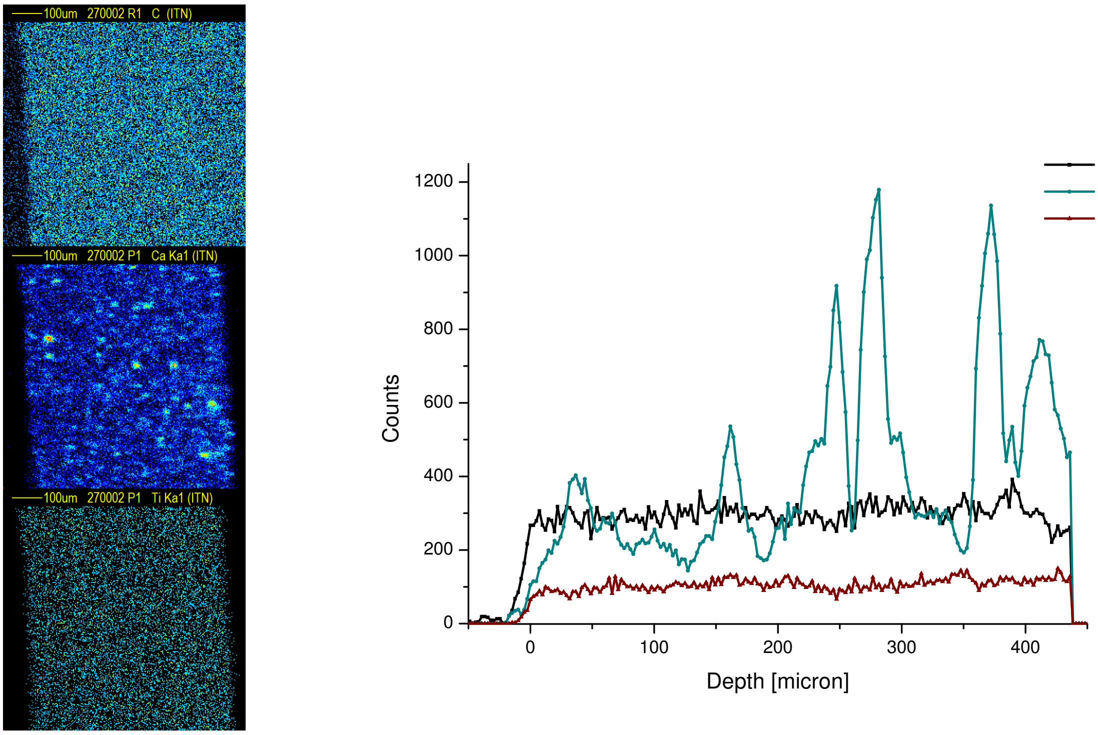

(a) 795 x 795 μm^2 maps of C, Ca and Ti

(b) Distribution of C, Ca and Ti resulting from a linescan

Figure 4.3: 795 x 795 μm^2 maps (a) resulting from a scan of the transversal section of an HDPE pristine sample. Main elements (C, Ca and Ti) distribution (b) provided by a linescan confirm the composition of the polymer deduced from the surface analysis.

4.2.2 PET

From RBS maps (Fig. 4.4 a) of the PET pristine sample, an homogeneous presence of C and O is evinced, confirmed by the RBS spectrum of Fig. 4.4 b and in accordance with the chemical formula of PET polymer, $C_{10}H_8O_4$. The PIXE spectrum (Fig. 4.4 c), since C and O are not detectable by the experimental setup, does not prove the presence of any other elements, except a very low quantity of Ca and I.

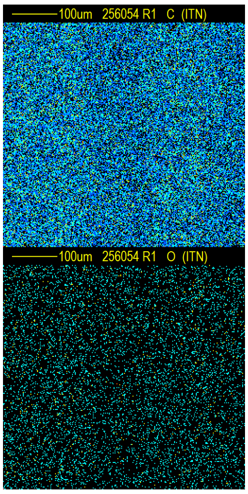

(a) 530 x 530 μm^2 maps of C and O

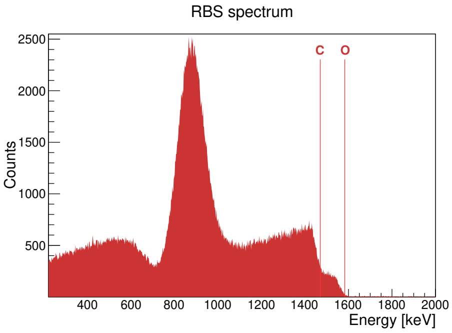

(b) PIXE spectrum of PET plastic large scan.

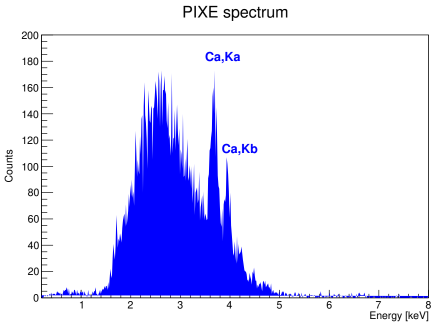

(c) RBS spectrum of PET plastic large scan.

Figure 4.4: 530 x 530 μm^2 maps (a) resulting from a scan of the surface of an PET pristine sample. RBS (b) and PIXE (c) spectra define the polymer elemental composition: C and O presence can be deduced from the RBS spectrum while the PIXEs shows low quantity of Ca and I (Q = 126 nC).

Data refer to different large scans of the pristine sample, thus represent an average of the plastic composition. OMDAQ2007 and NDF simulates the RBS spectrum with different plastic composition, despite having both a good χ^2. OMDAQ2007 result of the RBS fit is consistent with the PET stoichiometry (if the H contribution in the chemical formula is not considered, since hydrogen is not detected):

$$65.84\ at.\%\ \mathrm{C} \quad 33.91\ at.\%\ \mathrm{O} \quad 0.25\ at.\%\ \mathrm{Ca}$$

NDF estimates a composition with an higher quantity of C:

$$76.19\ at.\%\ \mathrm{C} \quad 23.81\ at.\%\ \mathrm{O} \quad 0.001\ at.\%\ \mathrm{Ca}$$

OMDAQ2007 PIXE analysis estimates a low average concentration of Ca (0.0057 ± 0.0003 %) and I (0.0092 ± 0.0008 %) inside the plastic. Point analysis (Table 4.4) again confirm that these elements are not detected in the large scan analysis because dirtyness on the surface, but they

Point	Ca [%]	I [%]
1_{PET}	0.0076 ± 0.0003	0.013 ± 0.001
2_{PET}	0.0074 ± 0.0004	0.012 ± 0.001

Table 4.4: Elemental concentration related to points analysis of the PET pristine sample. Values estimated refer to a 100 μm structure with the PET composition resulting from the RBS fitting routine of OMDAQ2007.

are included in the plastic matrix structure.

Transversal analysis of PET can be seen in Fig. 4.5. C and O homogeneous distributions inside the plastics are deduced from linescans and transversal maps of these elements. No signals from other elements is detected. The estimated polymer thickness of ∼ 350 μm is obtained from the C and O scan maps covering the whole length of the cross section.

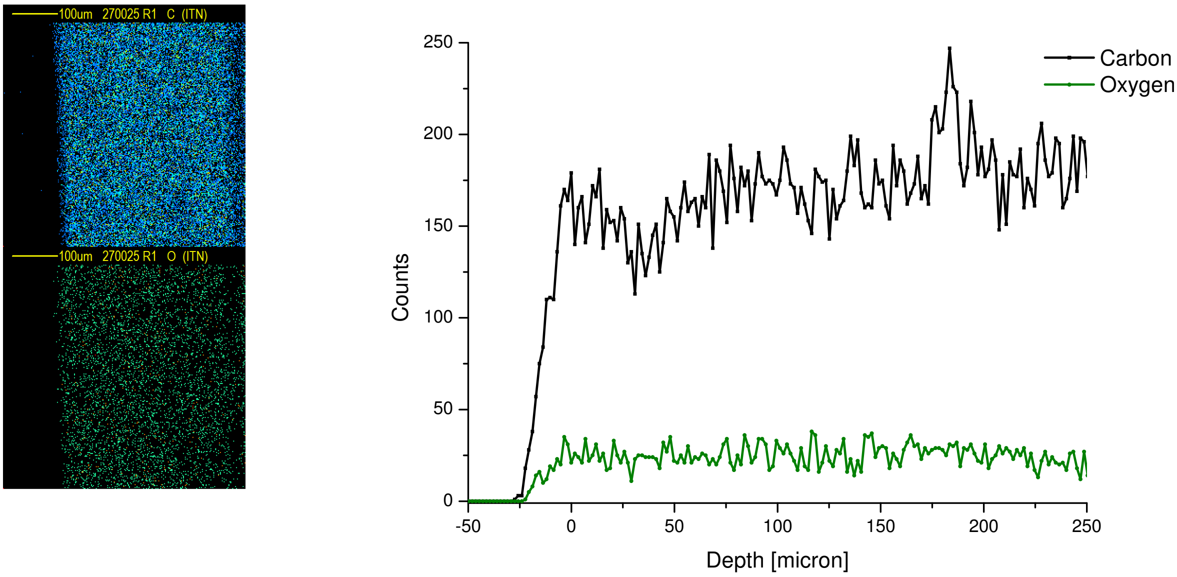

(a) 530 x 530 μm^2 maps of C, Ca and Ti

(b) Distribution of C, Ca and Ti resulting from a linescan

Figure 4.5: 530 x 530 μm^2 maps (a) resulting from a scan of the transversal section of a PET pristine sample. Main elements (C, and O) distribution (b) provided by a linescan confirm the composition of the polymer deduced from the surface analysis.

4.2.3 PP

In Fig. 4.6 a, C and O RBS maps of a PP surface scan are shown, together with the RBS (Fig. 4.6 b) and PIXE spectra (Fig. 4.6 c).

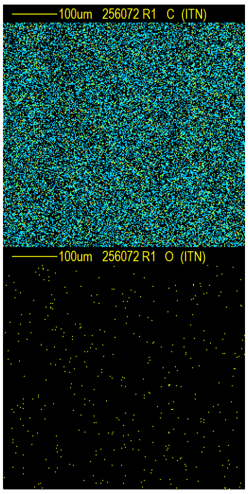

(a) 530 x 530 μm^2 maps of C and O

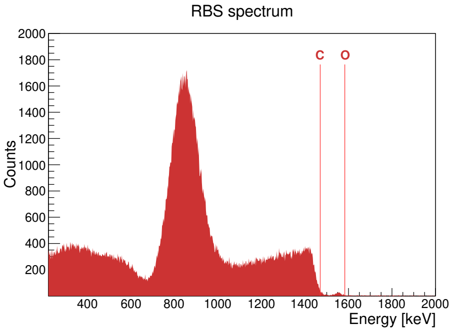

(b) RBS spectrum of PP plastic large scan.

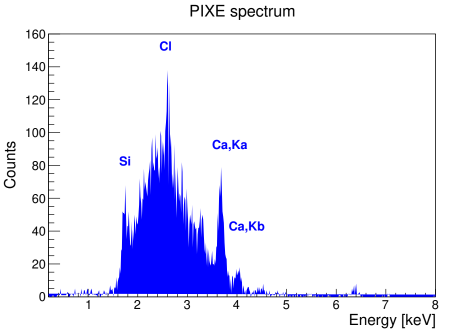

(c) PIXE spectrum of PP plastic large scan.

Figure 4.6: 530 x 530 μm^2 maps (a) resulting from a scan of the surface of a PP pristine sample. RBS (b) and PIXE (c) spectra define the polymer elemental composition: C is the main element that compose the plastic (RBS) while other elements, such as Si, Cl and Ca are traced in low concentrations (PIXE). Oxygen presence is not evident.

This polymer is mainly composed by C, as it is stated also by its chemical formula, $(C_3H_6)_n$, that has an homogeneous distribution inside the PP matrix. From PIXE spectrum, is possible to notice the presence of traces of Si, Cl and Ca while from the RBS spectrum O seems to be present in the polymer. Since Si is the element that in PIXE spectrum has the larger peak area, it has been included in the matrix composition first guess of the analysis softwares and it is present in the fit results, even if in a very low atomic percentage. Similar plastic compositions are provided by OMDAQ2007:

$$97.85\ at.\%\ \text{C} \quad 1.76\ at.\%\ \text{O} \quad 0.39\ at.\%\ \text{Si}$$

and NDF:

$$98.55\ at.\%\ \text{C} \quad 1.37\ at.\%\ \text{O} \quad 0.08\ at.\%\ \text{Si}$$

Lastly, OMDAQ2007 PIXE analysis of large scans data provide the quantification of the Si, Cl and Ca concentration inside the plastic (Table 4.5). The results of point analysis of the same samples are reported on Table 4.6. The local elemental concentrations are similar to the ones obtained in large scan analysis, proving that these elements are inside the plastic with very low

Element	Concentration [%]
Si	0.08 ± 0.01
Cl	0.0039 ± 0.0007
Ca	0.0040 ± 0.0003

Table 4.5: Average elements concentration provided by the OMDAQ2007 analysis that combine PIXE and RBS through the Q-factor. Values estimated refer to a 100 μm structure with the PP composition resulting from the RBS fitting routine of OMDAQ2007.

Point	Si [%]	Cl [%]	Ca [%]
1_{PP}	0.06 ± 0.01	0.004 ± 0.001	0.0034 ± 0.0004
2_{PP}	0.12 ± 0.02	0.005 ± 0.001	0.0049 ± 0.0004

Table 4.6: Elemental concentration related to points analysis of the PP pristine sample. Values estimated refer to a 100 μm structure with the PP composition resulting from the RBS fitting routine of OMDAQ2007.

concentrations.
Samples of this plastic are too thin to be analyzed directly in the transversal section. Problems have been found in recognizing the selected regions for analysis of the samples inside the chamber and in the correct beam placement.

To sum up, the pristine plastics analysis define the elemental composition for each polymer of the substrate layer that will be included in the OMDAQ2007 and NDF algorithm when exposed samples are analyzed. During the following fitting routine, the composition of the substrate is set to be fixed, relying on the estimation that results from these analysis of the blank samples. In addition, the imaging capabilities of PIXE and RBS determine the elements distribution both on the surface, using the surface analysis, and in the plastic interior, using the cross-sections data. Analyzing exposed samples, these information help to discriminate if a particular element is included in the deposit materials and, even more, if it diffused in the plastic matrix, or if it is characteristic of the considered polymer. Finally, the estimation of the concentrations of the elements detected in the PIXE spectrum show traces of minor elements in the plastic matrix, that may be included during the production process, up to 0.004%.

4.3 Deposit general distribution and morphology features

Comparing different elemental maps of same scans, it is possible to infer the nature of the deposits and the mechanisms of adhesion of these deposits on the plastics surface.

In all the different polymers samples, the deposition mosaic consists of abiotic and biotic components. Biota can be identified through the Ca map, as calcium carbonate ($CaCO_3$) is the building block for the cell walls, shells and skeletons of many marine organisms (Hofmann and Bischof [79]). An example of biological deposit found during a surface scan can be seen in Fig. 4.7. Phosphorous and sulfur also characterize this type of deposits, as they follow the Ca distribution. Anyhow, in biotic materials their concentrations is not comparable to calcium. Silt, clay, sand particles, salt grains and earth crust materials are denoted as sedimentary deposit. Associated elements are: silicon, given that sand chemical formula is SiO_2 and Si is the major component of earth crust, potassium, present in many minerals and saline compounds (for example KCl), chlorine, mainly due to salt particles ($NaCl$), calcium and heavier metals like titanium and iron (Wedepohl [80], Babel and Schreiber [81]). In Fig. 4.7, sedimentary deposit is also visible looking at the maps. It is characterized by a variety of different sized grains and also by spread materials, as anticipated by the microscope observations. Si, S, K and Fe seem to have correlated distributions. Calcium, besides marine organisms, can be characteristic also of mineral particles ($CaSO_4$ but also $CaCO_3$ itself, for example). Chlorine particles distribution is not correlated with any of the other elements and it is characterized by clusters that can vary in a wide size range (from few μm up to ~ 100 μm), most probably representing sea salt deposits, which are present throughout the plastic surface. Also titanium, despite being present in lower quantities, is mainly characterized by small agglomerates.

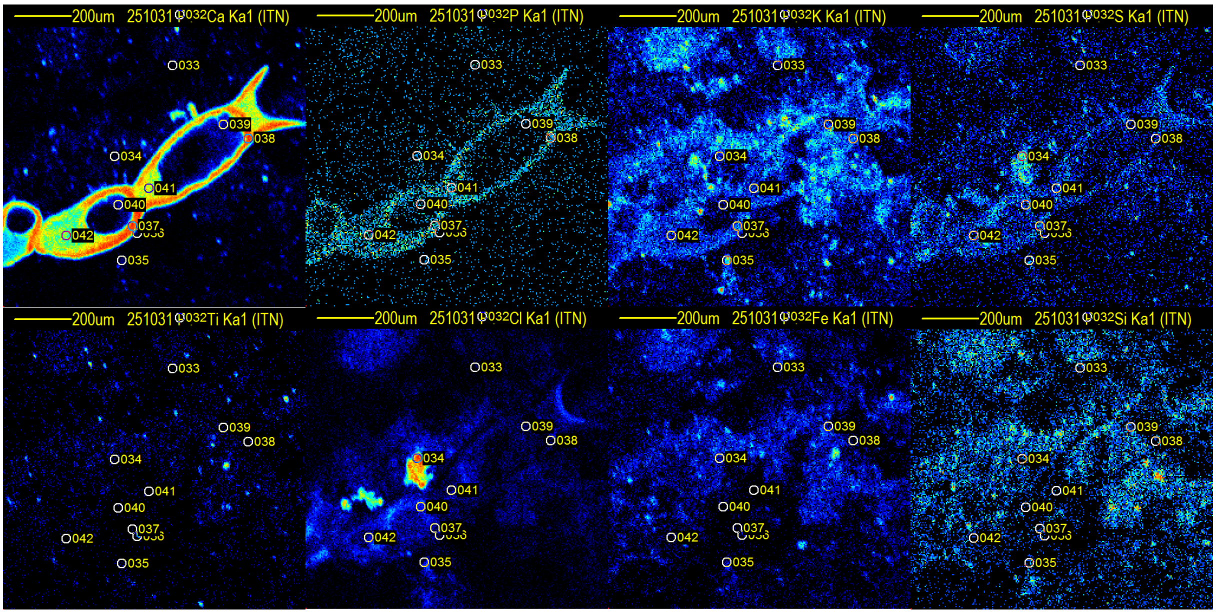

Figure 4.7: 1060 x 1060 μm^2 maps of Ca, P, K, S, Ti, Cl, Fe and Si that refer to a surface scan of a PET sample exposed to water. Biologic deposit has been found in the region of these maps, as it can be noticed from the Ca distribution. Materials of other nature is intertwined with the biota.

Comparing the maps of the different elements reported in Fig. 4.7, it can be noticed that deposits of different nature are often present in the same area of the sample. Evidences of this features can be also seen in the maps of Fig. 4.8. Biological and sedimentary deposits are distributed with different patterns even though they are concentrated in the same plastic region. It can be concluded that materials tend to stick in plastic surfaces in multilayers structures that can contain different types of molecules intertwined with each other.

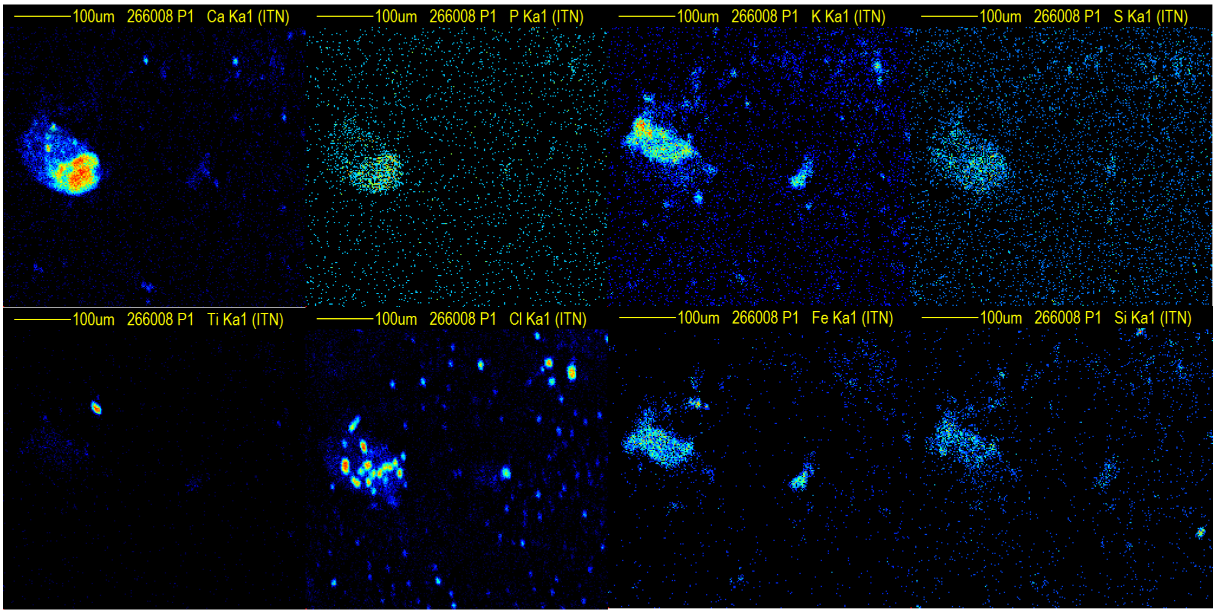

Figure 4.8: 530 x 530 μm^2 maps of Ca, P, K, S, Ti, Cl, Fe and Si that refer to a surface scan of a PET sample exposed to water. Mixed deposit has been found in an area of the region of these maps: Ca distribution correspond possibly to biologic deposit; in the same area, K, Fe and Si distributions are related to sediment particles. Furthermore, Cl is distributed, in the same region of the sample, in small aggregates (salt particles).

Last observation that can be done looking at elemental maps is that different amount of deposit materials can be found in different regions of the samples, always with the same discussed patterns. Moreover, not all the samples surface are covered by deposit, some area seems to be without any attached materials. Fig. 4.9, as well as Fig. 4.7, shows an high loaded deposit region, composed by different kind of deposits mixed together. Cl deposits are grouped in common regions, while other elements materials are spread all over the scanned surface, with a variety of different μm size grains. Maps of a region with low quantity of materials are reported in Fig. 4.10. A thin layer of mixed elements material covers some of the plastic area, while the remaining area does not show the presence of any other detectable element. The region in Fig. 4.8 also shows a mosaic distribution as the one just described, where deposit regions are surrounded by areas practically devoid of deposit.

In conclusion, samples are characterized by high and low deposit regions. In loaded regions, deposits of different nature are overimposed and mixed one to the others, making a non trivial multi-layered structure. In addition to this, particles of different materials can be composed by common detected elements, since they represent the main sea-water and earth crust constituents and can be found in different minerals (Babel and Schreiber [81]). Therefore, to estimate the elemental concentrations in the variety of deposits found in the polymers, the complexity of the deposit attached on the plastics surface has to be taken into account.

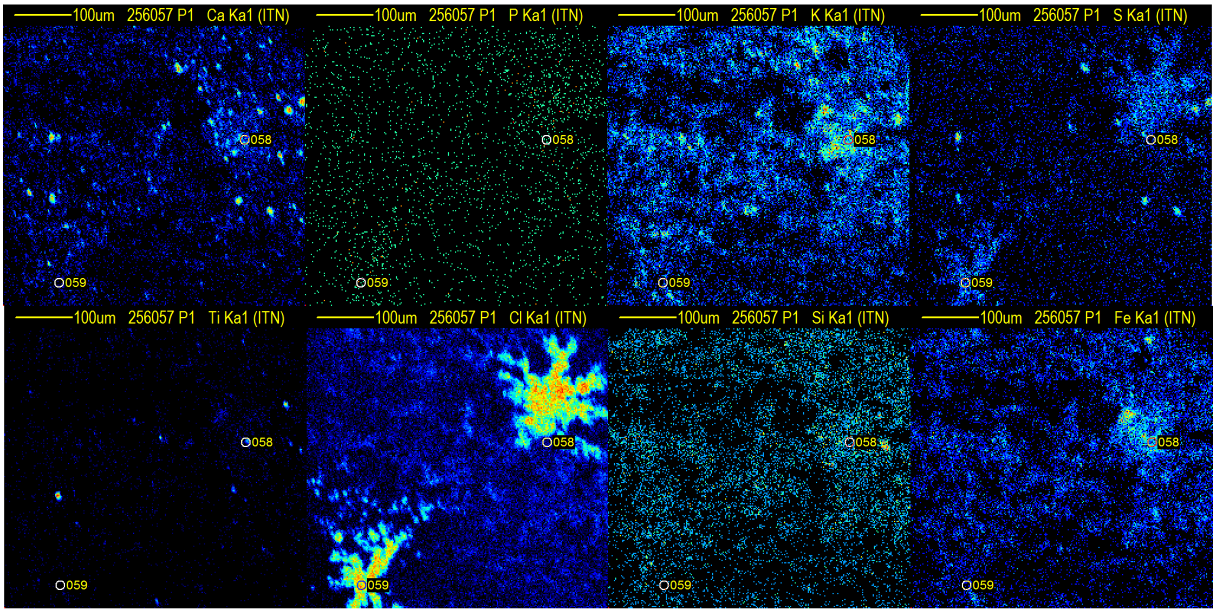

Figure 4.9: 530 x 530 μm^2 maps of Ca, P, K, S, Ti, Cl, Fe and Si that refer to a surface scan of a PP sample exposed to water. High-loaded region of deposit has been found in these maps: clusters of chlorine are dominating the deposit in this area. Other elements are present widely in lower quantities and with different distributions.

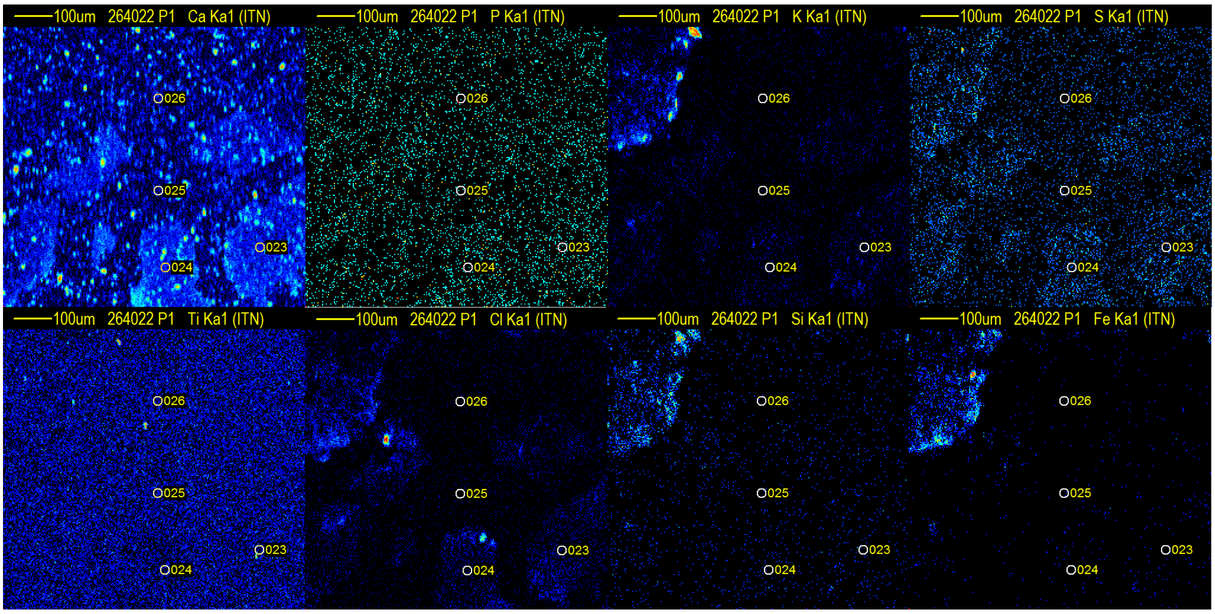

Figure 4.10: 530 x 530 μm^2 maps of Ca, P, K, S, Ti, Cl, Fe and Si that refer to a surface scan of a HDPE sample exposed to water. Low-loaded region of deposit has been found in these maps: plastic surface is covered, only in some regions, by a thin layer of mixed elements material. The remaining area does not show the presence of any other detectable element.

Since equal considerations can be done for samples of every polymers, the following analysis does not consider if the sample substrate is HDPE, PET or PP, besides to make general considerations about elements that are shared between deposits and polymers. Even more, samples exposed either for 7 and 30 days show the same elemental distribution patterns, with the only exception that the plastic surface is characterized by an higher percentage of low-loaded regions respect plastics exposed for longer. This aspect does not influence the concentration and depth structure analysis, since, locally, the deposit has the same features. Therefore, from now on, also specimens with different exposition time are treated equally, with the exception of the investigation of elements adsorption inside the plastic matrix, in which the exposition time may represents a significative variable of the phenomenon.

4.4 Quantitative concentration and depth deposit characterization

To characterize the elemental composition of deposits, the complementarity of PIXE and RBS is explored. Different elements are detected from these two techniques and different are also the deducible information: backscattering events give hints mainly about the stoichiometry and the depth structure of the sample analyzed, while PIXE data reflect its elemental concentration. Nevertheless, better precision on the results is achieved if spectra of both techniques are combined during the samples analysis. Improvements of the PIXE analysis relying on the RBS data (Q-factor, OMDAQ2007) permit to estimate the concentrations of the elements correcting the systematic error represented by the charge measurement and considering an estimated depth composition of the analyzed sample. On the other way, investigation of the depth profile based on the RBS data are facilitate if the PIXE spectrum is also taken into account (NDF), since elemental concentrations inferred by collected X-rays set some limitations in the fitting routine of the RBS spectrum that estimates the depth profile (See Section 2.3).

The microprobe setup gives the possibility to cluster PIXE and RBS for the analysis of the plastic samples. The characterization of the deposit in their surface is done using data of point analysis that have been chosen during the data acquisition operations, trying to include deposits of different nature. The rationale of the following analysis of data related to these surface analysis, either if OMDAQ2007 or NDF is considered, consists in defining an initial depth structure of the sample with three layers:

1. Sample coating; thin layer ($< 0.5\ \mu m$) with 100 $at.\%$ C composition.
2. Deposit (if present); variable thickness and composition.
3. Plastic baking; standard thickness (100 μm that represents an infinite thickness for the specific beam energy and projectile used) and composition depending on the particular sample polymer, estimated during the pristine plastics analysis.

OMDAQ2007, which is used to analyze all the data collected, estimates the elements concentration in the deposit layer, optimizing previously the compositions and thicknesses of the three layers structure model during the RBS spectrum fitting routine, but without evaluating a more complex, multi-layered structure. Therefore, the multilayer characteristics of deposits, discussed in Section 4.3, is not completely assessed using this software. This represents a limitation to analyze the elemental concentrations in the plastic deposit that is characterized by a complex structures, with layers that also share common elements. As already stated, cells (several layers: cell wall - intracellular medium-cell wall) sometimes are on top or below sea salt and sediment particles (Fig. 4.7) and sediment deposits consist of clusters or aggregates of overlapping particles with different composition (Fig. 4.9). For these reasons, the uncertainty in the determination of the deposit matrix composition is even larger, as well as in the charge estimation. Consequently the elemental concentrations obtained using PIXE data, which rely on the matrix composition and charge estimated from RBS analysis, are affected by these uncertainties.

NDF provides a more powerful approach as it allows the estimation of the best multilayer depth structure using the RBS spectra and experimental PIXE yields. In this way, the sample depth profile solutions obtained with NDF combining RBS and PIXE data are self-consistent with the information provided by the two techniques. However, unlike OMDAQ2007, the elemental concentrations in *ppm* from PIXE data are not estimated.

Depth structure results of these softwares are compared with direct measurements provided by linescans of samples cross section. Surface deposits thickness is estimated analyzing the elements distributions. General consideration about the interaction of the material with the polymer can also be done.

In this Section, joining information from the two analysis softwares and transversal sections data, is achieved a characterization of deposits of different nature: sediment deposits, including either individual particles and clusters of abiotic materials and regions with biologic material.

4.4.1 Sediment deposit

The analysis of sediment deposits on different polymer samples show similar elemental correlations in few cases. These elemental associations enable to identify the main minerals, compounds and ionic species present in sediments and sea water. Therefore, examples of the analytical results obtained in the analysis of deposits with similar features are presented below.

Calcium sulphate particles

Example of deposit with recurrent patterns are the particles with the elemental profile showed in the maps of Fig. 4.11. These particular deposits are characterized by an high concentration of Ca and S, while other elements are in different regions of the maps. The area analyzed with the point analysis are marked and numbered in those maps. Points number 49_{CaS} and 50_{CaS}, in particular, have been chosen in order to hit completely the particles rich in S and Ca. The other point analysis are related to other maps: numbers 44_{CaS} and 45_{CaS} cover the same particles as points 49_{CaS} and 50_{CaS} but are selected in larger scan maps. Numbers 61_{CaS} and 62_{CaS} correspond to similar particles in a PP sample. Fig. 4.12 illustrates the RBS spectra

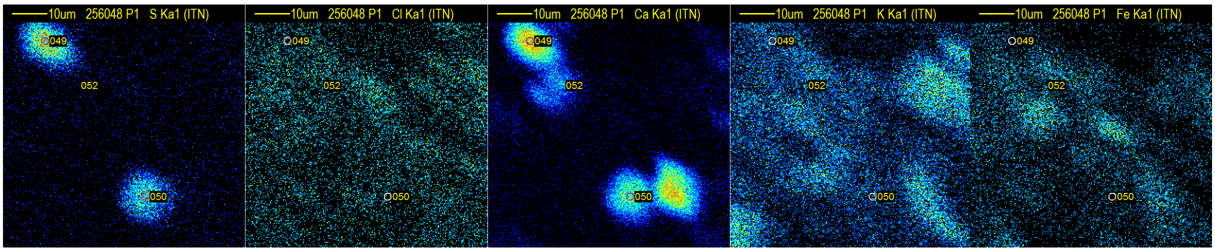

Figure 4.11: 53 x 53 μm^2 maps of S, Cl, Ca, K and Fe that refer to a surface scan of a PET sample exposed to water. Particles with an high concentration of Ca and S can be found in these maps.

corresponding to the points 49_{CaS} and 61_{CaS}. Deposit composition that best simulate the RBS spectra using OMDAQ2007 of all the considered points are reported on Table 4.7.

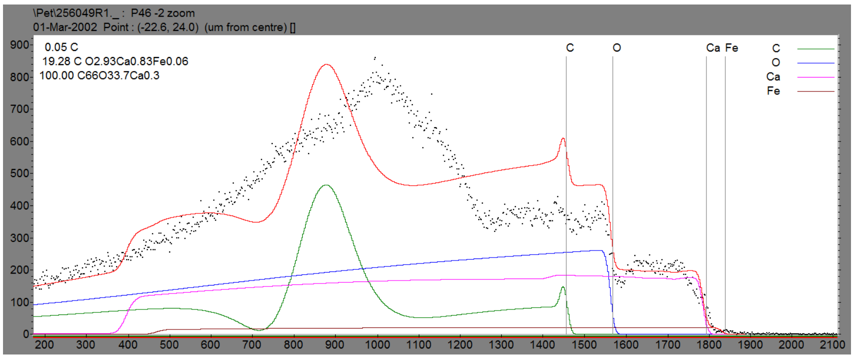

(a) Spectrum of point 49_{CaS} (Q = 117 nC, $\chi^2 = 5.2$)

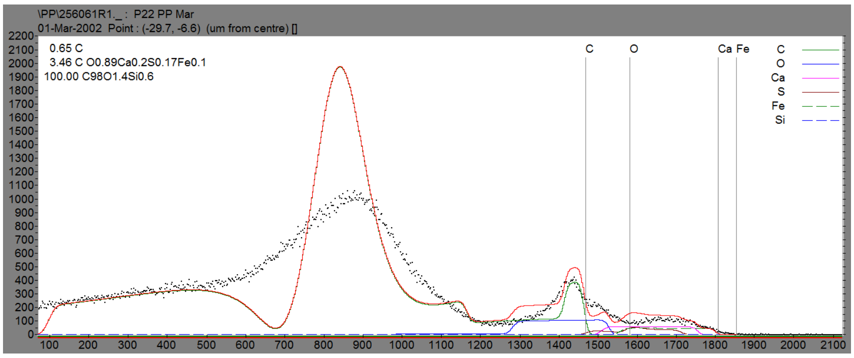

(b) Spectrum of point 61_{CaS} (Q = 50 nC, $\chi^2 = 9.3$)

Figure 4.12: RBS spectra of points 49_{CaS} and 61_{CaS} showing different characteristics, due to the different deposit thickness and composition. The red line in the graph is the spectrum simulated from the best composition fit given by OMDAQ2007. The coloured lines are the yields of the individual element that compose the matrix.

Point	Thickness [μm]	C [$at.\%$]	O [$at.\%$]	S [$at.\%$]	Ca [$at.\%$]	Fe [$at.\%$]
61_{CaS} (PP)	3.5	42.4	37.7	7.2	8.5	4.2
62_{CaS} (PP)	3.9	43.0	41.2	7.3	4.5	3.9
44_{CaS} (PET)	16.5	44.1	44.5	3.5	6.9	1.0
45_{CaS} (PET)	16.0	45.2	51.1	1.4	0.5	1.8
49_{CaS} (PET)	19.3	19.4	56.9	12.8	9.7	1.2
50_{CaS} (PET)	15.6	41.5	40.2	8.3	9.1	0.8

Table 4.7: Structure parameters that best fit the RBS spectrum for every analyzed point: thickness of the deposit layer and atomic composition. First layer, that is the C coating, and plastic baking layer, with fixed composition depending on the plastic, are not reported.

Deposit analyzed in runs 61_{CaS} and 62_{CaS} are about 3/4 μm while the ones analyzed in the other runs are about 15/20 μm. Estimated thickness of point analysis data taken in the same particle are comparable. This is the case of the data points 44_{CaS}, 45_{CaS} and 49_{CaS}, 50_{CaS}. The differences in the particles thickness of different samples is also predictable looking at the RBS spectra of Fig. 4.12. The spectrum of point 49_{CaS} has well defined barriers corresponding to Ca and O while point 61_{CaS} spectrum does not. This means that, in the first case, atoms of Ca and O are included in the deposit depth structure for several μm and thus induce the backscattering of the protons at different energies. Even if the deposit thickness is different, the deposit monolayer compositions resulting from the fit of the RBS spectra are similar, with an high presence of O, Ca and S and of C for the substrate. Fe is included probably for other type of deposit on the same area. χ^2 of the RBS spectra fits are variable. Fit of point 49_{CaS} is the best obtained for this type of deposit while the one of point 61_{CaS} is the worst, as it can be noticed from the values reported in Fig. 4.12. However, even if the χ^2 of point 49_{CaS} states the goodness of the related fit, not all the region of the RBS spectrum are simulate properly, with a particular regard the C resonance. Multilayer matrix probably would improve the fit goodness. On the other hand, since elements are probably shared between the different layers that compose deposits, setting a multilayers structure would not allow to have correct concentration estimations, that is the principal aim of OMDAQ2007 analysis. The PIXE spectra correspondent to the points 49_{CaS} and 61_{CaS} are reported on Fig. 4.13, while results of the PIXE analysis can be seen on Table 4.8.

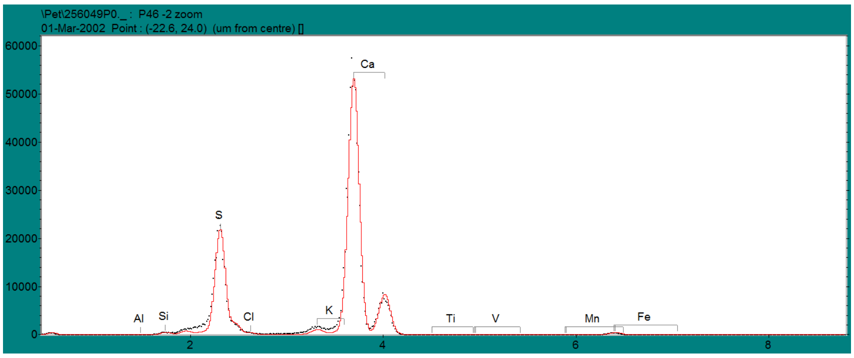

(a) Spectrum of point 49_{CaS} (Q = 117 nC)

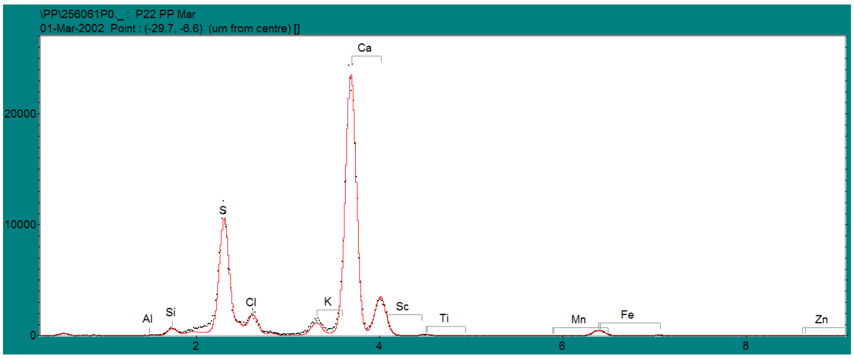

(b) Spectrum of point 61_{CaS} (Q = 50 nC)

Figure 4.13: PIXE spectrum of point 49_{CaS} and 61_{CaS}. Energy reported in keV. The dominance of Ca and S atoms is evident from the line in the spectra corresponding to their characteristic energy. The red line in the graph is the fit of the spectrum used by OMDAQ2007 to estimate the elements concentrations.

The high presence of S and Ca is confirmed, while other elements, such as Cl, K and Fe are present with lower percentages. Given these results, it can be proposed that those deposit clusters are calcium sulphate ($CaSO_4$). To support this suggestion, considerations can be done looking at the values of the structure compositions, resulting from the RBS fit, and of the elements

Point	S [%]	Cl [%]	K [%]	Ca [%]	Fe [%]
61_{CaS} (PP)	8.99 ± 0.03	1.12 ± 0.01	0.462 ± 0.007	10.24 ± 0.02	0.74 ± 0.01
62_{CaS} (PP)	9.02 ± 0.03	1.44 ± 0.01	0.550 ± 0.008	11.12 ± 0.02	0.81 ± 0.01
44_{CaS} (PET)	2.85 ± 0.01	0.042 ± 0.002	0.076 ± 0.002	2.480 ± 0.005	0.149 ± 0.002
45_{CaS} (PET)	1.59 ± 0.01	0.030 ± 0.001	0.046 ± 0.001	1.499 ± 0.004	0.093 ± 0.002
49_{CaS} (PET)	5.02 ± 0.01	0.045 ± 0.002	0.065 ± 0.002	4.251 ± 0.006	0.134 ± 0.002
50_{CaS} (PET)	2.71 ± 0.01	0.049 ± 0.002	0.083 ± 0.002	2.541 ± 0.005	0.170 ± 0.002

Table 4.8: Concentrations of the main elements (S, Cl, K, Ca and Fe) estimated for each analyzed point considering the deposit layer composition and the q-factor resulting from the RBS fitting routine.

concentrations estimated with the PIXE analysis. In fact, this particular deposit should respect the chemical formula of the calcium sulphate. This implies the proportion (Ca:S:O = 1:1:4) for the Ca, S and O atomic percentages. Additionally, elements concentrations should have defined ratios, calculated looking at the chemical formula and the elements atomic masses. In the $CaSO_4$ case, since oxygen atoms do not participate at the PIXE events, only the S/Ca concentrations ratio can be considered. Theoretical value of this ratio corresponding to calcium sulphate is 0.8. In table 4.9 the calculated ratios are reported.

Point	Composition (RBS) ratio			Concentration (PIXE) ratio
	Ca/S	O/Ca	O/S	S/Ca
61_{CaS} (PP)	1.2	4.5	5.2	0.88 ± 0.004
62_{CaS} (PP)	0.6	9.1	5.6	0.81 ± 0.003
44_{CaS} (PET)	2.0	6.4	12.6	1.15 ± 0.005
45_{CaS} (PET)	0.3	113.0	37.7	1.06 ± 0.005
49_{CaS} (PET)	0.8	5.9	4.4	1.18 ± 0.004
50_{CaS} (PET)	1.1	4.4	4.9	1.07 ± 0.004

Table 4.9: Ratios between the *at.%* of Ca, S and O estimated during the RBS fitting routine and ratio of the S and Ca concentrations estimated with PIXE analysis.

Atomic percentages ratios are coherent with elements proportions (Ca:S:O = 1:1:4) only in few cases. This is due to the difficulties to fit the RBS spectra with the monolayer structure. Furthermore, the kinematic factors of the elements detected in the RBS spectra have similar values, that represents a source of ambiguity when RBS events have to be correlated to a specific element. Concentration ratios, on the other hand, are very close to the theoretical value (0.8) and are comparable if related to analysis on the same map (61_{CaS} with 62_{CaS} and 44_{CaS}, 45_{CaS}, 49_{CaS}, 50_{CaS} between them). In conclusion, deposits agglomerates on exposed samples that present high concentration of S and Ca are most probably made of calcium sulphate.

Chlorine salt particles

Cl particles are widely distributed in all samples analysed. Typical chlorine deposit is illustrated in the maps of Fig. 4.14.

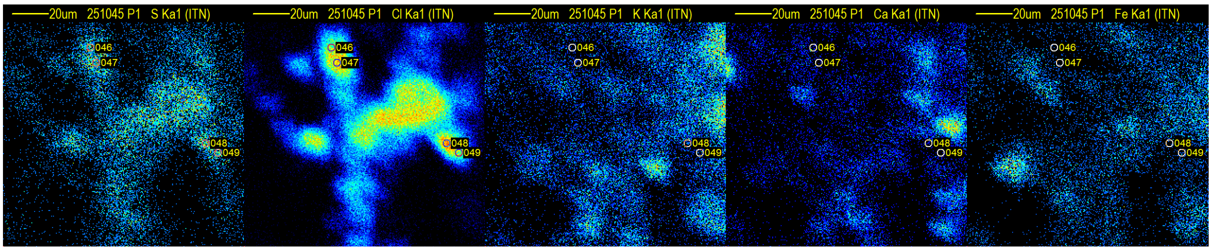

Figure 4.14: 106 x 106 μm^2 maps of S, Cl, K, Ca and Fe that refer to a surface scan of a PET sample exposed to water. Chlorine is found to be concentrated in some region of samples with a distribution independent from the ones of other elements.

Analyzed points are highlighted in those maps. Point analysis data number 34_{Cl} of Fig. 4.7 and 59_{Cl} of Fig. 4.9 are also included in this deposit type. In Table 4.10, monolayer compositions of that points estimated by OMDAQ2007 fitting routine are shown. Example of RBS spectra can be seen in Fig. 4.15, related to data of points 59_{Cl} and 49_{Cl}.

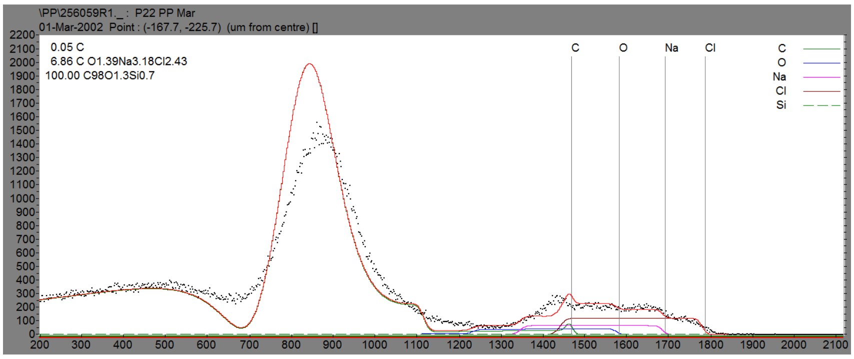

(a) Spectrum of point 59_{Cl} (Q = 105 nC, χ^2 = 5.5)

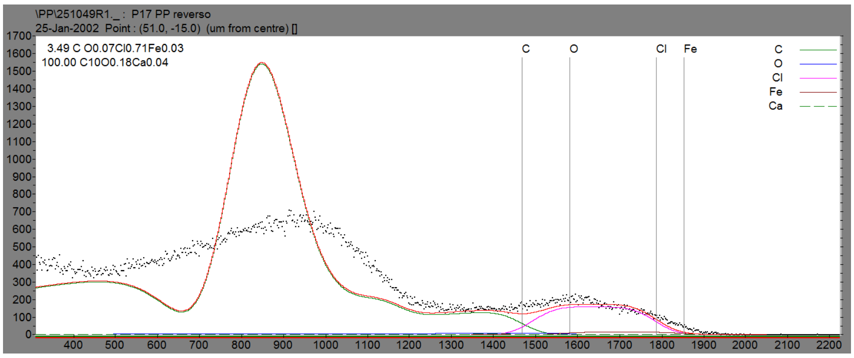

(b) Spectrum of point 49_{Cl} (Q = 112 nC, χ^2 = 10.6)

Figure 4.15: RBS spectrum of point 59_{Cl} and 49_{Cl}. The edge of the spectrum correspond at to backscattering events with Cl atoms in the sample surface. The resolution of the spectrum of the point 59_{Cl} is higher, due maybe to differences in particular experimental conditions in the analysis days. The red line in the graph is the spectrum simulated from the best composition fit given by OMDAQ2007. The coloured lines are the yields of the individual element that compose the matrix.

Point	Thickness [μm]	C [$at.\%$]	O [$at.\%$]	Na [$at.\%$]	Cl [$at.\%$]
34_{Cl} (PET)	17.7		48.5	38.2	13.4
46_{Cl} (PP)	4.5	28.6	29.7		41.7
47_{Cl} (PP)	4.9	39.5	20.2		40.3
48_{Cl} (PP)	4.6	36.8	27.8		35.4
49_{Cl} (PP)	3.5	55.3	4.0		39.1
59_{Cl} (PP)	6.9	12.5	17.3	39.8	30.4

Table 4.10: Structure parameters that best fit the RBS spectrum for every analyzed point: thickness of the deposit layer and atomic composition. First layer, that is the C coating, and plastic baking layer, with fixed composition depending on the plastic, are not reported.

Cl presence is marked by the correspondent barrier in the spectra. Area analyzed with points 34_{Cl} and 59_{Cl} contain also sodium, according to the OMDAQ2007 estimations. Na is not included in the deposit composition of the other points. However, as it can be noticed observing Fig. 4.15 b, RBS spectra related to those points do not have very well defined barriers or bumps, resulting ambiguous to fit (χ^2 of the fit, in fact, is 10.6). Even so, the estimated thickness from the bad-fitted spectra is compatible, ~ 4 μm, while the depth size of the other deposit area are larger, ~ 7 μm and ~ 18 μm. Finally, proportion between Na and Cl atomic percentages respects the $NaCl$ chemical formula (Na:Cl = 1:1) only for the composition resulting from data of the point 59_{Cl}. This result is also due to the relative goodness of the RBS fit ($\chi^2 = 5.5$).
PIXE spectra are shown in Fig. 4.16 while estimated elements concentration are reported on Table 4.11.

Point	S [%]	Cl [%]	K [%]	Ca [%]	Fe [%]
34_{Cl} (PET)	0.35 ± 0.02	17.91 ± 0.02	0.326 ± 0.002	0.107 ± 0.002	0.307 ± 0.003
46_{Cl} (PP)	0.52 ± 0.02	21.47 ± 0.04	0.217 ± 0.005	0.264 ± 0.005	0.221 ± 0.006
47_{Cl} (PP)	0.48 ± 0.02	26.81 ± 0.03	0.162 ± 0.004	0.117 ± 0.003	0.124 ± 0.004
48_{Cl} (PP)	0.41 ± 0.02	27.81 ± 0.03	0.707 ± 0.006	0.387 ± 0.005	0.686 ± 0.008
49_{Cl} (PP)	0.48 ± 0.03	29.40 ± 0.04	0.836 ± 0.008	0.173 ± 0.005	0.71 ± 0.01
59_{Cl} (PP)	0.55 ± 0.08	21.66 ± 0.03	0.417 ± 0.005	0.253 ± 0.004	1.02 ± 0.01

Table 4.11: Concentrations of the main elements (S, Cl, K, Ca and Fe) estimated for each analyzed point considering the deposit layer composition and the q-factor resulting from the RBS fitting routine.

Besides the different deposit structures estimated for each analysis, the Cl concentrations calculated are around 20% for all different data. Other elements concentrations are negligible compared to chlorine (less than 5% compared to Cl values). Since Na X-rays are not detected, its concentration cannot be estimated using PIXE data. Thus is not possible to have a further proof that these deposits are $NaCl$ salts. Nevertheless, being salty particles one of the main constituent of sea water, it remains the most probable solution.

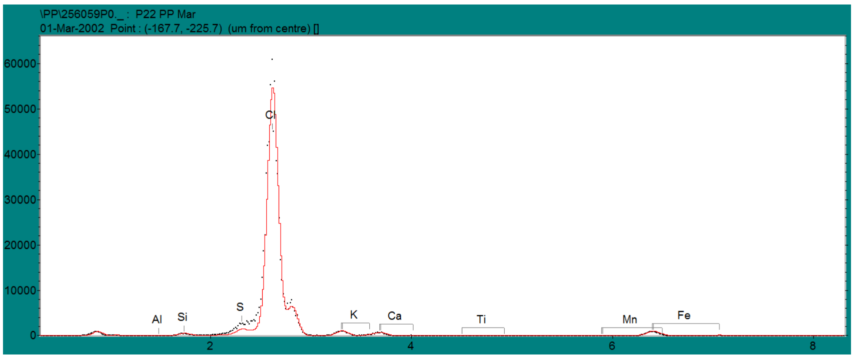

(a) Spectrum of point 59_{Cl} (Q = 105 nC)

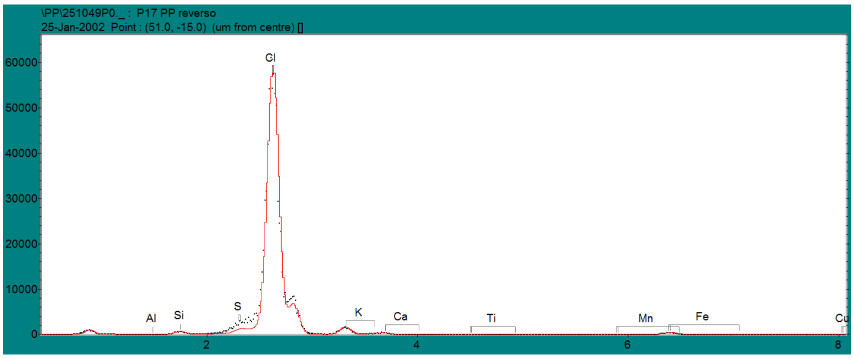

(b) Spectrum of point 49_{Cl} (Q = 112 nC)

Figure 4.16: PIXE spectrum of point 59_{Cl} and 49_{Cl}. Energy reported in keV. Almost the whole atomic X-ray emission are due to Cl atoms. It is distinguishable not only its K_α line but also the K_β. The red line in the graph is the fit of the spectrum used by OMDAQ2007 to estimate the elements concentrations.

Titanium particles

Other particles showing recurrent features, that can enable their identification, are characterized by an high Ti concentration. Titanium is present only in small particles and its concentration is usually very low in general analysis. One of these particles can be seen in maps of Fig. 4.17.

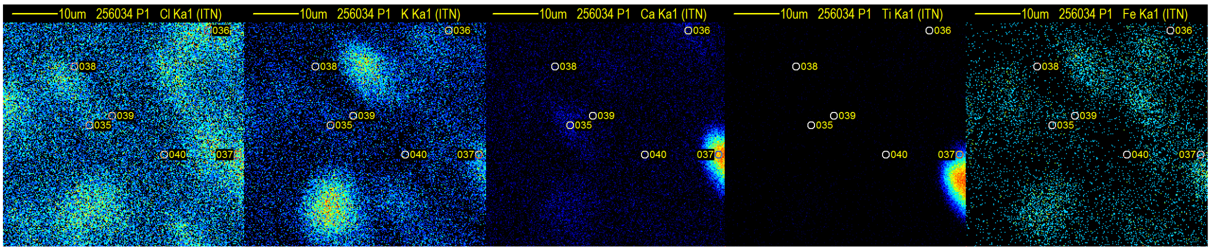

Figure 4.17: 53 x 53 μm^2 maps of Cl, K, Ca, Ti and Fe that refer to a surface scan of a PET sample exposed to water. Titanium characterized a particle in the surface deposit.

Analysis are effettuated for data that refer to point number 37_{Ti} of these maps and to point 36_{Ti} of Fig. 4.7. RBS spectrum of point 37_{Ti} and estimated deposits structure of both areas are reported in Fig. 4.18 and Table 4.12 respectively.

The two considered deposit regions are characterized by different thicknesses, 2.65 μm the one analyzed in point 36_{Ti} and 15 μm for the area numbered as 37_{Ti}. The composition of the deposit layer that best fit the respective RBS spectrum does not present interesting values. Besides the

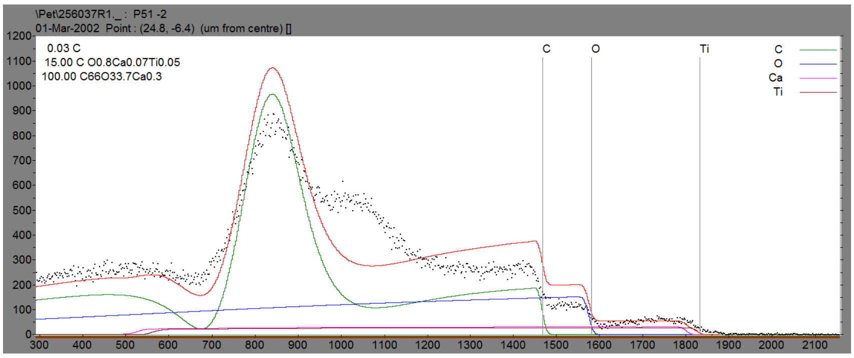

Figure 4.18: RBS spectrum of point 37_{Ti} (Q = 34 nC, $\chi^2 = 4.9$). Edge at high energy related to Ti basckscattered events. The red line in the graph is the spectrum simulated from the best composition fit given by OMDAQ2007. It is able to simulate properly the sample yield almost in the entire energy range. In the C resonance, however, there is a bump that the fit is not able to describe. The coloured lines are the yields of the individual element that compose the matrix.

Point	Thickness $[\mu m]$	C $[at.\%]$	O $[at.\%]$	Ca $[at.\%]$	Ti $[at.\%]$	Fe $[at.\%]$
36_{Ti} (PET)	2.65	54.2	37.4	2.2	5.3	0.8
37_{Ti} (PET)	15	52.1	41.7	3.6	2.6	

Table 4.12: Structure parameters that best fit the RBS spectrum for every analyzed point: thickness of the deposit layer and atomic composition. First layer, that is the C coating, and plastic baking layer, with fixed composition depending on the plastic, are not reported.

high presence of C and O, there is a significative fraction of Ti, compared to the analysis of other deposits. PIXE spectrum related to data of the area labelled with the number 37_{Ti} is visible in Fig. 4.19. On Table 4.13, the elements concentrations estimated by the OMDAQ2007 fitting routine for the two titanium deposit points are presented.

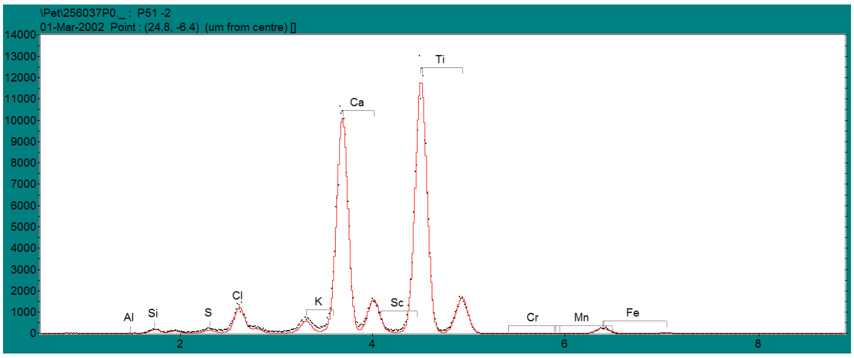

Figure 4.19: PIXE spectrum of point 37_{Ti} (Q = 34 nC). Ti X-rays are the main contribution in the spectrum but also Ca presents a comparable concentration.

The region corresponding to the thiner titanium deposit (36_{Ti}) presents an high concentration of Ti and Fe and trace of manganese. If looking at the atomic percentages of elements in the estimated composition of this deposit nothing can be concluded. However, calculating the ratio between Ti and Fe concentrations percentage, provided by PIXE analysis, it can be proposed that this is an Ilmenite particle ($FeTiO_3$) (Wynn [82]). Theoretical ratio between Fe and Ti

Point	Cl [%]	Ca [%]	Ti [%]	Mn [%]	Fe [%]
36_{Ti} (PET)	1.001 ± 0.008	0.608 ± 0.006	6.94 ± 0.02	0.328 ± 0.006	4.90 ± 0.02
37_{Ti} (PET)	0.220 ± 0.003	1.218 ± 0.004	2.28 ± 0.01	0.007 ± 0.001	0.128 ± 0.003

Table 4.13: Concentrations of the main elements (Cl, Ca, Ti, Mn and Fe) estimated for each analyzed point considering the deposit layer composition and the q-factor resulting from the RBS fitting routine.

concentrations [%] is 0.9 while the value calculated from data is 1.417 ± 0.008.
Deposit area labelled with point 37_{Ti} is characterized by an high concentration of Ti and Ca. Fe is not detected in this deposit. The particular mineral could be Rutile (TiO_2) (Wynn [82]), even if the matrix composition does not respect the chemical formula proportion. Ca and Ti are not correlated and do not compose the same grain. In fact, looking carefully at the maps of Ca and Ti, included in Fig. 4.17, one can notice that there are two different sediment particles very close to each other and probably intertwined. OMDAQ2007, using the monolayer approximation to estimate elemental concentrations, can not separate these two different particles during its fitting routine and this results in a monolayer deposit with a comparable concentration of both elements. Also comparing fit and data of the RBS spectrum (Fig. 4.18), is evident that this structure model is not the best approach to describe in depth the deposit: there is a counts rise near the C resonance that is not simulate adequately by the OMDAQ2007 fit.

To achieve more satisfactory results in the depth structure estimation, some of the data are evaluated with NDF. Although the procedure is time consuming, provided the RBS is well modelled, a good depth structure of the deposit can be defined and a better depth resolution obtained. The following example illustrates the degrees of improvement that can be achieved with NDF in the analysis of data regarding point 37_{Ti}. Ca, Ti and Fe are selected to be included in the analysis, being the elements with larger PIXE peak area. C and O are taken in account only for the RBS spectrum. “Fast” fit results can be seen in Fig. 4.20. NDF is able to find a depth structure that fits properly the RBS spectrum (Fig. 4.20 a). In particular, bottom layers composed by Ca and Ti explain the bump in the spectrum near the C resonance that with the monolayer approximation is not simulated. The PIXE elements peak area simulated with the depth structure of the fit are compatible with the data ones (Fig. 4.20 b), sign that the fit is effectively self-consistent with the two techniques. The depth structure estimated is composed by six layers: the C coating on top of the sample (0.2 μm), two layers composed mainly by C, O and Ca (1.9 and 6.9 μm), a thin layer of Ca, Ti and C (0.9 μm) and the last deposit layer, made by Ti and C (3.6 μm). The sixth layer is the plastic baking, the 100 μm layer with PET polymer fixed composition. This structure respects what is seen also in the maps. There are two different types of deposit, one of top of the other. Calcium particle is on top and it is approximately 8.9 μm (first two layers). Ti material is attached to the plastic and is ∼ 3.6 μm size. In between, a thin intermediate layer that can be seen as an interface between the two particles. The depth profile is schematized in Fig. 4.20 c, in which the atomic percentage of C, O, Ca, Ti and Fe are represented as a function of depth.

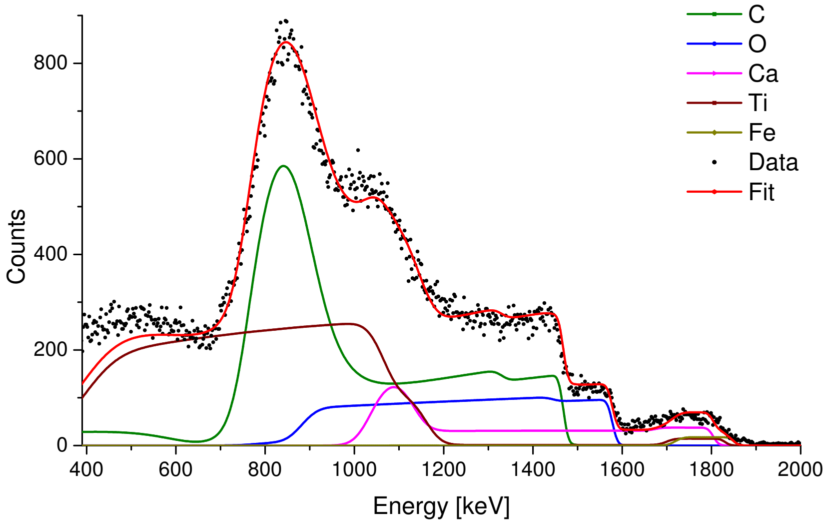

(a) NDF fit of the RBS spectrum of point 37_{Ti}

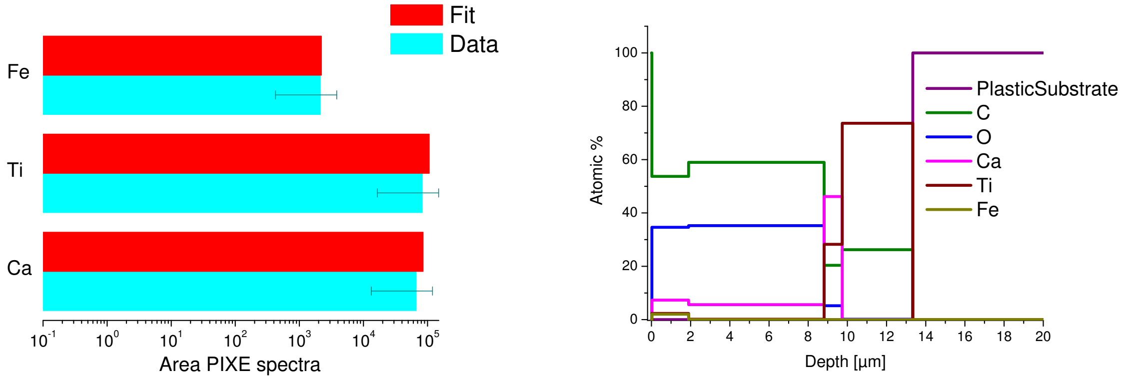

(b) Comparison between simulated and experimental PIXE yields

(c) Estimated deposit depth structure

Figure 4.20: Results of a “Fast” fit of RBS and PIXE spectra of point 37_{Ti}, provided by NDF. The fit of the RBS spectrum is improved respect to OMDAQ2007s (a) since the analysis are done accordingly also to PIXE data, that restricts the possible depth structure. PIXE yields of the simulated depth structure have to be consistent with the experimental yield of X-ray emission (b). The best structure of the analyzed, provided by the NDF algorithm, is composed by six layers with different atomic percentage compositions (c).

NDF analysis, however, do not gives further proof on the nature of the titanium particle but rather estimates the presence of C, instead of O, together with Ti. Therefore is not possible to assert which is the particles material. These different results are probably consequence of the presence of C and O also in the polymer, that amplifies the ambiguities of the RBS spectrum, as well as of the fact that C and O are not detected with PIXE and their peak area cannot be included in the NDF analysis method.

Mixed deposit

The majority of the point analysis are related to mixed deposits of very fine particles, which can not be resolved by the dimensions of the beam. Estimated concentrations, in these cases, do not show any evident correlation between elements. The points discussed as examples are reported on Table 4.14 and correspond to maps with similar deposit distribution to the ones of Fig. 4.10. On this Table, thickness resulting from RBS depth structure analysis and estimated concentrations from PIXE spectrum can be found. Structure composition that fit the RBS spectrum are not reported because, given the deposit complexity and the difficulties in distinguish elements looking at the RBS spectrum, not indicative of any interesting deposit features. Selected points characterize regions with different features, from area without any deposit layer (number 67_{mix}) to deposits layer of different thickness, ranging from 0.02 to 9 μm. Neither the element concentrations show any clear pattern, and is not possible to recognize the specific mineral among the sea water constituents. Points are characterized by high concentrations of a couple of elements each at least, and other elements quantity is not neglectable compared to the main ones as well. Recurrent elements in those general deposits are S, K, Cl, Ca and Fe, showing that deposits on top of the plastic samples exposed to water are mainly sediments and abiotic materials. Small biologic particles can be also mixed in these deposits but, if they are not clearly distinguishable from the distribution on the maps, their identification is not straight-forward. The only reference used in the analysis to characterize this particle is Ca (see 4.4.3) that is also a component of several sediment particles.

Point	Thickness [μm]	S [%]	Cl [%]	K [%]	Ca [%]	Fe [%]
24_{mix} (HDPE)	0.42	0.95 ± 0.06	2.07 ± 0.05	0.33 ± 0.04	1.064 ± 0.003	0.10 ± 0.02
28_{mix} (HDPE)	5.83	0.247 ± 0.008	1.623 ± 0.008	1.774 ± 0.008	0.401 ± 0.003	2.21 ± 0.01
29_{mix} (HDPE)	0.02	4.2 ± 0.9	28.1 ± 0.7	2.3 ± 0.4	0.235 ± 0.001	0.9 ± 0.2
31_{mix} (PET)	9.35	0.163 ± 0.005	0.686 ± 0.005	0.387 ± 0.004	2.933 ± 0.009	0.689 ± 0.007
35_{mix} (PET)	2.40	0.337 ± 0.009	0.231 ± 0.006	0.104 ± 0.004	0.269 ± 0.005	0.089 ± 0.005
67_{mix} (PP)		0.006 ± 0.002	0.019 ± 0.001	0.0019 ± 0.0004	0.0034 ± 0.0004	0.0023 ± 0.0005
70_{mix} (PP)	1.24	0.23 ± 0.03	3.35 ± 0.04	1.62 ± 0.02	0.42 ± 0.01	2.73 ± 0.05
71_{mix} (PP)	1.46	0.27 ± 0.02	1.10 ± 0.02	2.71 ± 0.03	0.64 ± 0.02	4.39 ± 0.06

Table 4.14: Structural and compositional analysis of mixed deposit area. Regarding each analyzed point, the estimated thickness of the deposit layer resulting from the RBS fit are reported together with the estimated concentrations from the PIXE spectra.

Even more than in the other deposit regions, the monolayer approximation limits the OMDAQ2007 analysis, since mixed deposit regions are characterized mainly by overlapped materials of different nature. In order to have an evaluation of what could be the depth structure of this kind of deposit, data related to point 31 (marked in maps of Fig. 4.21) are analyzed with NDF. "Fast" fit results are presented in Fig. 4.22. Fe, K, Cl, Ca, and Si are included in the analysis, being the main components of the PIXE spectrum. The simulated depth structure is able to fit the RBS spectrum, especially in the resonance region (Fig. 4.22 a). Its wider shape is due to the multilayer structure, in particular to the presence of Ca in layers near to the plastic surface, as it can be noticed from the individual contribution of calcium at the fit of the spectrum (pink line in Fig. 4.22 a). The calculated PIXE yields for Si, Cl, K, Ca and Fe show a remarkable

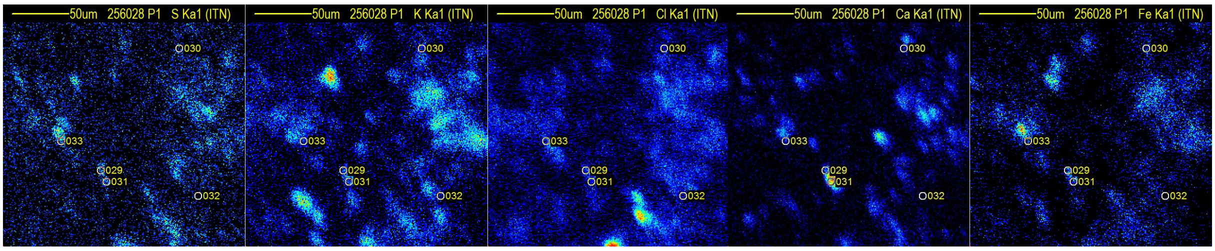

Figure 4.21: 265 x 265 μm^2 maps of Cl, K, Ca, Ti and Fe that refer to a surface scan of a PET sample exposed to water. Point analysis labelled as 31 hits a region of deposit characterized by an high concentration of Ca and the simultaneous presence of Cl and Fe.

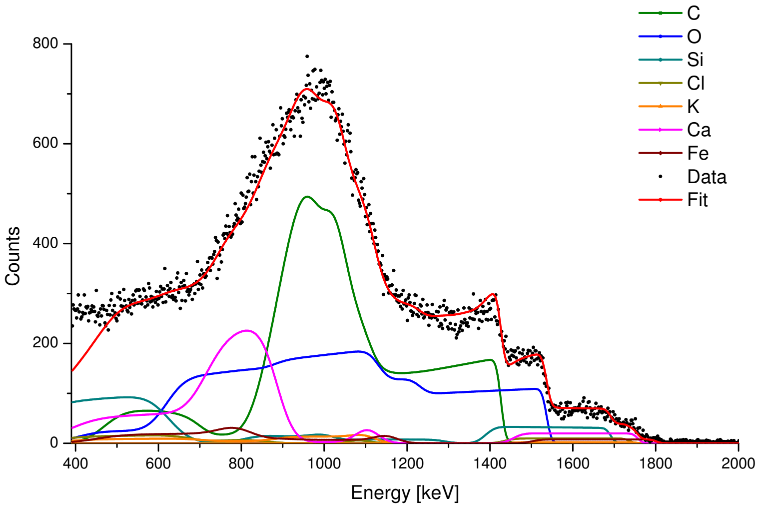

(a) NDF fit of the RBS spectrum of point 31_{mix}

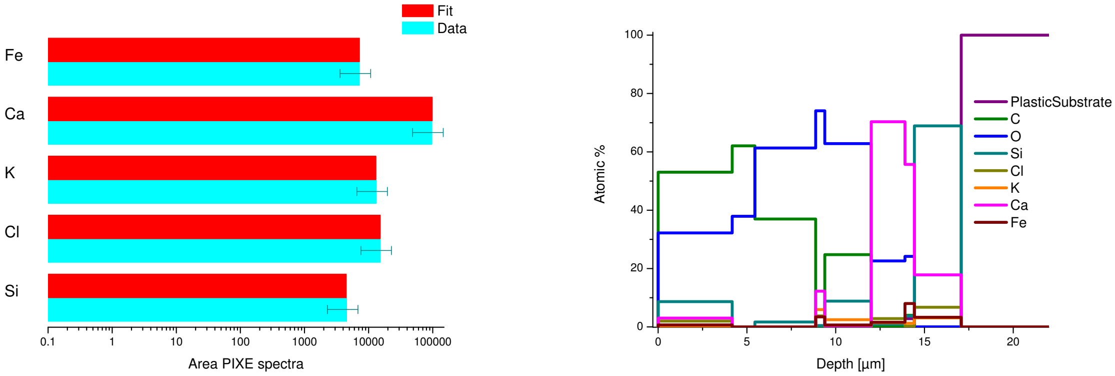

(b) Comparison between simulated and experimental PIXE yields

(c) Estimated deposit depth structure

Figure 4.22: Results of a "Fast" fit of RBS and PIXE spectra of point 31_{mix}, provided by NDF. The fit of the RBS spectrum is improved respect to OMDAQ2007s (a) since the analysis are done accordingly also to PIXE data, that restricts the possible depth structure. PIXE yields of the simulated depth structure have to be consistent with the experimental yield of X-ray emission (b). The best structure of the analyzed, provided by the NDF algorithm, is composed by nine layers with different atomic percentage compositions (c).

agreement with the experimental data. The estimated depth profile is composed by 8 layers with different thicknesses and composition, compatible with a mixture of organic matter and earth crust materials (Santos-Echeandìa et al. [83]). The depth structure evidences a larger organic contribution at the deposit surface (higher C atomic percentage in the first three layers) and more oxidized Fe, Ca and Si earth crust materials (Santos-Echeandìa et al. [83]) deeper in the deposit. Interestingly, Cl is also present at deeper layers, suggesting proximity of the substrate that may favour its diffusion into the polymer matrix.

4.4.2 Transversal profile

During transversal profile scans of exposed samples, only sediment deposit have been found and analyzed. Examples of linescans of both high and low loaded deposit regions are shown in Fig. 4.23 and 4.24 respectively.

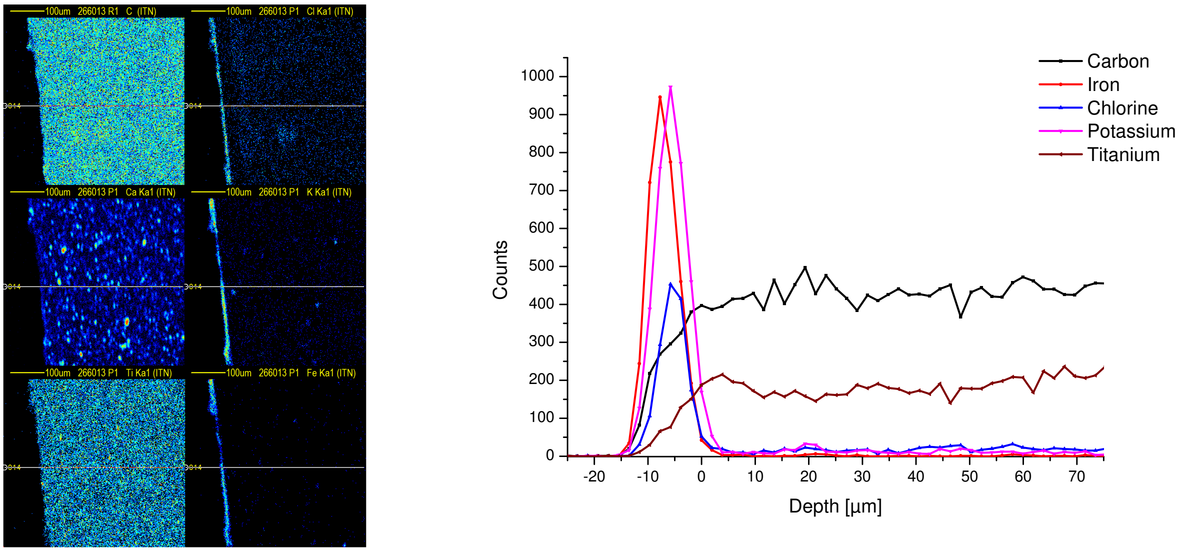

(a) 530 x 530 μm^2 maps of C, Ca, Ti, K, Cl, Fe

(b) Distribution of C, Fe, Cl K and Ti resulting from a linescan (Q = 145 nC)

Figure 4.23: 530 x 530 μm^2 maps (a) resulting from a scan of the transversal section of an HDPE samples exposed to water and with high concentration of material in its surface. Main elements (C, Fe, Cl K and Ti) distributions (b), provided by a linescan, allow to analyze directly the depth structure of the deposit.

Element distributions correspond to the linescans marked in the maps. Since both examples are of HDPE samples, the plastic substrate is recognizable in the maps from the C, Ca and Ti distributions (Figs. 4.23, 4.24 a). In the linescans, illustrated in Figs. 4.23, 4.24 b, references to distinguish the plastic from the deposit materials, are the C and Ti counts. Ca, distributed in-homogeneously in HDPE polymers, is not reliable. Deposit material is marked on the maps by Cl, Fe and K events on the plastic left edge. In the plastic interior there is no evidence of the presence of these elements. This is confirmed by the linescans analysis, which evaluate that deposit elements are concentrated in the plastic edge with Gaussian-like distributions. On table 4.15, FWHMs values of the different element distributions of linescans with different PIXE resolution are reported, included data of the linescan 14 (Fig. 4.23). This parameter of the Gaussian-like distribution is synonym of the deposit thickness (see Appendix A). The

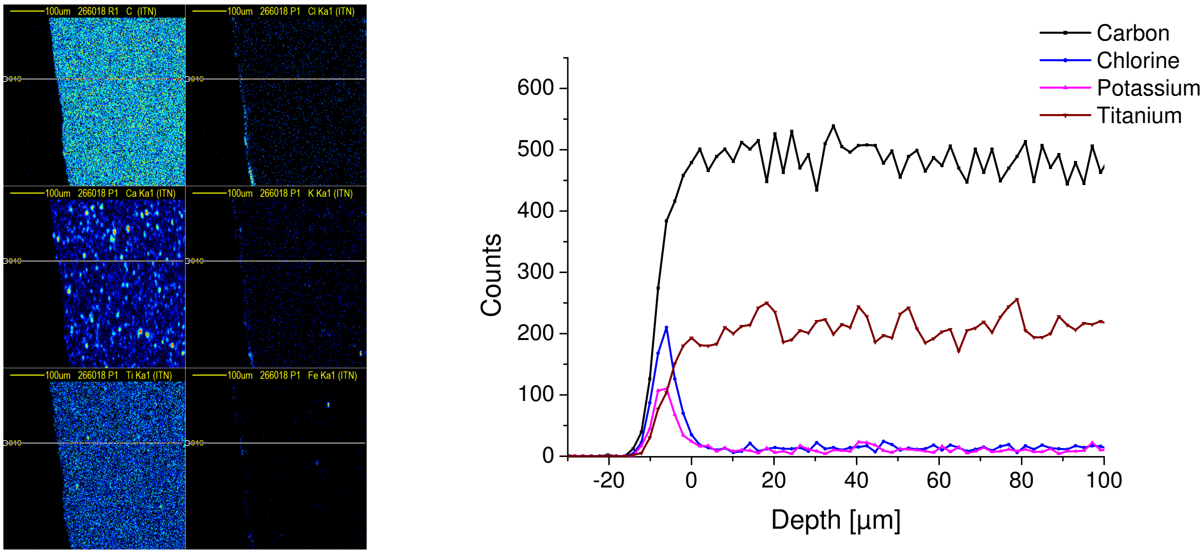

(a) 530 x 530 μm^2 maps of C, Ca, Ti, K, Cl, Fe

(b) Distribution of C, Cl K and Ti resulting from a linescan (Q = 172 *nC*)

Figure 4.24: 530 x 530 μm^2 maps (a) resulting from a scan of the transversal section of an HDPE samples exposed to water and with low concentration of material in its surface. Main elements (C, Cl K and Ti) distributions (b), provided by a linescan, allow to analyze directly the depth structure of the deposit.

	Linescan 11		Linescan 03		Linescan 14	
Element	FWHM [μm]	Rel. Height	FWHM [μm]	Rel. Height	FWHM [μm]	Rel. Height
Si	19 ± 5	0.06			5 ± 2	0.18
S	18 ± 3	0.10			6 ± 2	0.17
Cl	18 ± 2	0.74	15 ± 2	0.19	5 ± 2	1.00
K	17 ± 2	0.39	15 ± 2	0.42	6 ± 2	2.48
Ca	11 ± 2	1.01	10 ± 2	0.69		
Ti	14 ± 2	3.03				
Fe	14 ± 2	2.07	22 ± 2	0.12		

Table 4.15: FWHM of the Gaussian distribution of surface deposits in different linescans, characterized by different resolutions. In particular, linescan 11 has a spatial resolution of 5.2 μm, the number 03 of 4.3 μm and linescan 14 of 3.2 μm. The estimated deposit thickness ranges from 5 to 22 μm. Together with the distribution FWHM is reported also the peaks height divide by the number of C counts inside the plastics.

relative heights of the peak to the average C constant counts of the same linescan can also be found on Table 4.15, in order to compare the estimated widths for elements present in high quantity from the low concentration ones. Superficial distributions of different elements are characterized by compatible FWHMs. Small differences can be due to imaging uncertainties of the PIXE system or to the complexity of the deposit, already stated more than once. The multilayer structure of deposits implies that elements are present at different depths and in different quantities, thus presenting different elemental depth distributions. Statistic does not seem to have a correlation with the estimated deposits widths, since peaks with lower statistic are not necessarily characterized by a wider or smaller FWHM.

Considering the results of the different linescans, the deposits thicknesses estimated variate in a range between 5 and 20 μm. The resolution can influence these estimations, setting a lower limit to the thickness estimation: better resolution enables to reach a better depth precision in the linescans. However, comparing the values reported on the Table 4.15, is not immediate to conclude the real impact of the spatial resolution on these analysis. Reported FWHM are smaller when related to days in which the system have a better resolution but this can be due also to the effective deposit depth structure, thiner than in the other analysis.

In conclusion, linescans analysis can provide a direct estimation of the thicknesses range of the sediment deposit on top of the exposed plastics samples, that results to be from 5 to 20 μm. Software estimations are coherent with those values, proving the goodness of the softwares fitting algorithm. Elements absorption and plastic matrix changes, in the interface between deposit and plastic, are not investigable with this type of analysis. The uncertainties just discussed have to be summed to the arbitrary of the zero definition for the plastic edge and this gives an error in defining the relative position of deposit and plastic that overcome the length of the possible diffusion of elements inside the plastic.

4.4.3 Biotic deposit

Biotic material is also found on top of the samples during the analysis. Maps of deposit of this nature can be seen in Fig. 4.25, as well as in Fig. 4.7.

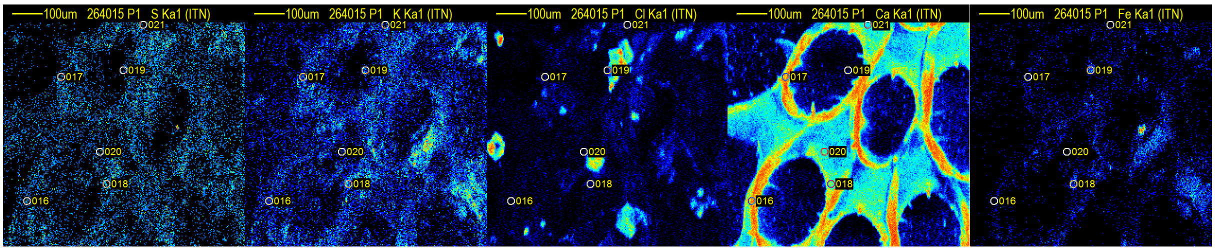

Figure 4.25: 795 x 795 μm^2 maps of S, Cl, Ca, K and Fe that refer to a surface scan of a PET sample exposed to water. In this region biota are attached in the plastic sample surface.

The first maps are discussed in Section 4.3, while describing the deposits distributions on plastics surface. Biologic material found in the scan of maps of Fig. 4.25, besides having a different distribution of the cells, grouped together and not arranged in a line, has equivalent elements distributions patterns. Points are selected in order to analyze, in particular, three different region of the biotic deposits: cell walls (16_{bio}, 17_{bio} and 18_{bio} in Fig. 4.25 and 37_{bio}, 38_{bio} in Fig. 4.7), intracellular media (20_{bio}, 21_{bio} in Fig. 4.25 and 41_{bio}, 42_{bio} in Fig. 4.7) and possible vacuole-like regions (39_{bio}, 40_{bio} in Fig. 4.7). Softwares analysis operations are the same followed during the study of sedimentary deposits. Example of an RBS spectrum is reported in Fig. 4.26, correspondent to point area 16_{bio} in Fig. 4.25. Results of OMDAQ2007 depth structure fits of all the considered points can be found on Table 4.16. Data are organized looking at the region they belong to: first the cell walls analysis results, then the intracellular material and lastly inside the vacuole-like regions.

The reported example of RBS spectrum presents a very sharp barrier in correspondence to the characteristic energy of protons backscattered from Ca nuclei. The barrier width indicates also

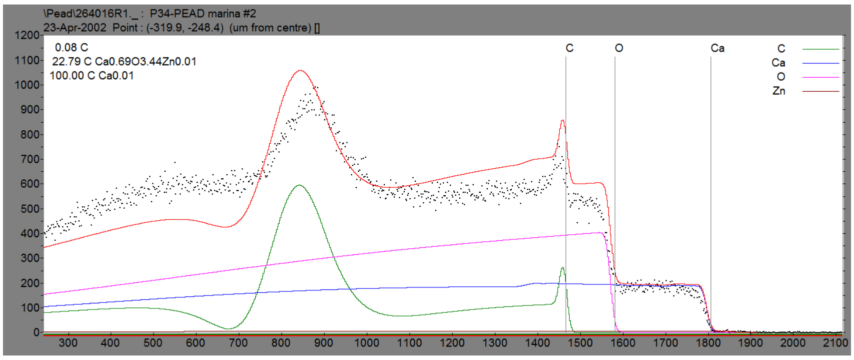

Figure 4.26: Spectrum of point 16_{bio} (Q = 151 nC, $\chi^2 = 5.2$). The red line in the graph is the spectrum simulated from the best composition fit given by OMDAQ2007.

Point	Thickness [μm]	C [$at.\%$]	O [$at.\%$]	Ca [$at.\%$]
16_{bio} (HDPE)	22.8	19.5	66.9	13.4
17_{bio} (HDPE)	28.4	34.5	56.7	8.8
18_{bio} (HDPE)	11.0	17.5	53.9	28.6
37_{bio} (PET)	25.3	13.6	73.8	12.6
38_{bio} (PET)	25.5	3.4	79.9	16.7
20_{bio} (HDPE)	20.4	25.6	57.5	16.4
21_{bio} (HDPE)	5.8	35.6	48.0	16.4
41_{bio} (PET)	5.0	20.3	64.3	15.4
42_{bio} (PET)	5.8	47.2	30.3	22.5
39_{bio} (PET)	1.7		86.2	13.8
40_{bio} (PET)	2.8	68.4	27.8	3.8

Table 4.16: Structure parameters that best fit the RBS spectrum for every analyzed point: thickness of the deposit layer and atomic composition. First layer, that is the C coating, and plastic baking layer, with fixed composition depending on the plastic, are not reported.

the large thickness of this deposit, confirmed by the following analysis that estimate a deposit width of ∼ 20 μm. It is interesting to notice that the estimated thicknesses have coherent values within the analyzed points. Cell walls are about 25 μm thick. Point number 18_{bio} of Fig. 4.25 is not completely on a wall and thus results thiner. Intracellular media have a thickness of ∼ 5 μm, lower than the walls, as it can be expected. Point 20_{bio} is an exception: it results to be thicker (20.4 μm) probably because it covers also the Cl aggregate close to the selected area, as can be seen in Fig. 4.25. Lastly, inside the vacuoles, deposit is very thin, ∼ 2 μm, confirming that it is a low loaded region. The atomic percentage composition of the simulated deposit layer is characterized by a significative fraction of calcium in all the analyzed points.

Using these compositions and the Q-factor estimated during the RBS fitting routine, concentration estimations are done analyzing the correspondent PIXE spectra. Spectrum related to point analysis number 16_{bio} of Fig. 4.25 is presented in Fig. 4.27.

Except for analysis of area corresponding to vacuoles, the concentrations estimated with PIXE events show an high concentration of Ca, in the range of 13-20 %. Other elements (Cl, K and Fe) concentrations are neglectable compared to calciums. Some of the analyzed areas present

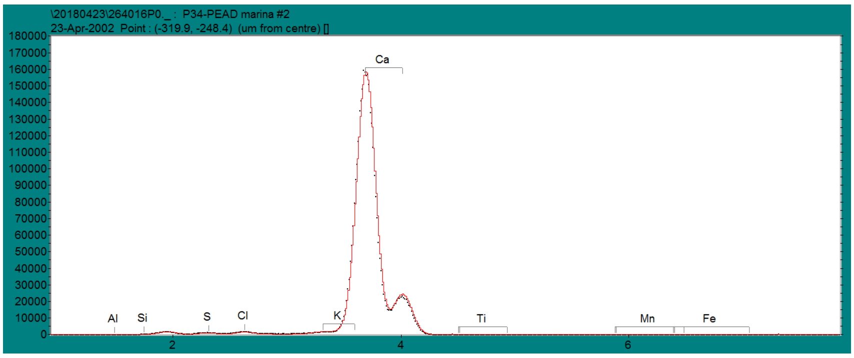

Figure 4.27: PIXE spectrum of point 16_{bio} (Q = 151 nC), mainly composed by the Ca characteristic X-rays emission lines.

Point	Cl [%]	K [%]	Ca [%]	Fe [%]
16_{bio} (HDPE)	0.218 ± 0.003	0.071 ± 0.005	14.755 ± 0.009	0.013 ± 0.002
17_{bio} (HDPE)	1.333 ± 0.005	0.265 ± 0.007	19.89 ± 0.01	0.016 ± 0.003
18_{bio} (HDPE)	1.038 ± 0.007	0.698 ± 0.007	16.47 ± 0.02	2.94 ± 0.01
37_{bio} (PET)	0.301 ± 0.002	0.051 ± 0.002	9.135 ± 0.008	0.0162 ± 0.0009
38_{bio} (PET)	0.139 ± 0.002	0.103 ± 0.003	13.01 ± 0.01	0.112 ± 0.002
20_{bio} (HDPE)	0.128 ± 0.002	0.019 ± 0.002	5.113 ± 0.005	0.0021 ± 0.0007
21_{bio} (HDPE)	1.514 ± 0.007	0.397 ± 0.007	16.04 ± 0.02	0.109 ± 0.003
41_{bio} (PET)	0.716 ± 0.006	0.092 ± 0.006	19.05 ± 0.02	0.013 ± 0.002
42_{bio} (PET)	0.911 ± 0.006	0.113 ± 0.005	13.27 ± 0.02	0.153 ± 0.004
39_{bio} (PET)	2.26 ± 0.02	2.33 ± 0.02	4.51 ± 0.02	0.16 ± 0.03
40_{bio} (PET)	3.73 ± 0.01	0.097 ± 0.003	1.99 ± 0.01	0.004 ± 0.004

Table 4.17: Concentrations of the main elements (Cl, K, Ca, and Fe) estimated for each analyzed point of biological deposit, considering the deposit layer composition and the Q-factor resulting from the RBS fitting routine.

higher quantities of these minor elements, probably due to the overlapping with abiotic deposits. Regions inside the vacuoles, instead, are still dominated by Ca concentration, as it is expected since the area is surrounded by cell walls, but other elements are present in comparable quantities. Any particular consideration about the particular compound that characterizes biotic deposits can be done looking at the percentage concentrations given by PIXE analysis, provided that, with this technique, C and O concentrations are not estimated (biological material is composed mainly by $CaCO_3$). More hints are given by the matrix atomic compositions resulting from the fitting routine of OMDAQ2007. Ca, C and O atomic percentages should respect the proportion 1:1:3. Ratios between these three elements, for points corresponding to cell walls and intracellular media only, are reported on Table 4.18.

Results are slightly compatible with the theoretical proportion. However, it has to be remembered that, matrix compositions resulting from the RBS fitting routine of OMDAQ2007, are not the most accurate values on which rely for further considerations. Moreover, every polymers contains C, and HDPE also calcium, that can thus amplify the ambiguities during the spectrum fitting routine.

Point	Ca/C	O/C	O/Ca
16_{bio} (HDPE)	0.7	3.4	5.0
17_{bio} (HDPE)	0.3	1.6	6.5
18_{bio} (HDPE)	1.6	3.1	1.9
37_{bio} (PET)	0.9	5.5	5.9
38_{bio} (PET)	4.9	23.6	4.8
20_{bio} (HDPE)	0.6	2.3	3.5
21_{bio} (HDPE)	0.5	1.4	2.9
41_{bio} (PET)	0.8	3.2	4.2
42_{bio} (PET)	0.5	0.6	1.3

Table 4.18: Ratios between the *at.*% of Ca, C and O estimated in the deposit layer of biotic material during the RBS fitting routine. The proportion between those elements should be Ca:C:O = 1:1:3.

Even if the RBS spectrum is fitted by OMDAQ2007 with a good χ^2, data related to the area labelled with the number 16_{bio} in maps of Fig. 4.25 have also been analyzed using NDF. In this way, a precise estimation of the depth structure of a biologic deposit can be achieved, aiming to understand in particular its multilayer structure. "Fast" fit results are presented in Fig. 4.28. Compared to the fit visible in Fig. 4.26, NDF provides a better simulation of the RBS spectrum (Fig. 4.28 a), according to PIXE data (Fig. 4.28 b). Included elements in the analysis are Ti, Ca and Cl (Ti because it composes HDPE, plastic of this particular sample). The layer structure and the relative elemental composition of each layer can be represented by plotting the fitted depth profile with the linear depth scale (Fig. 4.28 c). Estimated depth profile of this biologic deposit is composed by five layer. Apart the first thin C coating layer, the second layer composition (16 *at.*% C + 68 *at.*% O + 16 *at.*% Ca) reproduces the atomic percentages in calcium carbonate ($CaCO_3$) and the third layer shows a composition closer to an intracellular milieu, less Ca, more C and O (26 *at.*% C + 66 *at.*% O + 9 *at.*% Ca). The fourth layer is noteworthy as it reveals a mixed composition of the cell wall and the polymer (0.2 *at.*% C + 2.2 *at.*% O + 0.4 *at.*% Cl + 34 *at.*% Ca + 63 *at.*% substrate). This mixed composition is compatible with the required cell adhesion to the substrate (the 5^{th} layer is 100 μm HDPE standard composition) and may reflect the biodegradation of the polymer surface carried out by enzymatic hydrolysis of specific polymer bonds (Holmes et al. [11], Restrepo-Florez et al. [13], Zheng et al. [84]). Total thickness of the estimated structure is ~ 20 μm, as resulted also in OMDAQ2007 analysis (22.8 μm). During the transversal analysis, it was not possible to identify and scan a biological deposit, thus comparison of the estimated depth structure with direct measures can not be effectuated. Nevertheless, assuming that the deposit thickness is quite similar to the sedimentary one, the value estimated are in agreement with the direct measurements described in Section 4.4.2.

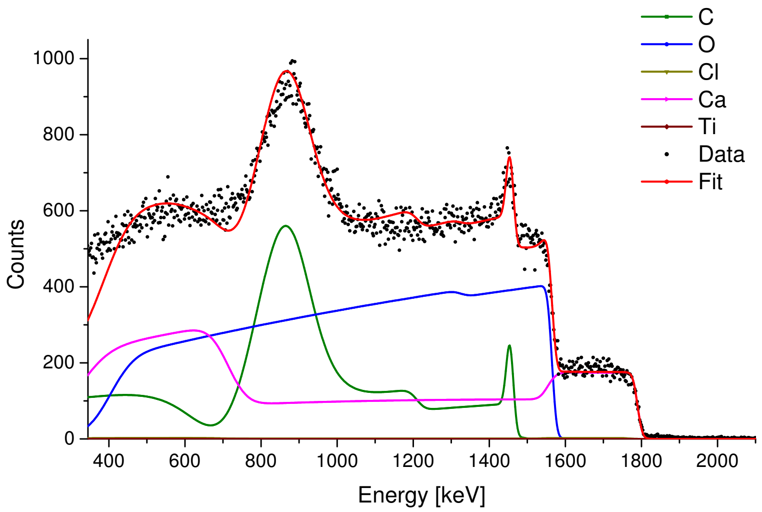

(a) NDF fit of the RBS spectrum of point 16_{bio}

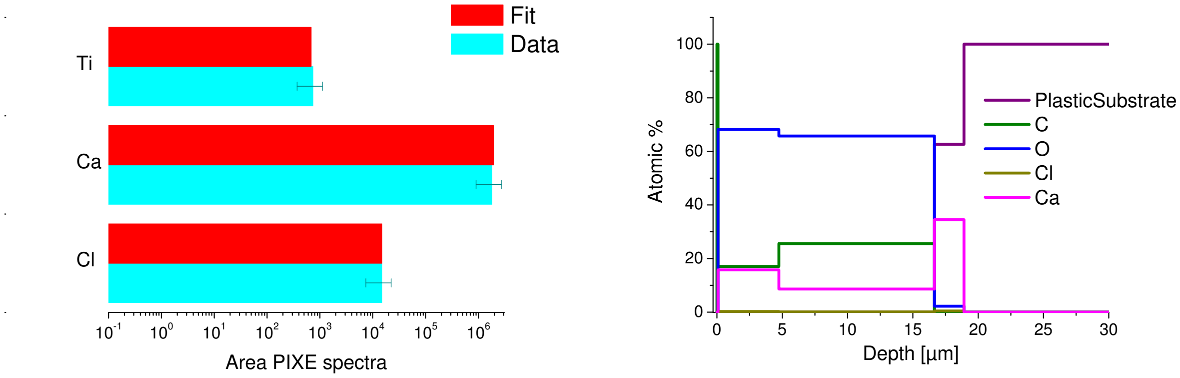

(b) Comparison between simulated and experimental PIXE yields

(c) Estimated deposit depth structure

Figure 4.28: Results of a “Fast” fit of RBS and PIXE spectra of point 16_{bio}, provided by NDF. The fit of the RBS spectrum is improved respect to OMDAQ2007s (a) since the analysis are done accordingly also to PIXE data, that restricts the possible depth structure. PIXE yields of the simulated depth structure have to be consistent with the experimental yield of X-ray emission (b). The best structure of the analyzed, provided by the NDF algorithm, is composed by five layers with different atomic percentage compositions (c).

4.5 Chlorine absorption

Cross-sections linescans are used also to search for evidence of elements absorption in the plastic interior. If in the range of the linescans referred to the plastic inner part there are counts regarding elements that do not compose the plastic polymer itself, it means that they are absorbed inside it. In more than one linescan, of samples of both the polymers which cross section is analyzed (PET and HDPE), Cl distribution exceeds the plastic edge and counts related to this elements can be observed inside the samples. Examples are shown in Fig. 4.29.

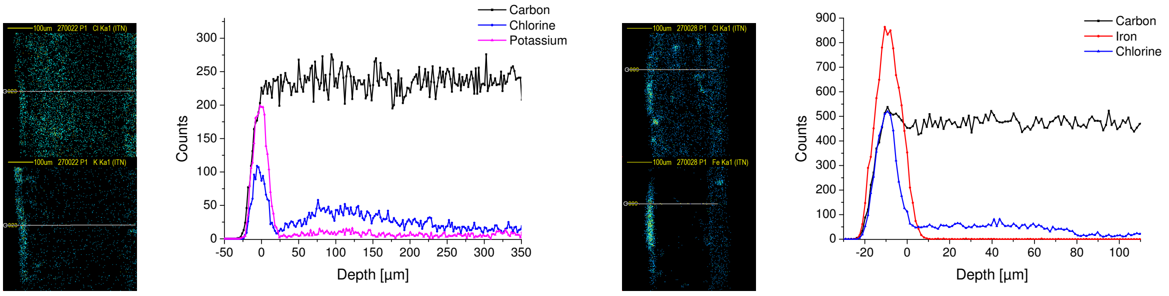

(a) Low Cl diffusion HDPE (Q = 169 μC)

(b) Low Cl diffusion PET (Q = 184 μC)

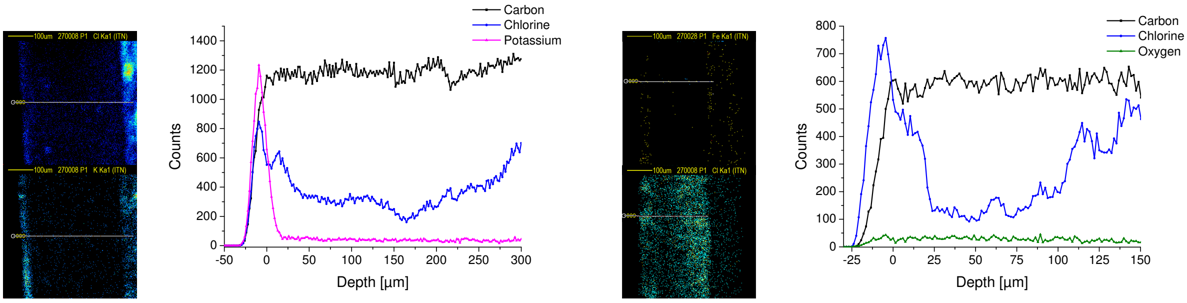

(c) Cl diffusion from both sides HDPE (Q = 1009 μC)

(d) Cl diffusion from both sides PET (Q = 205 μC)

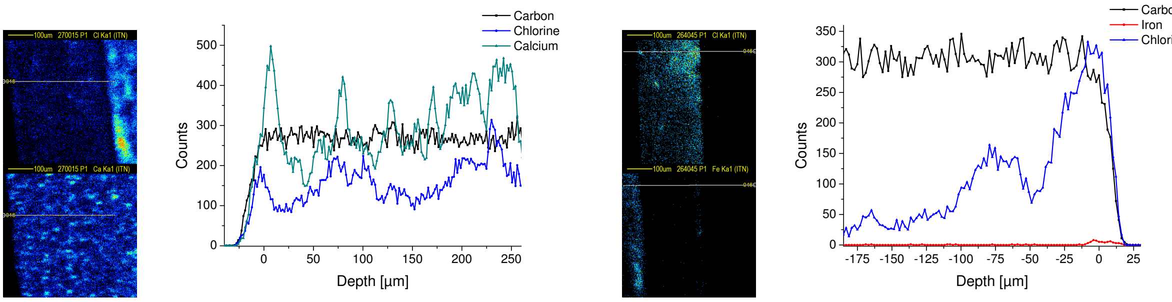

(e) Irregular Cl diffusion HDPE - correlation with Ca aggregates (Q = 226 μC)

(f) Irregular Cl diffusion PET (right edge analyzed) (Q = 79 μC)

Figure 4.29: Several examples of transversal section analysis of polymers that show Cl adsorption inside the matrix. This phenomenon affects both HDPE (a), (c), (e) and PET (b), (d), (f). The adsorption is irregular and only few features can be guessed: low adsorption (a), (b); diffusion from both sides (c), (d); irregular diffusion (e), (f).

This phenomenon does not have any regular and constant feature. Moreover, some samples present regions with Cl absorption and others without. Correlation with the surface deposits is inspected, without finding any regularity: the diffusion inside the plastic is observed with an high deposit on the surface (Linescans of Fig. 4.29 a, b, c) but also without any deposit on it of other elements (Linescans d, e, f). Some recurrent features of the diffusion in both type of plastics have been summed up after having analyzed all the cross sections data: low Cl absorption (a, b), exponential diffusion from both plastics surfaces (c, d) and irregular distribution inside the plastic (e, f). In this last case, only for HDPE plastic, diffused Cl could follow the irregular distribution of calcium, that composes the plastic polymer.

Masks of the inner plastic area on the transversal analysis maps enable to study the chlorine concentration inside the plastic. With this analysis option, dependence on time of Cl diffusion is also investigated, dividing, during the OMDAQ2007 analysis, linescans regarding samples with different exposition time (7 and 30 days). Averages between concentrations of data of the same sample are done (including either scans with Cl diffusion and without). After that, averages of concentrations of data regarding samples with the same exposition time are done. The result, for HDPE and PET, are shown in Fig. 4.30.

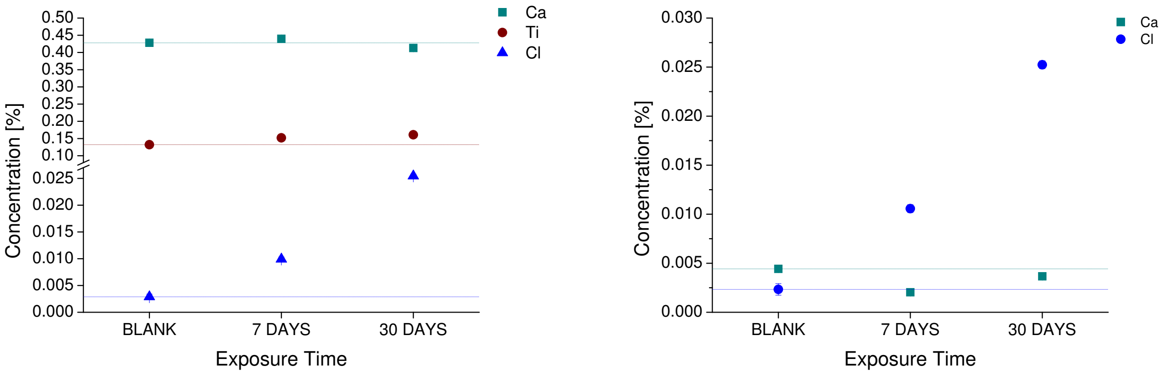

(a) HDPE

(b) PET

Figure 4.30: Average concentration of Cl in the interior of HDPE (a) and PET (b) samples in function of the exposure time (7 and 30 days). Together with the estimated Cl is reported also the time-depending concentration of Ca and Ti for HDPE and of Ca for PET. These are trace elements of the relative polymers and, being constant in time, they confirm the Cl increase inside the polymer is due to its diffusion from the water. The horizontal lines are significative of the correspondent element concentration in blank samples.

Concentrations of Cl are estimated using a single 100 μm layer, since it is assumed that its presence is inside the sample matrix. The composition of the layer used for the PIXE analysis depends on the polymer of the sample. Together with the Cl concentration, Ca and Ti values for HDPE samples are also reported, showing that their average are constant inside all the samples and during time. For PET, similar consideration are done using the Ca concentration inside the polymer (even if it is a minor element). The chlorine concentration inside both the plastics goes up to 0.025 % after 30 days of exposure and seems to have similar trends during time. However, more scans should be analyzed of different samples but also of different regions of the same sample. In fact, the estimations done depend on which and how many regions of the plastics have been analyzed. Analysis of samples with an intermediate exposure time could also help to investigate this aspect of the interaction of plastic polymers with Cl ions. Nevertheless, what is assessed clustering PIXE and RBS in direct transversal analysis, is that plastic exposed in aquatic environment adsorbs Cl ions. This may have an important role in the degradation of

plastic debris that float in water (mainly salty water since Cl composes salt particles).
Analysis of surface scans data, using either OMDAQ2007 and especially NDF, have not shown any evidence of this process. Once, during the discussion of the NDF analysis of the mixed deposit region (Fig. 4.22), the Cl presence at deeper layers has been interpreted as a suggestion of the diffusion of Cl ions into the polymer matrix, given the proximity with the substrate. However, the elements of interest have a low yield relative to matrix, due also to the low concentration of these elements if absorbed into the polymer (direct measurements estimates 0.025 % of Cl absorbed (Fig. 4.30)). Furthermore, straggling in upper layer of the deposit and attenuation of the incoming energetic particles by the materials in the deposit also limit the analysis capacity in the evaluation of polymer-deposit interaction and matrix changes. These do not permit to model the diffusion of Cl or any other element in the plastic substrate using surface analysis and the dedicated softwares. To assess matrix changes the element yield should overcome the uncertainty of the fit of the upper layers and the matrix.

Chapter 5

Conclusions and Future Work

The knowledge on the interaction mechanisms between plastic debris and the main constituents of aquatic ecosystems is expanded by means of simultaneous PIXE and RBS analysis, provided by the CTN nuclear microprobe. These two techniques present complementary characteristics that, combined together with the use of the microbeam, permit to inspect important aspects of the weathering of plastics in natural environment, in particular in estuarine and marine ecosystems.

The imaging capability of the microprobe, together with the multi-elemental feature of PIXE and RBS analysis, enables to determine recurrent patterns in the elements distributions on the plastic surface. Detected elements combining the two techniques are: C, O, Si, P, S, Cl, K, Ca, Cl, Ti, Mn, Fe, Br, Sr and I. Maps of surface large scans resolve the morphology of these elements with μm precision. The most common detected elements are Si, S, Cl, Ca, K, Ti and Fe, fingerprints of both biotic and sediment materials. Although the individual distributions may be not correlated, agglomerates of different elements are frequently observed, reflecting the complex multilayer structure of the film that covers plastics when exposed to marine environments.

More details on the depth profile of deposited materials are furnished by means of OMDAQ2007 and NDF, dedicated analysis softwares which integrate the possibility to cluster data coming from PIXE and RBS. The results obtained enable to determine, firstly, the typical thickness of the deposit layer on top of the exposed specimens, ranging from few nm up to 20 μm. The substrate polymer of the sample is not related to the quantity of material on top of the plastics and, locally, neither is the immersion time. A prolonged exposure to water causes only a difference in the global amount of materials in plastics but in the analysis of specific regions of the dimension of few μm dissimilarities are not observed. The multilayer structure is confirmed by the NDF analysis. The depth profile is estimated with nm precision, enabling, for instance, to evaluate the various layers that compose the walls of cells, to discriminate two overimposed particles and to prove the multiplex composition of the deposit. Also, NDF analysis suggested that biota may have an important role in altering the surface of the polymer, although the assessment of the polymer-deposit interaction and matrix changes is not straightforward. The main elements that compose polymers (C and O) are common constituent also of the deposited materials and this amplifies the ambiguities that already characterizes the fit procedure of the RBS spectrum. Furthermore, due to the complexity of the analysis, NDF cannot be taken as a routine method to evaluate all the data that can be gathered during a microprobe analysis of the polymers. Transversal section analysis validate the softwares estimation of the deposit thickness but further considerations about the structure in depth of the superficial material are limited by the spatial resolution of the microprobe system.

On the other hand, conversely to surface analysis, direct measurements of the elemental distribution in the specimens cross section permit the investigation of how permeable plastics are to metals and ions in aquatic ecosystems. Transversal cross sections of both HDPE and PET polymers, either being exposed 7 or 30 days, show, in some regions, a chlorine concentration in the plastic matrix that have not been detected in the analysis of the pristine sample, suggesting that Cl^- ions from sea-water diffuse to the plastics interior. Evidences of this phenomenon, as far as we know, has never been observed since studies and data on the literature are virtually lacking. Further analysis performed with OMDAQ2007, estimate that the Cl concentration in the plastics interior may increase with the immersion time.

Finally, the deposited materials have been also characterized estimating the concentrations of its main elements. Particles of major minerals that compose the earth crust, and can be found in the sea sediments, are identified using OMDAQ2007 capability of calculating elemental concentrations through the PIXE spectra using the matrix estimation and charge correction of RBS spectra.

Considering that the described work is the first documented trial to apply PIXE and RBS analysis performed with a nuclear microprobe to examine plastic weathering in aquatic environment, several aspects of the analysis can be improved in future works. Undoubtedly, the multi-elemental character of the used techniques is one of the mainstays of these analysis. Nevertheless, some of the major elements that compose sea-water can not be detected in the experimental setup used and this limits the identification of the chemical nature of some attached particles. This suggests that a possible upgrade could be on the sensitivity of the detecting system to elements such as Na.

The diffusion of elements inside the plastic matrix interior may has a key role in the weathering process of plastics. Studies of polymers exposed to controlled media conditions should be performed to furnish a supplementary proof of this process. In order to confirm the trend of the concentration of the diffused Cl^- ions, more regions of the exposed samples should be analyzed and longer exposure times should be considered. In fact, different regions of the same plastics samples have been observed to have chlorine diffusion while others do not and the acquired statistics does not allow to conclude if it is due to the exposure time or to in-homogeneity in the polymers matrix. Additionally, the concentration of diffused elements could be estimated, if an higher statistics is acquired, considering sequential regions of the plastic samples. The depth-dependency of the diffusion process would be thus further investigated.

There are also plenty of room to improve both OMDAQ2007 and NDF depth structure assessment. A common issue will be the acquisition of spectral data with greater statistical power. This would help improving the estimation of the interaction of elements in deposits with the plastic surface and the diffusion of elements into the polymer matrix. The NDF capabilities account for roughness, voids and different layer edge configurations, which would be interesting to explore in the search of solutions that would describe more accurately the spectral data of deposits. Hopefully NDF will be a pivotal tool to explore further the interaction of biota and salts with the plastic.

From the experimental setup point of view, the main parameters that can be changed are the particles that compose the beam and their energy and the beam current. Replacing protons with heavier ions, for example ^4He, would increase the mass resolution and the yield of RBS analysis. Better discrimination of elements in RBS spectrum and higher statistics can thus be achieved. On the other hand, the range inside the specimens becomes shorter and, regarding PIXE, the ions should be accelerated at higher energy in order to have the same ionization cross-section. Therefore, the choice of substituting protons by heavier ions is meaningful if the interest is on the depth structure of a thin (few μm) superficial layer: the higher mass resolution and yield allow the elements to be identified with RBS events and the short range decrease the contribution from the plastic substrate. Increasing the energy, considering a protons beam, could have various implications. RBS would be characterized by a lower cross-section but the achieved range would be longer and the mass resolution improved. The ionization cross-section, that determine the PIXE yield, since low atomic number elements are considered, does not change much with the energy. Therefore, accelerating the particles at higher energy, could be advantageous to decrease the ambiguities in the RBS spectrum and improve the depth profile resolution obtained. Nevertheless, it has be taken into account that samples integrity may be damaged by higher energy particles. Finally, a low current beam would improve imaging capabilities to a resolution up to 1 μm that would be appropriate to analyze the transversal cross-section of the deposit and have direct measurements of its multilayer structure. However, to have a satisfactory statistics, acquisition time have to be extended.

The results of the present study demonstrate the unique capabilities of applying nuclear microscopy, in combination with the OMDAQ2007 and NDF analytical tools, to study plastic degradation and plastic chemical transfer with minimal sample manipulation. However, the search for solutions to improve the precision of the results has to be pursued. The importance of studies like the present one relies on the information inferred on the rates and modalities of polymers weathering in marine ecosystems, upon which advanced predictions and models about plastics distributions in those environments can be based. The impact of plastic wastes in the environment and the threat they represent in terms of physical and chemical damage to living organisms and to the contamination of food webs can then be better evaluated. Advances in the scientific knowledge about plastic weathering will also have a significant impact in what concerns the implications for human food safety, demonstrating how plastic pollution is of public interest. Evidence-based research may then pave the way to decision-making processes of dedicated public bodies to reduce the amount and the impact of plastics in the environment.

References

[1] PlasticEurope. Plastics - the facts 2017. Technical report, PlasticEurope, 2017.

[2] M. Cole, P. Lindeque, C. Halsband, and T. S. Galloway. Microplastics as contaminants in the marine environment: a review. *Marine pollution bulletin*, 62(12):2588–2597, 2011.

[3] J. R. Jambeck, R. Geyer, C. Wilcox, T. R. Siegler, M. Perryman, A. Andrady, R. Narayan, and K. L. Law. Plastic waste inputs from land into the ocean. *Science*, 347(6223):768–771, 2015. doi: 10.1126/science.1260352.

[4] A. L. Andrady. Microplastics in the marine environment. *Marine Pollution Bulletin*, 62(8): 1596 – 1605, 2011. doi: https://doi.org/10.1016/j.marpolbul.2011.05.030.

[5] D. Cressey. Bottles, bags, ropes and toothbrushes: the struggle to track ocean plastics. *Nature News*, 536(265), 2016. doi: https://doi.org/10.1016/j.marpolbul.2011.05.030.

[6] J. L. Conkle, C. D. B. Del Valle, and J. W. Turner. Are we underestimating microplastic contamination in aquatic environments? *Environmental management*, 61(1):1–8, 2018.

[7] GESAMP. Sources, fate and effects of microplastics in the marine environment: a global assessment. *IMO/FAO/UNESCO-IOC/UNIDO/WMO/IAEA/UN/UNEP/UNDP Joint Group of Experts on the Scientific Aspects of Marine Environmental Protection, Report Studies GESAMP No 90*, page 96, 2015.

[8] M. Eriksen, L. C. Lebreton, H. S. Carson, M. Thiel, C. J. Moore, J. C. Borerro, F. Galgani, P. G. Ryan, and J. Reisser. Plastic pollution in the world's oceans: more than 5 trillion plastic pieces weighing over 250,000 tons afloat at sea. *PloS one*, 9(12):e111913, 2014.

[9] D. W. Laist. Overview of the biological effects of lost and discarded plastic debris in the marine environment. *Marine Pollution Bulletin*, 18(6, Supplement B):319 – 326, 1987. doi: https://doi.org/10.1016/S0025-326X(87)80019-X.

[10] C. D. Rummel, A. Jahnke, E. Gorokhova, D. Kuhnel, and M. Schmitt-Jansen. Impacts of biofilm formation on the fate and potential effects of microplastic in the aquatic environment. *Environmental Science & Technology Letters*, 4(7):258–267, 2017.

[11] L. A. Holmes, A. Turner, and R. C. Thompson. Adsorption of trace metals to plastic resin pellets in the marine environment. *Environmental Pollution*, 160:42–48, 2012.

[12] B. Gewert, M. M. Plassmann, and M. MacLeod. Pathways for degradation of plastic polymers floating in the marine environment. *Environmental Science: Processes & Impacts*, 17(9):1513–1521, 2015.

[13] J.-M. Restrepo-Florez, A. Bassi, and M. R. Thompson. Microbial degradation and deterioration of polyethylene–a review. *International Biodeterioration & Biodegradation*, 88: 83–90, 2014.

[14] M. Vedolin, C. Teophilo, A. Turra, and R. Figueira. Spatial variability in the concentrations of metals in beached microplastics. *Marine pollution bulletin*, 129(2):487–493, 2018.

[15] M. Kedzierski, M. D'Almeida, A. Magueresse, A. Le Grand, H. Duval, G. César, O. Sire, S. Bruzaud, and V. Le Tilly. Threat of plastic ageing in marine environment. adsorption/desorption of micropollutants. *Marine pollution bulletin*, 127:684–694, 2018.

[16] D. Brennecke, B. Duarte, F. Paiva, I. Cacador, and J. Canning-Clode. Microplastics as vector for heavy metal contamination from the marine environment. *Estuarine, Coastal and Shelf Science*, 178:189–195, 2016.

[17] A. A. Shah, F. Hasan, A. Hameed, and S. Ahmed. Biological degradation of plastics: a comprehensive review. *Biotechnology advances*, 26(3):246–265, 2008.

[18] J.-D. Gu. Microbiological deterioration and degradation of synthetic polymeric materials: recent research advances. *International biodeterioration & biodegradation*, 52(2):69–91, 2003.

[19] W. Li, H. Tse, and L. Fok. Plastic waste in the marine environment: A review of sources, occurrence and effects. *Science of the Total Environment*, 566:333–349, 2016.

[20] O. Setälä, M. Lehtiniemi, R. Coppock, and M. Cole. Microplastics in marine food webs. In *Microplastic Contamination in Aquatic Environments*, pages 339–363. Elsevier, 2018.

[21] R. Thompson, C. Moore, A. Andrady, M. Gregory, H. Takada, and S. Weisberg. New directions in plastic debris. *Science*, 310(5751):1117–1117, 2005. doi: 10.1126/science.310.5751.1117b.

[22] S. L. Wright, R. C. Thompson, and T. S. Galloway. The physical impacts of microplastics on marine organisms: a review. *Environmental pollution*, 178:483–92, 2013.

[23] D. A. Cooper and P. L. Corcoran. Effects of mechanical and chemical processes on the degradation of plastic beach debris on the island of kauai, hawaii. *Marine Pollution Bulletin*, 60(5):650–654, 2010.

[24] M. Zbyszewski, P. L. Corcoran, and A. Hockin. Comparison of the distribution and degradation of plastic debris along shorelines of the great lakes, north america. *Journal of Great Lakes Research*, 40(2):288–299, 2014.

[25] E. Ikada. Electron microscope observation of biodegradation of polymers. *Journal of environmental polymer degradation*, 7(4):197–201, 1999.

[26] A. Copinet, C. Bertrand, S. Govindin, V. Coma, and Y. Couturier. Effects of ultraviolet light (315 nm), temperature and relative humidity on the degradation of polylactic acid plastic films. *Chemosphere*, 55(5):763–773, 2004.

[27] X. U Zhao, Z. Li, Y. Chen, L. Shi, and Y. Zhu. Solid-phase photocatalytic degradation of polyethylene plastic under uv and solar light irradiation. *Journal of Molecular Catalysis A: Chemical*, 268(1-2):101–106, 2007.

[28] J. Kosanetzky, B. Knoerr, G. Harding, and U. Neitzel. X-ray diffraction measurements of some plastic materials and body tissues. *Medical physics*, 14(4):526–532, 1987.

[29] B. Schmidt and K. Wetzig. *Ion beams in materials processing and analysis*. Springer Science & Business Media, 2012.

[30] C. Jeynes, M. Bailey, N. Bright, M. Christopher, G. Grime, B. Jones, V. Palitsin, and R. Webb. "total iba"–where are we? *Nuclear Instruments and Methods in Physics Research Section B: Beam Interactions with Materials and Atoms*, 271:107–118, 2012.

[31] K. G. Malmqvist. Accelerator-based ion beam analysis—an overview and future prospects. *Radiation Physics and Chemistry*, 71(3-4):817–827, 2004.

[32] I. Hotovy, J. Huran, P. Siciliano, S. Capone, L. Spiess, and V. Rehacek. The influences of preparation parameters on nio thin film properties for gas-sensing application. *Sensors and Actuators B: Chemical*, 78(1-3):126–132, 2001.

[33] M. Wittmer. High-temperature contact structures for silicon semiconductor devices. *Applied Physics Letters*, 37(6):540–542, 1980.

[34] C. Ryan. Ion beam microanalysis in geoscience research. *Nuclear Instruments and Methods in Physics Research Section B: Beam Interactions with Materials and Atoms*, 219:534–549, 2004.

[35] D. Angelici, A. Borghi, F. Chiarelli, R. Cossio, G. Gariani, A. L. Giudice, A. Re, G. Pratesi, and G. Vaggelli. μ-xrf analysis of trace elements in lapis lazuli-forming minerals for a provenance study. *Microscopy and Microanalysis*, 21(2):526–533, 2015.

[36] P. A. Mandò. Advantages and limitations of external beams in applications to arts & archeology, geology and environmental problems. *Nuclear Instruments and Methods in Physics Research Section B: Beam Interactions with Materials and Atoms*, 85(1-4):815–823, 1994.

[37] J.-C. Dran, J. Salomon, T. Calligaro, and P. Walter. Ion beam analysis of art works: 14 years of use in the louvre. *Nuclear Instruments and Methods in Physics Research Section B: Beam Interactions with Materials and Atoms*, 219:7–15, 2004.

[38] V. Corregidor, A. Oliveira, P. Rodrigues, and L. Alves. Paintings on copper by the flemish artist frans francken ii: Pixe characterization by external microbeam. *Nuclear Instruments and Methods in Physics Research Section B: Beam Interactions with Materials and Atoms*, 348:291–295, 2015.

[39] W. Maenhaut. Applications of ion beam analysis in biology and medicine, a review. *Nuclear Instruments and Methods in Physics Research Section B: Beam Interactions with Materials and Atoms*, 35(3-4):388–403, 1988.

[40] K. G. Malmqvist. Ion beam analysis for the environment. *Nuclear Instruments and Methods in Physics Research Section B: Beam Interactions with Materials and Atoms*, 85(1-4):84–94, 1994.

[41] I. Orlic. The nuclear microscope: A review of applications in the environmental sciences. *Nuclear Instruments and Methods in Physics Research Section B: Beam Interactions with Materials and Atoms*, 104(1-4):602–611, 1995.

[42] L. Alves, M. Breese, E. Alves, A. Paùl, M. Da Silva, M. Da Silva, and J. Soares. Micron-scale analysis of sic/sicf composites using the new lisbon nuclear microprobe. *Nuclear Instruments and Methods in Physics Research Section B: Beam Interactions with Materials and Atoms*, 161:334–338, 2000.

[43] T. B. Johansson, R. Akselsson, and S. A. Johansson. X-ray analysis: elemental trace analysis at the 10-12 g level. *Nuclear Instruments and Methods*, 84(1):141–143, 1970.

[44] R. Woldseth. *X-ray energy spectrometry.* Kevex Corporation, 1973.

[45] G. H. Zschornack. *Handbook of X-ray Data.* Springer Science & Business Media, 2007.

[46] H. G. J. Moseley. Xciii. the high-frequency spectra of the elements. *The London, Edinburgh, and Dublin Philosophical Magazine and Journal of Science*, 26(156):1024–1034, 1913.

[47] E. Merzbacher and H. Lewis. X-ray production by heavy charged particles. In *Corpuscles and Radiation in Matter II/Korpuskeln und Strahlung in Materie II*, pages 166–192. Springer, 1958.

[48] J. Garcia. Inner-shell ionizations by proton impact. *Physical Review A*, 1(2):280, 1970.

[49] B.-H. Choi. Cross section for m-shell ionization in heavy atoms by collision of simple heavy charged particles. *Physical Review A*, 7(6):2056, 1973.

[50] W. Brandt and G. Lapicki. Energy-loss effect in inner-shell coulomb ionization by heavy charged particles. *physical review A*, 23(4):1717, 1981.

[51] F. Watt and G. W. Grime. Principles and applications of high-energy ion microbeams. 1987.

[52] Y. Wang and M. A. Nastasi. *Handbook of modern ion beam materials analysis.* Materials Research Society Warrendale, Pennsylvania, 2009.

[53] M. Nastasi, J. W. Mayer, and Y. Wang. *Ion beam analysis: fundamentals and applications.* CRC Press, 2014.

[54] Z. caron Scaronmit, M. Budnar, V. Cindro, M. Ravnikar, and V. RamScaronak. Secondary fluorescence correction in thick target pixe analysis. *Nuclear Instruments and Methods in Physics Research Section A: Accelerators, Spectrometers, Detectors and Associated Equipment*, 228(2-3):482–489, 1985.

[55] S. Rubin, T. Passell, and L. Bailey. Chemical analysis of surfaces by nuclear methods. *Analytical Chemistry*, 29(5):736–743, 1957.

[56] J. L'ecuyer, J. Davies, and N. Matsunami. How accurate are absolute rutherford backscattering yields. *Nuclear Instruments and Methods*, 160(2):337–346, 1979.

[57] H. H. Andersen, F. Besenbacher, P. Loftager, and W. Moller. Large-angle scattering of light ions in the weakly screened rutherford region. *Physical review A*, 21(6):1891, 1980.

[58] M. Bozoian, K. M. Hubbard, and M. Nastasi. Deviations from rutherford-scattering cross sections. *Nuclear Instruments and Methods in Physics Research Section B: Beam Interactions with Materials and Atoms*, 51(4):311–319, 1990.

[59] J. R. Tesmer and M. Nastasi. Handbook of modern ion beam materials analysis. *Materials Research Society, 9800 McKnight Rd, Suite 327, Pittsburgh, PA 15237, USA, 1995. 700*, 1995.

[60] J. F. Ziegler. *SRIM - The Stopping and Range of Ions in Matter*. URL `http://www.srim.org/`. Accessed April 2018.

[61] M. B. Breese, D. N. Jamieson, and P. J. King. Materials analysis using a nuclear microprobe. *John! Wiley & Sons Ltd, Journals, Baffins Lane, Chichester, Sussex PO 19 1 UD, UK, 1996. 428*, 1996.

[62] L. Doolittle. Rump: Rutherford backscattering spectroscopy analysis package. *Nucl. Instrum. Methods Phys. Res., Sect. B*, 9:344, 1985.

[63] F. Corni and M. Michelini. A didactic proposal about rutherford backscattering spectrometry with theoretic, experimental, simulation and application activities. *European Journal of Physics*, 39(1):015501, 2017.

[64] G. Grime. The "q factor" method: quantitative micropixe analysis using rbs normalisation. *Nuclear Instruments and Methods in Physics Research Section B: Beam Interactions with Materials and Atoms*, 109:170–174, 1996.

[65] D. K. Brice. Theoretical analysis of the energy spectra of back-scattered ions. *Thin Solid Films*, 19(1):121–135, 1973.

[66] *OMDAQ2007*. Oxford Microbeam Ltd. URL `http://www.microbeams.co.uk/download.html`. Accessed July 2018.

[67] *Aerodag G*. Acheson Colloids Company. URL `http://www.achesonindustries.com`.

[68] E. Rauhala. Computer analysis of ion elastic backscattering: An iterative fitting method. *Journal of applied physics*, 56(11):3324–3327, 1984.

[69] E. Kòtai. Computer methods for analysis and simulation of rbs and erda spectra. *Nuclear Instruments and Methods in Physics Research Section B: Beam Interactions with Materials and Atoms*, 85(1-4):588–596, 1994.

[70] E. Szilàgyi, F. Pàszti, and G. Amsel. Theoretical approximations for depth resolution calculations in iba methods. *Nuclear Instruments and Methods in Physics Research Section B: Beam Interactions with Materials and Atoms*, 100(1):103–121, 1995.

[71] N. Barradas, C. Jeynes, and R. Webb. Simulated annealing analysis of rutherford backscattering data. *Applied Physics Letters*, 71(2):291–293, 1997.

[72] M. Mayer. Technical report ipp9/113. Technical report, Max-Planck-Institut fur Plasmaphysik, Garching, German, 1997.

[73] C. Ryan, D. Cousens, S. Sie, and W. Griffin. Quantitative analysis of pixe spectra in geoscience applications. *Nuclear Instruments and Methods in Physics Research Section B: Beam Interactions with Materials and Atoms*, 49(1-4):271–276, 1990.

[74] J. Maxwell, J. Campbell, and W. Teesdale. The guelph pixe software package. *Nuclear Instruments and Methods in Physics Research Section B: Beam Interactions with Materials and Atoms*, 43(2):218–230, 1989.

[75] E. Clayton. Pixan: The lucas heights pixe analysis computer package. Technical report, Australian Atomic Energy Commission Research Establishment, 1986.

[76] G. Szabò and I. Borbèly-Kiss. Pixyklm computer package for pixe analyses. *Nuclear Instruments and Methods in Physics Research Section B: Beam Interactions with Materials and Atoms*, 75(1-4):123–126, 1993.

[77] K. Sera and S. Futatsugawa. Personal computer aided data handling and analysis for pixe. *Nuclear Instruments and Methods in Physics Research Section B: Beam Interactions with Materials and Atoms*, 109:99–104, 1996.

[78] N. Barradas and C. Jeynes. Advanced physics and algorithms in the iba datafurnace. *Nuclear Instruments and Methods in Physics Research Section B: Beam Interactions with Materials and Atoms*, 266(8):1875–1879, 2008.

[79] L. C. Hofmann and K. Bischof. Ocean acidification effects on calcifying macroalgae. *Aquatic biology*, 22:261–279, 2014.

[80] K. H. Wedepohl. The composition of the continental crust. *Geochimica et cosmochimica Acta*, 59(7):1217–1232, 1995.

[81] M. Babel and B. Schreiber. 9.17-geochemistry of evaporites and evolution of seawater. *Treatise on geochemistry*, pages 483–560, 2014.

[82] J. C. Wynn. Titanium geophysics: The application of induced polarization to sea-floor mineral exploration. *Geophysics*, 53(3):386–401, 1988.

[83] J. Santos-Echeandìa, C. Vale, M. Caetano, P. Pereira, and R. Prego. Effect of tidal flooding on metal distribution in pore waters of marsh sediments and its transport to water column (tagus estuary, portugal). *Marine Environmental Research*, 70(5):358–367, 2010.

[84] Y. Zheng, E. K. Yanful, and A. S. Bassi. A review of plastic waste biodegradation. *Critical Reviews in Biotechnology*, 25(4):243–250, 2005.

Appendix A

Linescans analysis procedure

Linescans along the transversal section of the samples provide the elemental distributions in function of the sample depth. Aside from analysis in which the adsorption of Cl is observed, these distributions are characterized by a gaussian-like peak in correspondence of the deposit on the plastics surface. The analysis procedure of linescans data includes two operations: define the plastic edge and fit the surface deposit using a gaussian distribution. This results in a characterization of the deposits thicknesses and in the investigation of the PIXE and RBS imaging capabilities to deduce alteration in the interface between plastics and deposit.
In order to define the plastic edge, that corresponds to the 0 μm depth in the linescans presented in the thesis, the carbon distribution is considered for all the polymers since C is their major component. Firstly, a reference is defined analyzing the linescans of the pristine plastic samples. The parameter that has been chosen to compare the linescans edge of different samples of the same polymer is the linear slope of the distribution at the plastic edge. In particular, for the blank samples, an arbitrary and reasonable depth range related to the plastic edge is chosen. Before operating the linear fit, the counts of the selected region of the linescans are normalized to the counts of the last pixel of the range. This allows the comparison between edge slopes of different elements and different linescans. The last pixel of the defined edge is set also to be the zero-depth point of the pristine sample. The linear fit is then exploited to estimate the standard slope relative to each particular polymer. For HDPE and PET specimens, in principle, respectively Ti and O could be used for this purpuse but their yield, compared to C, is smaller and, in addition to this, they can be also a component of the deposit on the surface. Nevertheless, if possible, these plastic components could be used to confirm the rightness of the plastic edge choice. Estimated slope values of pristine samples of each polymers are reported on Table A.1.

HDPE slope		PET slope	
C	Ti	C	O
0.051 ± 0.002	0.048 ± 0.005	0.042 ± 0.002	0.041 ± 0.006
0.050 ± 0.004	0.068 ± 0.007		

Table A.1: Slopes of the edge [*norm. counts* / μm] of C and Ti for HDPE and C and O for PET of normalized linescans along the sample transversal section maps.

When the transversal section of exposed samples is analyzed, the zero-depth point is assumed to be the position in which begins the plastic substrate. It is set, for every linescan, referring to the edge slope values of the correspondent polymer pristine sample (Table A.1). Similarly to blank samples, a depth range is chosen in the plastic edge region. The part of the distribution included is fitted with a linear function after having normalized the counts of each pixel to the ones of the last point of the selected range. If the estimated slope is close to the value of the blank sample, the range boundary related to the plastic edge is defined as the zero-depth point of the specific linescan. On the other hand, if the slope value does not agree with the standard, the range is changed till the estimated value is close to the correspondent pristine sample. Fig. A.1 shows a typical linescan and the zero-depth definition procedure.

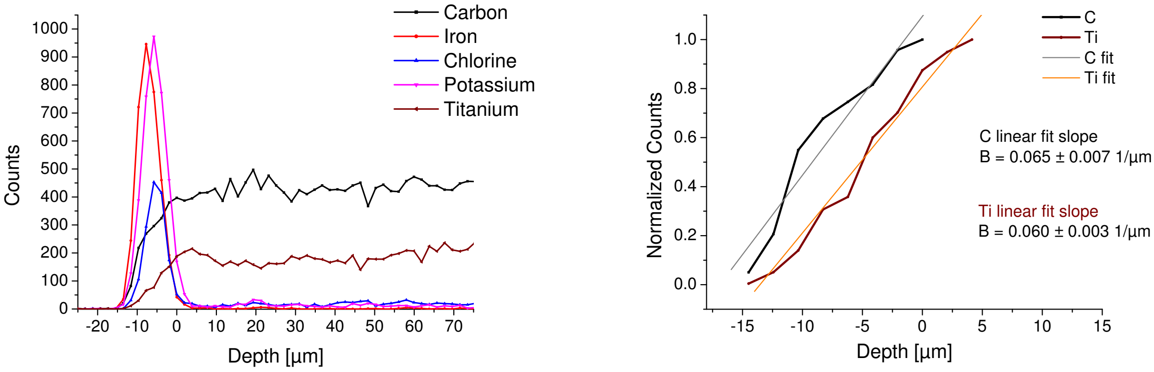

(a) C, Fe, Cl, K and Ti transversal distributions

(b) C and Ti distributions at the plastic edge

Figure A.1: A typical linescan (a) provides the transversal distributions of the single elements present in the sample. Fem Cl and K compose the superficial deposit while C, Ti the plastic matrix (HDPE in this example. In order to define the interface between the deposited material and the plastic sample, the edge range of the C and Ti distributions are linearly fitted (b). Resulted slopes are reported in the correspondent graph.

The presented edge choice has the best agreement to the standard slope values even if, as it can be noticed, they are not completely compatible with the standards. In fact, this method to define the plastic edge may not be always accurate. The assumption that the plastic edge is perfectly straight does not reflect the real shape of the samples, in which roughness and imperfection are common. Moreover, the deposit is covered by a C layer of the spray, so the C counts in the linescans may not have a linear growth but follow the deposit counts distribution. In linescans where the deviation from a linear growth does not allow a proper linear fit, the plastic starting point is defined to be where the C counts start to be constant, without checking the C edge slope.

The definition of the zero is the first operation during the analysis of cross-section data. Afterwards, the deposit widths are estimated analyzing the peak in the elements superficial distributions. The thickness of the deposit is assumed to be the FWHMs of the gaussian fits of these peaks. The uncertainties deriving by the PIXE resolution and the complexity of the samples analyzed do not allow to make more complicated assumptions. Considering the same linescan presented in Fig. A.1 a, the analysis of the peaks of the relative main elements are reported in Fig. A.2.

In this linescan, the thickness of the deposit is about 5/6 μm. The distributions included in the

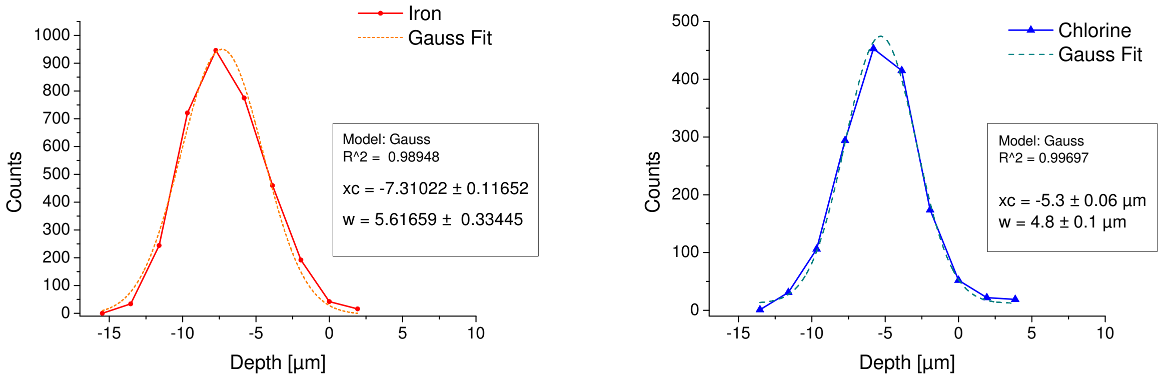

(a) Iron (b) Chlorine

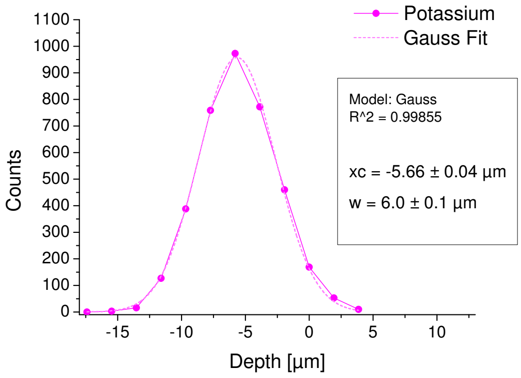

(c) Potassium

Figure A.2: Gaussian fits of the main element of the linescan reported in Fig. A.1. In particular, Fe (a), Cl (b) and K (c) superficial peaks are considered. The estimated FWHMs are reported in the graphs, together with centroid of the gaussian function relative to the zero-depth position previously defined.

linescan show compatible widths. The elements are on top of the plastic sample as it can be noticed comparing the zero-depth position with the centroids of the gaussian fits. The different positions of the centroids may state that the deposit have a multilayer composition, with different element at different depth. In this specific example, a first layer characterized by an high Fe concentration is followed by a bottom layer dominated by the presence of Cl and K (maybe KCl saline particle).

Further considerations about the interaction in the superficial interface between deposited material and plastic substrate are not possible. The definition of the samples starting point is user-dependent and not accurate. A more reliable definition of the zero-depth position could be the middle point of the range correspondent to the plastic edge. However, for samples with non-linear C distributions in this range, this definition is not applicable and the alternative method to set the plastic starting-point just before the C plateau does not suit the middle-range definition.